

# Single $\pi^0$ electroproduction off the proton in the resonance region

Nikolay Markov, Ph.D.

University of Connecticut, 2012

We study a  $\pi^0$  electroproduction off the proton in the invariant mass range for the  $p\pi^0$  system of  $W = 1.1 - 1.8 \text{ GeV}$  in the broad range of the photon virtualities  $Q^2 = 0.4 - 1.0 \text{ GeV}^2$ . The experiment was conducted in the Hall B at the Jefferson Lab with the CEBAF Large Acceptance Spectrometer (CLAS) detector which is uniquely suited for the spectroscopic measurements. The channel is identified by subsequent determination of the electron using information from the forward angle electromagnetic calorimeter and the drift chambers, and proton from the time of flight and drift chambers signals. Kinematical relations between the charged particles separate the single pion events. The detector efficiency and the geometrical acceptance are studied with the GEANT simulation of the CLAS. The exclusive channel radiative corrections are developed and applied. The full differential cross section of the  $\pi^0$  electroproduction is measured with high statistical accuracy and small systematical error. The quality of the overall

data analysis is checked against the firmly established benchmark reactions. The structure functions and Legendre multipoles are extracted and show the sensitivity of our measurements to the different resonance electroproduction amplitudes. The advanced phenomenological approach will be used to extract the  $Q^2$  evolution of the electromagnetic transition form factors of the different resonance states in the combined analysis of the major exclusive channels. This information will notably improve our understanding of the structure of the nucleon.

**Single  $\pi^0$  electroproduction off the proton in the  
resonance region**

Nikolay Markov

M.S., Moscow State University, 2002

A Dissertation

Submitted in Partial Fulfillment of the

Requirements for the Degree of

Doctor of Philosophy

at the

University of Connecticut

2012

Copyright by

Nikolay Markov

2012

# APPROVAL PAGE

Doctor of Philosophy Dissertation

## Single $\pi^0$ electroproduction off the proton in the resonance region

Presented by

Nikolay Markov,

Major Advisor

---

Kyungseon Joo

Associate Advisor

---

Maurizio Ungaro

Associate Advisor

---

Richard Jones

University of Connecticut

2012

To my friends, Gleb and Zhenia

## ACKNOWLEDGEMENTS

First and foremost, I would like to thank my adviser, Kyungseon Joo, who made my transition from Moscow State to UConn really an easy one, put me in JLab, an excellent place to do a research, supported me during all these years, helped with every aspect of work and life and was overall extremely patient, knowledgeable and helpful. Maurizio Ungaro, former postdoc at the UConn and a new addition to JLab staff, a promotion he deserved long time ago in my eyes. He was a person right here, in JLab, to ask any question from detector calibration to C++ details, from analysis details to best places to show to my parents when they came to visit me. I am really happy that the person who introduced me to nuclear physics, Viktor Mokeev, is still nearby and is as approachable, helpful and lively as he has always been. Help of Cole Smith on the last stages of my analysis was invaluable. His expertise, willingness to help and ability to look at my work as an outsider helped to reveal and fix quite a few flaws and errors as well as introduced significant improvements. JLab staff and users, all helpful and competent, are too numerous to name, but especially want to mention Avto Tkabladze, Valery Kubarovsky, Stepan Stepanyan, Hovanes Egiyan, Eugene Pasyuk, Nerses Gevorgyan, Francois-Xavier Girod, Ivan Bedlinskiy. My friend and colleague of old time, Gleb Fedotov, both helped me to get started with my work and accommodate to living in Newport

News. Good friend of mine, Eugenia Ivanova, who spent quite some time reading my thesis. My friends in Newport News who helped me to have a life outside of work, Sergey Abrahamyan, Eugene Isupov, Mikhail Yurov, Taisiya Mineeva, Balsa Terzic. And of course my most important ones, wife Natalia and son Andrey, who happened to appear during my studentship. Without them nothing would be possible, and the same should be said about my parents, who, despite many thousands miles between us, were very close to me all these years.

# TABLE OF CONTENTS

<b>1. Introduction</b> . . . . .	1
<b>2. Theory</b> . . . . .	6
2.1 Strong interactions . . . . .	6
2.1.1 QCD . . . . .	6
2.1.2 Formation of hadrons . . . . .	9
2.1.3 Lattice QCD . . . . .	12
2.2 Hadrons in the models of the strong interaction . . . . .	14
2.3 Nucleon resonances . . . . .	18
2.3.1 Introduction . . . . .	18
2.3.2 Formalism . . . . .	19
2.3.3 Theoretical approaches for the analysis of the pion electroproduction	27
2.3.4 Properties of the selected resonances . . . . .	31
2.3.5 Current state of the data and analysis . . . . .	37
<b>3. Experimental setup</b> . . . . .	42
3.1 CEBAF accelerator . . . . .	42
3.2 CLAS detector . . . . .	44
3.2.1 Torus magnet . . . . .	46
3.2.2 Drift chambers . . . . .	47
3.2.3 Cerenkov counter . . . . .	50

3.2.4	Time of flight system . . . . .	52
3.2.5	Electromagnetic calorimeter . . . . .	52
3.3	Run conditions . . . . .	54
<b>4.</b>	<b>Data analysis . . . . .</b>	<b>57</b>
4.1	Data handling . . . . .	57
4.2	Event selection . . . . .	58
4.3	Particle ID . . . . .	59
4.3.1	Electron ID . . . . .	59
4.3.2	Proton ID . . . . .	63
4.4	Vertex and momentum corrections . . . . .	68
4.4.1	Vertex correction . . . . .	68
4.4.2	Cut on the vertex position . . . . .	69
4.4.3	Proton energy loss . . . . .	70
4.4.4	Electron momentum correction . . . . .	71
4.4.5	Proton momentum correction . . . . .	78
4.5	Fiducial cuts . . . . .	82
4.5.1	Electron fiducial cut . . . . .	82
4.5.2	Proton fiducial cuts . . . . .	84
4.6	Bethe-Heitler processes . . . . .	88
<b>5.</b>	<b>Simulation . . . . .</b>	<b>93</b>

5.1	Overview	93
5.2	Drift chambers resolution	94
5.3	Time of flight and drift chambers smearing	96
<b>6.</b>	<b>Results</b>	<b>101</b>
6.1	Binning	101
6.2	Corrections	103
6.2.1	Radiative correction	103
6.2.2	Bin centering correction	107
6.2.3	Acceptance correction	108
6.2.4	Target wall subtraction	109
6.3	Cross section	118
6.4	Structure functions	122
6.5	Absolute normalization	127
6.5.1	Data set selection	137
6.5.2	Elastic cross section	137
6.5.3	Inclusive cross section	139
6.6	Summary	143
6.7	Systematics studies	144
6.7.1	Overview	144
6.7.2	Electron ID	145
6.7.3	Proton ID	146

6.7.4	Pion ID . . . . .	147
6.7.5	Normalization uncertainty . . . . .	150
6.7.6	Summary . . . . .	150
6.7.7	Error propagation . . . . .	150
<b>7.</b>	<b>Physics analysis . . . . .</b>	<b>153</b>
7.1	Legendre polynomials and fits to the structure functions . . . . .	153
7.2	Multipole analysis . . . . .	157
7.3	Conclusion . . . . .	168
<b>8.</b>	<b>BIBLIOGRAPHY . . . . .</b>	<b>171</b>
8.1	* . . . . .	171
<b>A.</b>	<b>Legendre multipoles and structure functions . . . . .</b>	<b>180</b>

# LIST OF FIGURES

1.1	Electroexcitation of the proton to the excited $N^*$ state. The incoming electron emits a virtual photon which produces the excited nucleon, which in turn decays into a ground state nucleon and one or more mesons. The helicity amplitudes are shown in red and the multipoles of the pion-nucleon system in blue. Details will be provided later in this section. . . . .	3
2.1	The fundamental diagrams of the QCD. Two diagrams on the right shows self interaction of gluons. . . . .	8
2.2	Dressing of the bare quark (above) and the bare gluon (below) with a cloud of gluons and $q\bar{q}$ pairs. . . . .	10
2.3	Dressed quark mass function. The solid curves - DSE results, 'data' - numerical simulation of the LQCD. The current quark of the perturbative QCD evolving into constituent quark as its momentum drops. The constituent quark mass arises from a gluon cloud. . . .	12
2.4	$\pi^0$ electroproduction schematic. E is the electron scattering plane, H is the hadron production plane. . . . .	20
2.5	Diagrams corresponding to non-resonant (A), (B) and (C), and resonant (D) contributions to $\pi^0$ electroproduction. . . . .	21

2.6	<p>Multipole notation for the pion photoproduction. The photon with orbital angular momentum <math>L</math> excites the <math>N^*</math> state with isospin <math>I</math>, spin <math>J</math> and parity <math>P</math> which then decays into pion with orbital angular momentum <math>l</math> and nucleon. . . . .</p>	23
2.7	<p>Left: form factor <math>G^*(Q^2)</math> for the <math>\gamma^* \rightarrow \Delta(1232)</math> transition relative to the <math>3G_D(Q^2)</math>, <math>G_D(Q^2) = 1/(1 + \frac{Q^2}{0.71\text{GeV}^2})</math>. Right: ratios <math>R_{EM}</math>, <math>R_{SM}</math> [39]. The full boxes and uncertainties are from the Jlab analysis [63]. The results of the Mainz group analysis using the MAID2007 [57] are shown by dotted curves. MAMI [52], [53]- open triangles, MIT/Bates ([54], [55], [56]) - open crosses; JLab/Hall C ([50]) - open rhombuses, JLab/Hall C [51] - open boxes, JLab/Hall A [45, 46] - open circles. The older results from NINA [69] and MAMI [70], [71] are shown in full triangles. The solid and dashed curves are dressed and bare contributions from [72], for <math>R_{EM}</math> and <math>R_{SM}</math> only dressed contributions are shown. The dashed-dotted and thin dashed lines are obtained in the large-<math>N_c</math> limit of QCD of Refs [73, 74, 75]. . . . .</p>	33

2.8 Helicity amplitudes for the  $\gamma^*N \rightarrow N(1440)P_{11}$  transition [39]. The full circles and uncertainties bands are from the Jlab analysis [62], [63]. The results of the Mainz group analysis using the MAID2007 [57] are shown by dotted curves. The solid box at  $Q^2 = 0$  is the result extracted from the pion photoproduction data [76]. The results above correspond to the  $M = 1440 \text{ MeV}$ ,  $\Gamma_{tot} = 350 \text{ MeV}$ ,  $\beta_{\pi N} = 0.6$ . The solid triangle at  $Q^2 = 0$  is the RPP estimate [77]. The open boxes are from the combined analysis of CLAS single and double pion electroproduction data [41]. The open triangles are from CLAS  $2\pi$  electroproduction data with  $\beta_{2\pi N} = 0.4$  [64]. The solid and dashed-dotted curves are obtained in the LF relativistic quark model [78] and the covariant spectator quark model [79] assuming that the Roper resonance is a first radial excitation of the  $3q$  ground state. The thin solid curves are non-relativistic quark model predictions from [67]. The dashed curves are obtained assuming that the  $N(1440)P_{11}$  is a gluonic baryon excitation ( $q^3G$  hybrid state) [67]. 34

2.9	<p>Helicity amplitudes for the <math>\gamma^* N \rightarrow N(1550)S_{11}</math> transition [39]. For the amplitudes from the single pion channels the legend is the same as on the Fig. 2.8. The amplitudes from the <math>\eta</math> electroproduction: the stars [80], the open boxes [81], open circles [82], the crosses [83] and the rhombuses [40], [84]. The dashed and dashed-dotted curves show predictions of LF relativistic quark models [85] and [86] respectively. The solid lines show the amplitudes found within light-cone sum rules using lattice results for the light-cone distribution amplitudes of the <math>N(1535)S_{11}</math> resonance [87]. . . . .</p>	35
2.10	<p>Helicity amplitudes for the <math>D_{13}(1520)</math> state. The full boxes and circles are from the Jlab analysis [62, 63]. The results of the Mainz group analysis using the MAID2007 [57] are shown by dotted curves. MAMI [52, 53] - open triangles, [51] - open boxes. The older results from NINA [69] and MAMI [70, 71] are shown in full triangles. Curves are different model predictions. . . . .</p>	36

2.11	The helicity amplitudes for the $F_{15}(1680)$ [91]. The dots are MAID results from the data in Table 2.1. The solid and dashed curves are the results of the MAID superglobal fit and the predictions of the hyperspherical constituent quark model [92]. The dotted lines show the pion cloud contributions calculated with DMT [93]. The data points at finite $Q^2$ are the results of the single- $Q^2$ fits. At $Q^2 = 0$ the photon couplings from the PDG are shown [1]. . . . .	38
3.1	CEBAF accelerator and three experimental Halls. Injector serves as a source of electrons. . . . .	43
3.2	Cross section of CLAS detector. Different subsystems shown in color and will be explained below. . . . .	45
3.3	(A) Contours of constant magnetic field for the magnet in the midplane between coils. Thin gray lines represent projection of the magnet coils; (B) Magnetic field map for the CLAS toroid transverse to the beam in the midplane of the target. The cross section of coils is shown. . . . .	48
3.4	Picture of the layer. The field wires form a hexagonal cell surrounding the sense wire. Particle traveling through the gas (solid line) will produce current in the nearby cells. . . . .	49

3.5	Active gas volume is surrounded by elliptical and hyperbolic mirrors, directing particle radiation toward the Winston cones and photomultipliers. . . . .	51
3.6	One sector of the TOF counters. Scintillators at the forward direction (on the right) are shorter than at the higher angles. Each scintillator has two PMT to collect light. . . . .	53
3.7	Three scintillator layers (U, V, W) are rotated at $120^\circ$ with respect to each other to improve the spatial resolution in the EC. Optical readout scheme is also shown. . . . .	54
3.8	Photograph of the target cell for e1e run. Above: target cell and support structure. Below: closeup of the target cell. . . . .	56
4.1	U, V and W events distributions in calorimeter along with cut lines. . . . .	60
4.2	Ineffective region of sector three is excluded from the further analysis. . . . .	61
4.3	Energy deposited in inner calorimeter versus energy in outer calorimeter. Events on the left of the black line are negative pions. . . . .	62
4.4	Total energy, deposited in calorimeter, divided by momentum, versus momentum for negatively charged particles. The pions manifest themselves as $\frac{1}{x}$ band on the left plot at lower values of momentum. Red solid lines is resulting sampling fraction cut position. Vertical green line is minimum momentum cut. . . . .	64

4.5	TOF mass distribution versus momentum for different sectors. Note the erroneous structures especially prominent in the third sector. . . . .	65
4.6	$\Delta T$ (Eq. 4.6) versus particle momentum for one scintillator. <i>a</i> ) correct picture; <i>b</i> ) 2 ns shift (wrong beam bunch); <i>c</i> ) small shift (scintillator not calibrated to the bunch). . . . .	66
4.7	TOF mass distribution versus momentum for different sectors. The major structures in Sectors 2 and 3 are eliminated . . . . .	66
4.8	$\Delta T$ versus momentum distribution for positively charged particles along with the cut lines to select protons. . . . .	67
4.9	Reason of incorrect vertex reconstruction: when beam line and CLAS center line do not coincide, event, occurred in $R$ , will be projected on the centerline with electron $Z$ coordinate $A$ and $Z$ proton coordinate $B$ , while real position should be $R'$ . . . . .	68
4.10	$Z$ coordinate of electron vertex before (left) and after (right) correction. Different colors correspond to different sectors. . . . .	69
4.11	$Z$ coordinate of the electron vertex before the vertex cut along with the cut lines (red). The spike around $Z = 3$ cm is the foil. . . . .	70
4.12	Difference between the electron and proton $Z$ in the target. The cut $ \Delta Z  < 4$ cm is presented by red lines. . . . .	71
4.13	$W$ spectrum for elastic events. Black vertical line is true peak position at $W = 938.3$ MeV. . . . .	72

4.14	Electron momentum coverage for elastic (black), BH(red) and $\pi^0$ events (green). . . . .	73
4.15	$\theta_e$ coverage for elastic (black), BH(red) and $\pi^0$ events (green). . . . .	73
4.16	Preradiative (A) and postradiative (B) BH processes. Electron momentum after interaction can be measured in the first case. . . . .	74
4.17	BH events selection using $\phi_p - \phi_e$ cut. Events between red lines selected as a candidate BH events. . . . .	74
4.18	BH events selection using $\theta_x$ cut. Events on the left of red line selected as a candidate BH events. . . . .	74
4.19	$\frac{\Delta P_e}{P_e}$ for elastic events before correction with fit with $2^{nd}$ order polynomial (solid black line). . . . .	76
4.20	$\frac{\Delta P_e}{P_e}$ for elastic events before correction with fit with $2^{nd}$ order polynomial (solid black line). . . . .	76
4.21	Linear interpolation of a, b and c (Eq. 4.9) as a function of W. . . . .	76
4.22	$\frac{\Delta P_e}{P_e}$ for elastic events along with $2^{nd}$ order fit after correction. . . . .	77
4.23	$\frac{\Delta P_e}{P_e}$ for BH events along with $2^{nd}$ order fit after correction. . . . .	77
4.24	W distribution before (black) and after (green) correction. Vertical black line is at the proton mass (938.3 MeV). . . . .	77
4.25	$M_x^2$ distribution before (black) and after (green) correction. Vertical black line shown at zero. . . . .	77

4.26	W peak position as a function of sector before (black) and after (green) correction. Horizontal red line is at the nominal value of 939.3 MeV.	78
4.27	Width of W peak as a function of sector before (black) and green (after) correction.	78
4.28	$M_x^2$ peak position as a function of sector before (black) and after (green) correction. Horizontal red line is at zero, nominal position of the missing mass peak.	79
4.29	Width of missing mass peak as a function of sector before (black) and after (green) correction.	79
4.30	$\pi^0 M_x^2$ distribution for sector 1 along with the proposed cuts.	80
4.31	$\frac{\Delta P}{P}$ as a function of $\phi$ of the proton before correction.	81
4.32	$\frac{\Delta P}{P}$ as a function of $\phi$ of the proton after correction.	81
4.33	$\theta_e$ vs $\phi_e$ distribution of electrons in sector 1 with $1.2 \leq p \leq 1.4$ GeV before (left) and after fiducial cut. Blue line shows cut position.	83
4.34	$\phi_e$ distribution of electrons in sector 1 with $1.2 \leq P \leq 1.4$ GeV before (black) and after (green) fiducial cut. Note that shoulders found in original data absent after the cut.	84
4.35	Proton $\theta - \phi$ distribution before (left) and after (right) elastic events subtraction.	85
4.36	Proton $\theta - \phi$ distribution in momentum bins with proposed cut lines.	86

4.37	$\theta - P$ events distribution for the data. There are two prominent holes in the sector 2 and 5 and few smaller ones. Black lines illustrate the cuts. Exactly same cuts will be applied to the simulation. . . . .	87
4.38	W versus $M_x^2$ for all events. Structure around $0.02 \text{ GeV}^2$ shows pions. . . . .	88
4.39	The $\phi_{\pi^0}^*$ of the pion versus missing mass squared. Events below red cut lines are BH candidates. . . . .	90
4.40	$\Delta\theta_1$ versus $M_x^2$ (left plot) and its projection on the X axis. Events on the left of the cut line are BH contamination. . . . .	91
4.41	$\Delta\theta_2$ versus $M_x^2$ (left plot) and its projection on the X axis. Events on the left of the cut line are BH contamination. . . . .	92
4.42	The $\phi_{\pi^0}^*$ of pion versus missing mass squared for selected single pion events. . . . .	92
5.1	calDOCA and fitDOCA measured from the charge collection time and from the track fitted using all the DC cells. . . . .	95
5.2	The fit to the $ fitDOCA - calDOCA $ as a function of the fitDOCA. Black points are data, black solid line - $8^{th}$ order polynomial fit. . . . .	95
5.3	The fit to the $ fitDOCA - calDOCA $ as a function of the fitDOCA. Green circles are data, red - simulation, black solid line - $8^{th}$ order polynomial fit to the data points. . . . .	96
5.4	TOF proton mass peak width for data. . . . .	97
5.5	TOF proton mass peak width for simulation without additional smearing. . . . .	97

5.6	Width of TOF proton mass peak versus smearing factor $f$ . Horizontal red line represents width of the peak in data. Intersection at $f = 1.1$ corresponds to the correcting factor to be used in simulation. . . . .	97
5.7	Width of $\pi^0$ missing mass peak versus smearing factor. Horizontal red line represents width of the peak in data. Intersection at $a = b = c = 2.5$ corresponds to the correcting factor to be used in simulation. . . . .	98
5.8	$\pi^0$ missing mass peak width for data. Width is $0.0053 \text{ GeV}^2$ . . . . .	99
5.9	$\pi^0$ missing mass peak width for simulation with smearing factors $a = b = c = 2.5$ . Width is $0.0053 \text{ GeV}^2$ . . . . .	99
5.10	Left to right: $mm^2$ versus $\phi_{\pi^0}^*$ for the data after $\pi^0$ id, $mm^2$ versus $\phi_{\pi^0}^*$ for the simulation after $\pi^0$ id, missing mass distribution for data and simulation overlapped for the $W = 1.2875 \text{ GeV}$ , $Q^2 = 0.75 \text{ GeV}^2$ and different $\cos\theta_{\pi^0}^*$ bins. The normalization factor is chosen as a ratio of the total number of the $\pi^0$ events in data and simulation and is the same for all bins. . . . .	100
6.1	$W$ and $Q^2$ binning for the $\pi^0$ electroproduction events. Full resonance region is extensively covered. . . . .	102
6.2	$\cos\theta_{\pi^0}^*$ and $\phi_{\pi^0}^*$ binning for the $\pi^0$ electroproduction events. Full angular coverage with fine $\phi_{\pi^0}^*$ binning is crucial for future analysis. . . . .	103

6.3	Left to right: postradiative bremsstrahlung radiation, postradiative bremsstrahlung radiation, vertex modification, vacuum polarization.	104
6.4	Radiative corrections as a function of $\cos\theta_{\pi^0}^*$ and $\phi_{\pi^0}^*$ for $W = 1.2625 \text{ GeV}$ and $Q^2 = 0.75 \text{ GeV}^2$ .	107
6.5	Difference between center point of the bin (red circle) and bin average (green circle).	108
6.6	Example of the bin centering correction as a function of $\cos\theta_{\pi^0}^*$ and $\phi_{\pi^0}^*$ for $W = 1.2625 \text{ GeV}$ and $Q^2 = 0.75 \text{ GeV}^2$ .	109
6.7	Acceptance for one of the $W - Q^2$ bins. Number of $\phi_{\pi^0}^*$ bins is equal to 96, different panels correspond to different $\cos\theta_{\pi^0}^*$ values.	110
6.8	For selected $\pi^0$ , we isolate the events from the forward foil using the electron vertex coordinate $1.5 < Z_e < 3.2 \text{ cm}$ (left plot).	111
6.9	All $\pi^0$ events (black), events originated in the foil (green), result of the subtraction (blue) for lowest $W$ bin. Different panels correspond to different values of the $\cos(\theta_{\pi^0}^*)$ . Note the remaining contamination at the lowest $\cos(\theta_{\pi^0}^*)$ .	113
6.10	Electron vertex coordinate versus missing mass squared for the $W <$ $1.15 \text{ GeV}$ and $\cos\theta_{\pi^0}^* < -0.6$ with proposed cut to select events at lower $M_x^2$ (left plot); the same plot with the $M_x^2$ cutoff at $0.005$ $\text{GeV}^2$ (middle plot); the projection of the middle plot on the $Z$ axis. The right peak is the forward foil (right plot).	114

6.11	Number of events from the empty target runs divided in the bins over W and $\cos\theta_{\pi^0}^*$ . . . . .	115
6.12	Different methods of the target windows subtraction for different values of the $\cos\theta_{\pi^0}^*$ . Red squares - data, no subtraction, black triangles - data, subtraction based on the empty target runs, blue stars - data, subtraction based on the forward foil events. Red solid line (MAID07 predictions) and blue solid line (SAID08 predictions) are shown for the reference. The correction is significant at lower $\cos\theta_{\pi^0}^*$ values and is negligible as we go higher. . . . .	116
6.13	Different methods of the target windows subtraction for different values of the $\cos\theta_{\pi^0}^*$ . Red squares - data, no subtraction, black triangles - data, subtraction based on the empty target runs, blue stars - data, subtraction based on the forward foil events. Red solid line (MAID07 predictions) and blue solid line (SAID08 predictions) are shown for the reference. The correction at higher W region is neg- ligible. . . . .	117
6.14	W dependence of the cross section at fixed values of $Q^2$ and $\phi_{\pi^0}^*$ . Dif- ferent panels correspond to different values of $\cos\theta_{\pi^0}^*$ . . . . .	121

6.15	Sample cross section for one $W - Q^2 - \cos\theta_{\pi^0}^*$ bin near the $\Delta$ , overlapped with MAID07 (red line) and SAID08 (blue line) predictions. Black solid line is the fit to extract structure functions (more details in the Section 6.4). . . . .	123
6.16	Sample cross section for one $W - Q^2 - \cos\theta_{\pi^0}^*$ bin at the $W = 1.4375$ GeV overlapped with MAID07 (red line) and SAID08 (blue line) predictions. Black solid line is the fit to extract structure functions (more details in the Section 6.4). . . . .	124
6.17	Sample cross section for one $W - Q^2 - \cos\theta_{\pi^0}^*$ bin at the $W = 1.5875$ GeV overlapped with MAID07 (red line) and SAID08 (blue line). Note higher $Q^2$ value. Black solid line is the fit to extract structure functions (more details in the Section 6.4). . . . .	125
6.18	$\chi^2/\nu$ distributions for the different $Q^2$ bins. The center of each distribution is around one, which confirms the quality of the fit. . . . .	127
6.19	$\sigma_T + \epsilon\sigma_L$ from Eq. 6.18 in $W$ range around $\Delta$ in different $Q^2$ bins overlapped with predictions of the models. . . . .	128
6.20	$\sigma_{LT}$ from Eq. 6.18 in $W$ range around $\Delta$ in different $Q^2$ bins overlapped with predictions of the models. . . . .	129
6.21	$\sigma_{TT}$ from Eq. 6.18 in $W$ range around $\Delta$ in different $Q^2$ bins overlapped with predictions of the models. . . . .	130

6.22 $\sigma_T + \epsilon\sigma_L$ from Eq. 6.18 at $W = 1.4625$ GeV in different $Q^2$ bins overlapped with predictions of the models. . . . .	131
6.23 $\sigma_{LT}$ from Eq. 6.18 at $W = 1.4625$ GeV in different $Q^2$ bins overlapped with predictions of the models. . . . .	132
6.24 $\sigma_{TT}$ from Eq. 6.18 at $W = 1.4625$ GeV in different $Q^2$ bins overlapped with predictions of the models. . . . .	133
6.25 $\sigma_T + \epsilon\sigma_L$ from Eq. 6.18 at $W = 1.6125$ GeV in different $Q^2$ bins overlapped with predictions of the models. . . . .	134
6.26 $\sigma_{LT}$ from Eq. 6.18 at $W = 1.6125$ GeV in different $Q^2$ bins overlapped with predictions of the models. . . . .	135
6.27 $\sigma_{TT}$ from Eq. 6.18 at $W = 1.6125$ GeV in different $Q^2$ bins overlapped with predictions of the models. . . . .	136
6.28 Number of events per Faraday cup charge for the different reactions. Excluded runs are highlighted in red. . . . .	138
6.29 Spectrum of generated events with radiative tail. . . . .	139
6.30 Ratio of the elastic cross section in case of the electron detection to the Bosted parametrization as a function of the electron $\theta$ in different sectors. Red line is $1 \pm 5\%$ . . . . .	140
6.31 Ratio of the elastic cross section in case of the simultaneous electron and proton detection to the Bosted parametrization as a function of the electron $\theta$ . Red line is $1 \pm 5\%$ , green line - $1 \pm 10\%$ . . . . .	141

6.32	Inclusive cross section compared to Brasse (red) and Keppel (black) parametrization. . . . .	142
6.33	The radiative corrections corresponding to the different values of the $V_{cut}$ (black: 0.0475; green: 0.0367; yellow: 0.0258; red: 0.058; blue: 0.069) . . . . .	149
6.34	Variations of the $\Delta\theta_1$ cut. Red line is nominal cut position ( $5^\circ$ ), black lines show variations. . . . .	149
7.1	Fit to the structure function $\sigma_{TT}$ with the Legendre polynomials of the different orders. The case of $l = 1$ ( $s$ -wave only) does not provide good enough description of the data. . . . .	156
7.2	The $A_0$ coefficient (see Eq. 7.7) as a function of $Q^2$ in the different $W$ bins. Reported results (magenta circles) are compared to the Hall B results of [48] (red triangles and black squares, obtained with the different beam energy), [47] (green circles), [49] (blue crosses), and results of Hall A [46] (solid black square). . . . .	157
7.3	The $B_0$ coefficient (see Eq. 7.8) as a function of the $Q^2$ in different $W$ bins. Reported results (magenta circles) are compared to the Hall B results of [48] (red triangles and black squares, obtained with the different beam energy), [47] (green circles), [49] (blue crosses), and results of Hall A [46] (solid black square). . . . .	158

7.4	The $C_1$ (Eqs. 7.18 and 7.9) Legendre coefficient in the region of the $\Delta$ resonance. . . . .	159
7.5	The $C_1$ (Eq. 7.12) Legendre coefficient in the second resonance region. Solid lines are the full model calculations, dashed and dotted lines correspond to particular helicity amplitudes turned off. . . . .	161
7.6	The $A_3$ (Eq. 7.10) Legendre coefficient at the $Q^2 = 0.55 \text{ GeV}^2$ in the second resonance region as a function of $W$ . Solid lines are the full model calculations, dashed and dotted lines correspond to particular helicity amplitudes turned off. . . . .	162
7.7	The $A_3$ (Eq. 7.10) Legendre coefficient at the $W = 1.5375 \text{ GeV}$ as a function of the $Q^2$ . Solid lines are the full model calculations, dashed and dotted lines correspond to particular helicity amplitudes turned off. . . . .	163
7.8	The $C_2$ (Eq. 7.12) Legendre coefficient at the $W = 1.5875 \text{ GeV}$ as a function of the $Q^2$ . Solid lines are the full model calculations, dashed and dotted lines correspond to particular helicity amplitudes turned off. . . . .	164
7.9	The $C_2$ (Eq. 7.12) Legendre OA coefficient at the $Q^2 = 0.55 \text{ GeV}^2$ in the third resonance region as a function of $W$ . Solid lines are the full model calculations, dashed and dotted lines correspond to particular helicity amplitudes turned off. . . . .	165

7.10	The $A_2$ (Eq. 7.10) Legendre coefficient at the $Q^2 = 0.65 \text{ GeV}^2$ in the third resonance region as a function of $W$ . The solid lines indicate the full model calculations, and the dashed and dotted lines correspond to model calculations with specific helicity amplitudes excluded. . . . .	166
7.11	The $B_4$ (Eq. 7.11) Legendre coefficient at the $Q^2 = 0.65 \text{ GeV}^2$ in the third resonance region as a function of $W$ . Solid lines are the full model calculations, dashed and dotted lines correspond to particular helicity amplitudes turned off. . . . .	167

# LIST OF TABLES

1.1	Resonances masses and widths for selected well-established states (Ref [1]).  We use the spectroscopic notation $L_{2I2J}$ , where $L$ is the orbital momentum, $I$ is the isospin, and $J$ is the total spin of the state. . . .	4
2.1	Existing data on the $\pi^0$ electroproduction cross sections from different facilities. . . . .	37
4.1	Electron ID cuts and detector subsystem used for them. . . . .	59
4.2	Angular, momentum and invariant mass bins for electron momentum correction with BH events. . . . .	74
4.3	Angular and momentum binning for proton momentum correction. . .	80
4.4	Momentum correction results. Both pion missing mass position and width show improvement. . . . .	82
6.1	$W$ and $Q^2$ binning of the experiment. . . . .	102
6.2	Binning in $\cos\theta_{\pi^0}^*$ and $\phi_{\pi^0}^*$ . . . . .	102
6.3	Position of missing mass cut on the data and corresponding $V_{cut}$ used in excludad. . . . .	106
6.4	Missing mass cut and $V_{cut}$ values. . . . .	148
6.5	Summary of sources of systematical error. . . . .	151

# Chapter 1

## Introduction

The fundamental theory of the strong interaction, Quantum Chromodynamics (QCD), is very successful at small distances within a perturbative regime, with bare quarks and gauge gluons as the fundamental degrees of freedom. However, at the distance scale of the size of the nucleon there is a transition to completely different degrees of freedom, and strong interaction dynamics is governed by dressed quarks and gluons. Some of the fundamental phenomena of the strong interaction, like confinement, are manifestations of this non-perturbative regime.

Hadron formation is another manifestation of this regime. In addition to the ground states, like protons ( $p$ ) or neutrons ( $n$ ), we can also observe formation of their excited states ( $N^*$ ), see Table 1. Direct observations of such states are impossible due to their extremely short lifetimes, but we can study them from the products of their decays.

There are number of ways to study  $N^*$  production, including pion scattering and photoproduction, but this work concentrates on the electroproduction channel, depicted in Fig. 1.1, because of its advantages. Firstly, the electromagnetic

probe is structureless and very well known. Secondly, the virtual photon exchange allows us to study hadronic properties at different distance scales, which is crucial to understanding of the internal dynamics of the strong interaction in the confinement regime.

Using Fig. 1.1 we can relate initial  $(E_i, \mathbf{k}_i)$  and final  $(E_f, \mathbf{k}_f)$  electron four-momenta and four-momentum of the proton at rest  $p(M, 0)$  to the virtual photon four-momentum  $k(\nu, \mathbf{k})$ , where  $\nu = E_i - E_f$  is the photon energy and  $\mathbf{k} = \mathbf{k}_i - \mathbf{k}_f$  is the photon three-momentum. With the photon virtuality defined as  $Q^2 = -k^2$ , the invariant mass of the hadron system is:

$$W = \sqrt{(M^2 + 2M\nu - Q^2)}. \quad (1.1)$$

The helicity amplitudes shown in Fig. 1.1 correspond to transitions  $A_{3/2}(h_N = -\frac{1}{2}, h_\gamma = 1 \rightarrow h_{N^*} = \frac{3}{2})$ ,  $A_{1/2}(h_N = \frac{1}{2}, h_\gamma = 1 \rightarrow h_{N^*} = \frac{1}{2})$  and the longitudinal amplitude  $S_{1/2}(h_N = -\frac{1}{2}, h_\gamma = 1 \rightarrow h_{N^*} = \frac{1}{2})$ , where  $h_x$  is helicity, or projection of the spin of the particle  $x$ , on the direction of its momentum. The  $A_{3/2}$  transition changes the helicity by 2,  $A_{1/2}$  does not change it and  $S_{1/2}$  changes it by 1.

The multipoles shown on the same figure provides description in terms of electric (E), magnetic (M) and scalar (S) multipoles. These multipoles are further characterized by the relative orbital momentum  $l$  of the pion-nucleon final state. The sign of the multipole is positive or negative if the total angular momentum  $J$  is equal to  $l + \frac{1}{2}$  or  $l - \frac{1}{2}$  respectively. More details are shown in Fig 2.6.

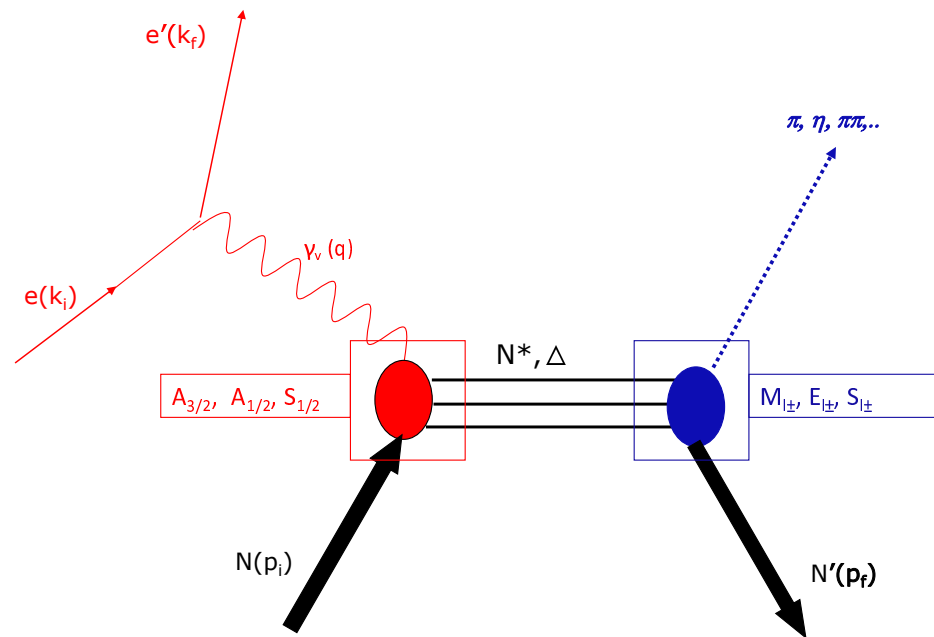


**Fig. 1.1:** Electroexcitation of the proton to the excited  $N^*$  state. The incoming electron emits a virtual photon which produces the excited nucleon, which in turn decays into a ground state nucleon and one or more mesons. The helicity amplitudes are shown in red and the multipoles of the pion-nucleon system in blue. Details will be provided later in this section.

Resonance	Width, MeV	Contributing multipoles
$P_{33}(1232)$	118	$S_{1+}, E_{1+}, M_{1+}$
$P_{11}(1440)$ ( <i>Roper</i> )	300	$S_{1-}, M_{1-}$
$D_{13}(1520)$	115	$S_{2-}, E_{2-}, M_{2-}$
$S_{11}(1535)$	150	$S_{0+}, E_{0+}$
$D_{15}(1675)$	150	$S_{2+}, E_{2+}, M_{2+}$
$F_{15}(1680)$	130	$S_{3-}, E_{3-}, M_{3-}$

**Table 1.1:** Resonances masses and widths for selected well-established states (Ref [1]).

We use the spectroscopic notation  $L_{2I2J}$ , where  $L$  is the orbital momentum,  $I$  is the isospin, and  $J$  is the total spin of the state.

Exclusive meson electroproduction gives us an opportunity to extract the properties of the baryons from both combined and independent analysis of different channels.  $\pi^0$  electroproduction in particular is an attractive tool since it covers a lower invariant mass range, and is one of the major decay channels of many of the higher-mass resonance states.

The final goal of the reported analysis is to extract the electromagnetic transition form factors from a combined analysis of the reported  $\pi^0$  electroproduction channel with other meson production channels. This will enable us to robustly separate resonant and non-resonant mechanisms. The scope of this thesis is limited to the extraction of the  $\pi^0$  electroproduction cross sections, structure

functions and a Legendre multipole analysis. This study will give us insight to the properties of the accessible resonances (Table 1) and will demonstrate the suitability of this data for a next-level analysis.

The structure of this work is as follows: Chapter 2 contains the overview of the study of the strong interaction in the exclusive  $\pi^0$  production channel. Chapter 3 is fully dedicated to the experiment: Jefferson Lab accelerator and CEBAF Large Acceptance Spectrometer (CLAS) detector. Details of the analysis of the experimental data are described in the Chapter 4. Simulation to obtain the acceptance of the detector is presented in the Chapter 5, cross section and structure functions extraction are described in the Chapter 6. Physics analysis and discussion are outlined in the Chapter 7.

## Chapter 2

### Theory

#### 2.1 Strong interactions

##### 2.1.1 QCD

Huge success of the fundamental physics of the XX century is creation of the theory of the strong interaction. The QCD describes the strong interaction as the interaction of the most fundamental constituents of the matter known to date - quarks and gluons.

The QCD Lagrangian is written as

$$L = \bar{q}_{f,\alpha}(i\gamma^\mu\partial_\mu - m_f)q_{f,\alpha} - g(\bar{q}_{f,\beta}\gamma^\mu\frac{\lambda_{\beta\alpha}^c}{2})A_\mu^c - \frac{1}{4}F_{\mu\nu}^c F_c^{\mu\nu}, \quad (2.1)$$

where

$$F_{\mu\nu}^c = [\partial_\mu A_\nu^c - \partial_\nu A_\mu^c] - go_{cc'}A_\mu^{c'}A_\nu^{c''} \quad (2.2)$$

and

$$g^2/4\pi = \alpha_s(Q^2), \quad (2.3)$$

with

$$\alpha_s(Q^2) = \frac{12\pi}{(33 - 2n_F)\ln(Q^2/\Lambda^2)}, \quad (2.4)$$

where the fields  $\bar{q}_{f,\alpha}$  stands for quark fields of flavor  $f$  and color  $\alpha$ , while  $A_\nu^{c''}$  represent color fields,  $\lambda^c$  is an octet of Gell-Mann matrices and  $F_{\mu\nu}^c$  represents tensors of gluon fields.  $Q^2$  is square of the gluon four momenta, corresponding to the distance scale of  $1/\sqrt{Q^2}$ ,  $n_F$  - number of the flavors of the quarks equal to six, and  $\Lambda$  - the fundamental cut-off parameter of the QCD, approximately equal  $200 \text{ MeV}$ .

The first term in Eq. 2.1 corresponds to the part of the non-interaction quark fields. The two other terms describe strong interaction dynamics at the fundamental level: the second term originates the quark-gluon interaction, when a gluon, emitted by a quark, produces virtual quark-antiquark pair. This process is similar to the production of electron-positron pairs by a virtual photon in the Quantum Electrodynamics (QED).

The third term describes gluon part of the strong interaction Lagrangian. It is the part which makes the QCD fundamentally different with respect to the QED. The reason for this fundamental difference is the non-Abelian symmetry of the QCD. It results in a self-interaction of gluon fields, shown in Fig. 2.1.

The color screening and antiscreening described above are presented in Eq. 2.4 for the running coupling constant of the QCD. The first term in the differ-

ence in the denominator describes the color antiscreening due to processes from the gluon-gluon vertices (Fig. 2.1). The second term corresponds to the screening by  $q\bar{q}$  pairs. Since number of the flavors of the quarks is equal to six, the antiscreening process dominates, which leads to the increase of the QCD running constant with distance and dramatically changes its dynamics.

The dynamics of the strong interaction at the distances of the order of the nucleon size is completely different from the strong interaction in the perturbative regime. In the perturbative regime current quarks and gauge gluons are the once that participate in the strong interaction, while on the distance of the order of  $1\text{ fm}$  degrees of freedom of the strong interaction change to the constituent quarks and collective systems of many gluons.

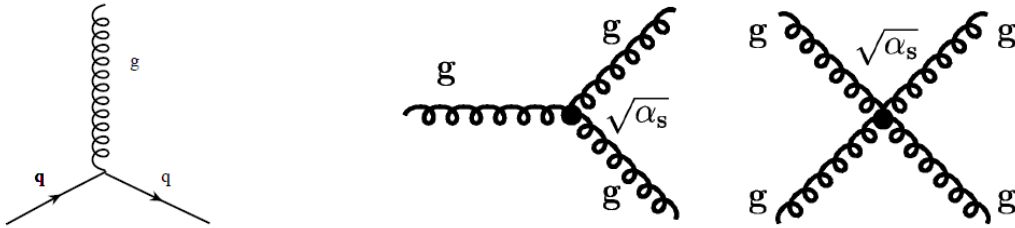


**Fig. 2.1:** The fundamental diagrams of the QCD. Two diagrams on the right shows self interaction of gluons.

### 2.1.2 Formation of hadrons

Baryons are the fundamental building blocks of the visible Universe and are governed by the strong interaction. The fundamental theory of this interaction is the Quantum Chromodynamics, and as such it gives the information about the principles obeyed by the hadron matter. It has current quarks and gauge gluons as the structureless fundamental degrees of freedom. At small distance of the order of  $10^{-2} fm$  the theory provides a good description of the fundamental quark-gluon interaction within the perturbative QCD framework. The question about how these gauge interactions between the bare current quarks and the gauge gluons are related to the hadron properties and hadron interactions of real world remains open and one of the most challenging problems of the contemporary hadron physics.

The fundamental uncertainty principle requires, that at the distance scale of less than  $1 fm$  bare quarks and gluons get dressed by the cloud of gluons and  $q\bar{q}$  pairs similarly to the dressing of electrons by photons and coupled with photons virtual  $e^+e^-$  pairs in QED (see Fig. 2.2)

However, dressing effects in the QED are suppressed by the small values of the electromagnetic coupling in the electron-photon vertices. Therefore, properties of dressed photons (electrons) are essentially determined by those of bare photons (electrons).

Different situation occurs in case of the strong interactions. The quark-gluon coupling increases with distance and at the distance scale  $> 10^{-1} fm$  dressing ef-

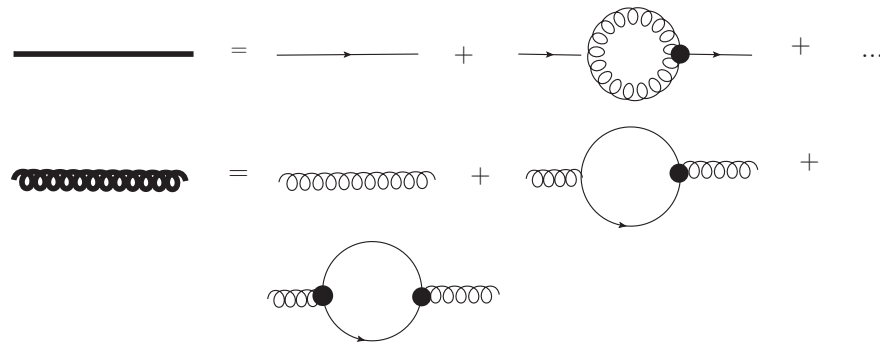


**Fig. 2.2:** Dressing of the bare quark (above) and the bare gluon (below) with a cloud of gluons and  $q\bar{q}$  pairs.

fects substantially determine properties of the dressed quarks and gluons. Combination of the growing with the distance effective quark-gluon coupling and shown in Fig. 2.2 dressing effects generate dynamical masses and structure of the dressed quarks and gluons which depend on distances. Furthermore, shown in Fig. 2.2 quark-gluon dressed vertices are also distance-dependent. At the distance scale more than  $10^{-1} fm$ , where the running quark-gluon coupling becomes large and comparable with unity, dynamics of the strong interaction in the non-perturbative regime becomes distance-dependent. The non-perturbative strong interaction dynamics can not be directly deduced from the fundamental QCD Lagrangian, since the interacting objects (dressed quarks and gluons) are different with respect to those in the QCD Lagrangian.

In the non-perturbative QCD regime dressed quarks and gluons interactions acquire qualitatively new features, including:

1. The dynamical generation of dressed quark/gluon masses, which accounts for more than 97% of nucleon mass;
2. The dynamical chiral symmetry breaking which manifests itself as a break of degeneracy in the baryon spectrum for the states with the opposite parities;
3. Confinement. No free colored quarks or gluons have been experimentally observed.

All these features determine the formation of baryons as the bound states of quarks and gluons. Therefore, the studies of the spectrum and structure of  $N^*$  offers a unique opportunity to access the full complexity of the non-perturbative strong interactions, which are responsible for the nucleon and  $N^*$  formations, and to explore how the non-perturbative strong interaction comes from the QCD.

Two conceptually different and based on the QCD approaches to describe a hadron structure, the Lattice QCD ([2]) and the Dyson-Schwinger Equation of QCD ([3, 4]), both predicted the pronounced dependencies of the dressed quark dynamical mass as a function of momentum, running over quark propagator, shown in Fig. 2.3. The computations were carried out for the different bare masses of the s-quark as well as in the chiral limit of the massless bare quarks. For all cases sharp increase of the dynamical quark running mass occurs when momentum becomes less than 2 GeV. Notably, this increase occurs even in the chiral limit of the massless bare quark.

The processes of the bare quarks dressing are also responsible for the Dynamical Chiral Symmetry Breaking (DCSB). DCSB determines the essence of the non-perturbative strong interaction, that is responsible both for the meson and baryon formation, allowing us to understand major features in the hadron spectra: low pion mass [6], lack of parity partners in the  $N^*$  spectrum [5], and the  $N^*$  state ordering [7].

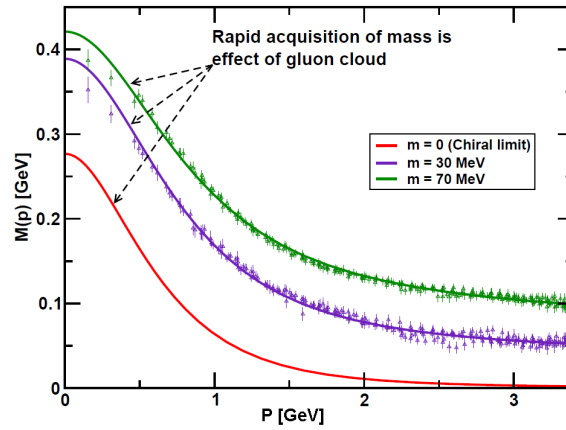


**Fig. 2.3:** Dressed quark mass function. The solid curves - DSE results, 'data' - numerical simulation of the LQCD. The current quark of the perturbative QCD evolving into constituent quark as its momentum drops. The constituent quark mass arises from a gluon cloud.

### 2.1.3 Lattice QCD

The lattice QCD (LQCD) is the numerical simulation of the theory of the strong interaction. Improvements in algorithms along with the increase in the compu-

tational power have enabled simulations to be carried out at the near physical parameters of the theory and opens up a possibility for an *ab initio* calculations of the experimentally known quantities.

Starting point to the LQCD calculation is definition of the theory on a four-dimensional Euclidean space-time lattice. The lattice spacing  $a$  provides an ultraviolet cutoff at the highest allowed momentum  $\pi/a$ . The gauge fields are determined as links  $U_\mu(n)$  between the adjacent lattices, and quarks are defined at each lattice site as the anticommuting Grassmann variables, belonging to the fundamental representation of the  $SU(3)$ . Using this fundamental degrees of freedom, one constructs an appropriate action such, that when  $a \rightarrow 0$  (and the total volume of the lattice  $\rightarrow \infty$ ) continuum theory is recovered. In order to extract the physical quantities, the construction of the appropriate operators with their normalization is carried out.

Although the LQCD results do not include any model assumption and are the direct QCD calculation, discretization of the space-time continuum and performing the numerical simulation on a finite volume introduce artifacts that may lead to the systematical errors, which need to be investigated before comparing to the experiment. Among them are: the finite volume (to study its effect one has to perform the calculations in different volumes); the finite lattice spacing (simulations for at least three values of the lattice spacing are needed to extrapolate to the continuum limit); the renormalization constants (computation of the

appropriate renormalization constants is needed to relate lattice matrix elements to continuum results); heavier than physical pion masses (current LQCD results are obtained using the simulations that are typically performed at heavier than physical pion masses, requiring the chiral extrapolation).

The recent result in the Lattice QCD, closely related to the scope of this work is the spectrum of the low-lying baryons which was recently computed. Nucleon and  $\Delta$  position are in agreement with the experimental data [10, 11].

## 2.2 Hadrons in the models of the strong interaction

There have been a numerous efforts to describe the electromagnetic properties of the nucleon and its excitation within the different hadron models using effective degrees of freedom.

The number of non-relativistic quark models, based on the SU(6) symmetry or some phenomenological interquark potential [12], capable of describing the static properties and decays of mesons and baryons, have intrinsic flaws - they treat quark motion as non-relativistic, the interquark potential is not very accurate and the gluon dynamics is neglected. Later attempts to build the relativistic quark models were aimed to resolve some of this issues.

The relativized quark model [13] uses the momentum-dependent interquark potential which includes spin-orbit and hyperfine interaction. The parameters (masses of the quarks, strength of the potential) of the model are the same be-

tween the baryon and meson side. Using variational method, authors calculate the energy eigenstates of the Hamiltonian and the corresponding eigenvalues. Importance of this approach is two-fold, since first it shows, that the relativization of the simpler quark model retains its predictive power in terms of the spectra of the baryons and second, it shows, that by using the constants from the meson sector one is still able to describe the baryon part satisfactory.

In the bag model, developed in the MIT by Chodos, Jaffe et al [14], the strongly interacting particle is confined in the finite volume of space in Lorentz-invariant way by attributing the region with a constant energy  $B$  per unit volume. The massless, spin- $\frac{1}{2}$  fields with the colored-quark quantum numbers are interacting with the massless, colored vector gluons. Even for the free quarks inside a volume there is no exact solution in three dimensions, so the quarks in the model occupy spherical cavities of fixed radius. In this case, the energy depends on which modes are occupied, and not on the way the total angular momentum or the isospin of the individual quarks are added to obtain the total angular momentum and the isospin of the system. The only free parameter of the model -  $B$ , is fixed by the average mass of  $N(938)$  and  $\Delta(1232)$ . The model allows to calculate the spectra of the low-lying non-strange resonances with  $J \leq \frac{3}{2}$ . It is also able to calculate the magnetic moment and the charge radius of proton and neutron.

The modification to the model, restoring the chiral symmetry, was introduction of the pion cloud, surrounding the original bag containing three quarks [15,

16]. The free parameter of model are the bag radius, which vary depending on particular approach in the range of  $R = 0.35 - 1 \text{ fm}$ . The obtained electromagnetic properties of nucleons - the charge radii of the  $p$  and  $n$  and their magnetic moments are in a good agreement with experiment. The axial-vector coupling constant is reproduced in both variations of the model and is in agreement with the experimental value.

The Skyrme model is a field theory, which introduces the self-interacting meson field in which particles appear as the non-dispersive wave packets, and the mesons are the bound states of such particle-antiparticle system. The nucleon in the model is the solution to the equation of the motion of the field [19]. The model is able to reproduce the static properties [17] of the nucleons as well as width of the  $\Delta$  decay, which is calculated to be 125 MeV (compared to the experimental value of 120 MeV). Introduction of the photoproduction into original model is done by adding term to the Lagrangian, corresponding to the coupling of the photon field to the original skirmion field. Calculations demonstrate, that the model predicts presence of the resonances in the second and third resonance region.

The dielectric model [23] considers formation of the flux tube between two quarks and then tube break-up with formation of two hadrons. To describe this behavior, the analogy to electrostatic interaction is used first, and a quark is treated as a free charge in a dielectric with a susceptibility  $\epsilon$  which may assume negative values. This allows to describe the tube formation and its energy density.

The real model includes three fields to describe the aforementioned properties: the Abelian gauge field which used to construct the gauge-invariant Maxwell field, the charged fermion field to be identified as quark, and the local dielectric susceptibility. In these conditions the fields create a long-range force, mediated by the flux tubes, which is screened by the production of the fermion pairs.

Study [22] uses the dielectric model above to perform the numerical lattice calculation of the relationship between the glueball mass and the string tension, as well as strength of the gluon condensate. Calculations achieve a good agreement with available data.

Another approach to get inside of the QCD on distance scale of the baryon structure is the Dyson-Schwinger equation (DSE) - set of the quantum field theory equations which relate the Green's functions of the theory to each other [24, 25]. It is a nonlinear integral equation, which in principle can yield much needed non perturbative information on the strong interaction without using model assumptions. Problem arises, that in order to have an exact solution we should solve the infinite number of the coupled equations. The current approach to the DSE is to truncate the series at some point and then introduce an ansatz to account for the truncated terms. There is also a hope to use the LQCD estimation for the truncated terms.

The calculations of the meson and baryon spectra within the DSE naturally connects meson and baryon observables with the QCD, and the current calcu-

lations, though obtained without accounting for the meson cloud effect, show interesting result for the Roper resonance: it is shown to be predominantly the radial excitation of the quark-diquark system with a strong contribution from a meson cloud.

## 2.3 Nucleon resonances

### 2.3.1 Introduction

The excitations of the nucleon resonances via the electromagnetic interactions is an important source of the information to understand the QCD in the region of the quark confinement [26]. The excited states of the nucleons -  $N^*$  were clearly seen as peaks in the energy dependence of the cross section of interaction of photons, electrons, negative pions and K-mesons with the nucleons.

The ground state and the excited states of the nucleon are formed by the same Hamiltonian of the strong interaction, hence, to study this Hamiltonian we need the information on both the ground and excited states. Resonance features significantly changes with the  $Q^2$  and the evolution of close in energy peaks can be very different, since such an evolution depends on the quantum numbers of the contributing resonances. The  $Q^2$  evolution of the non-resonant part can be well described within the QCD-based approaches, while these approaches fail to describe the  $Q^2$  evolution of the individual resonance peaks. So, data on the electromagnetic form factors provides the complimentary information to the one we

get from the study of the ground state of the nucleon. The experimentally obtained electromagnetic transitional form factors of the  $N^*$  are purely phenomenological, and has to be connected to the fundamental mechanisms of the QCD. The most promising approaches to that are described above - the lattice QCD and the DSE approaches, which as of now are able to predict some of the properties of resonance spectra and transitions from the first principles.

### 2.3.2 Formalism

We need to build a connection between the quantities we measure experimentally and the physical properties of the resonances to be theoretically interpreted. Experimentally accessible characteristic of the  $\pi^0$  electroproduction process (Fig. 2.4) is the cross section, which in the one photon approximation can be related to the differential cross section of the production of the pions by virtual photons as written in Eq. 2.5:

$$\frac{d\sigma}{dE_f d\Omega_e d\Omega_{\pi^0}^*} = \Gamma \frac{d\sigma}{d\Omega_{\pi^0}}, \quad (2.5)$$

where

$$\Gamma = \frac{\alpha}{2\pi^2 Q^2} \frac{(W^2 - m^2) E_f}{2m E_i} \frac{1}{1 - \epsilon}, \quad (2.6)$$

$$\epsilon = [1 + 2(1 + \frac{\nu^2}{Q^2} \tan^2) \frac{\theta_e}{2}]^{-1}, \quad (2.7)$$

$\alpha$  is the fine structure constant,  $E_i$  and  $E_f$  are initial and final electron energies in the laboratory frame,  $\nu = E_i - E_f$ ,  $\epsilon$  is polarization factor of the virtual

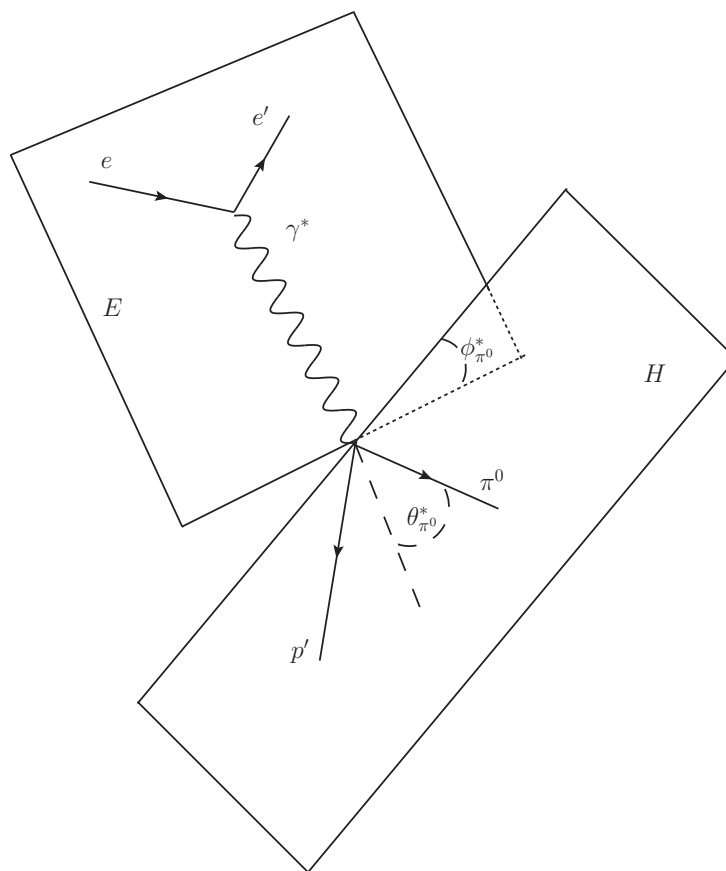


**Fig. 2.4:**  $\pi^0$  electroproduction schematic.  $E$  is the electron scattering plane,  $H$  is the hadron production plane.

photon,  $\Omega_e = \Omega_e(\theta_e, \phi_e)$  is laboratory solid angle of the scattered electron and  $\Omega_{\pi^0}^* = \Omega_{\pi^0}^*(\theta_{\pi^0}^*, \phi_{\pi^0}^*)$  is the pion solid angle in the center of mass system (CMS) of the reaction  $\gamma^* N \rightarrow N\pi$  with  $\theta_{\pi^0}^*$  - angle between pion and virtual photon in this system, and  $\phi_{\pi^0}^*$  is the angle between electron scattering and hadron production planes (see Fig. 2.5). Virtuality of photon  $k^2 = \nu^2 - \mathbf{k}^2$  is negative and it is more convenient to introduce the positive  $Q^2 \equiv -k^2$ . Invariant mass of the final hadronic state  $W = (p + k)^2 = m^2 + 2m\nu - Q^2$ , where  $p$  and  $k$  are the target nucleon and virtual photon four momenta and  $m$  is the nucleon mass.

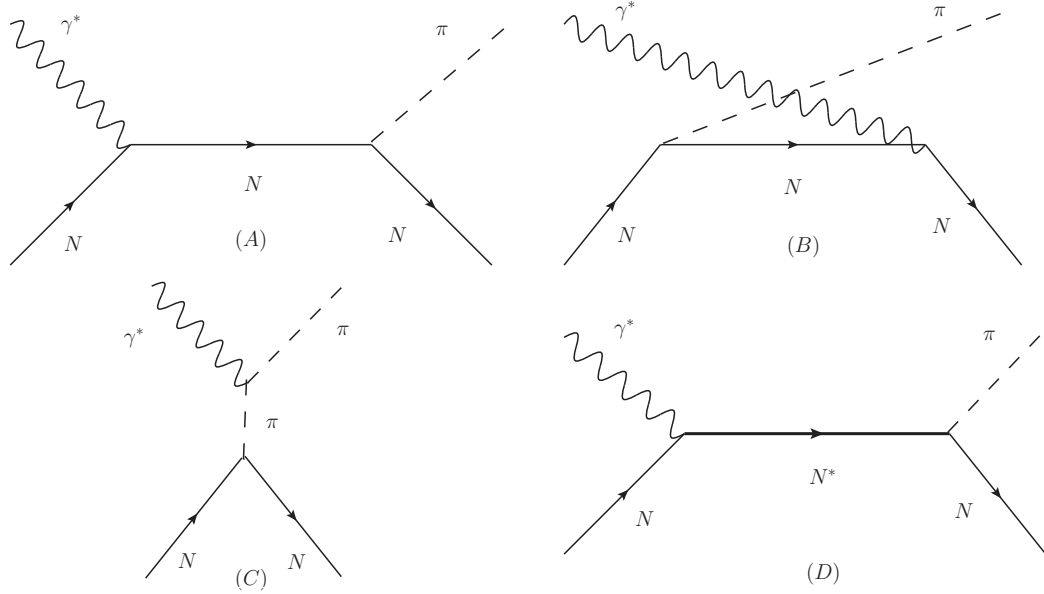


**Fig. 2.5:** Diagrams corresponding to non-resonant (A), (B) and (C), and resonant (D) contributions to  $\pi^0$  electroproduction.

For the unpolarized particles and unpolarized electron beam the  $\phi$ -dependence

of the cross section can be represented in the following way:

$$\frac{d\sigma}{d\Omega_{\pi^0}^*} = \frac{2Wp_{\pi^0}}{W^2 - m_P^2} (\sigma_T + \epsilon\sigma_L + \epsilon\sigma_{TT}\sin^2\theta_{\pi^0}^*\cos 2\phi_{\pi^0}^* + \sqrt{2\epsilon(1+\epsilon)}\sigma_{LT}\sin\theta_{\pi^0}^*\cos\phi_{\pi^0}^*) \quad (2.8)$$

where  $\sigma_T, \sigma_L, \sigma_{TT}$  and  $\sigma_{LT}$  are structure functions of the reaction  $\gamma^*N \rightarrow N\pi$  that depend on the  $W, Q^2$  and  $\cos\theta_{\pi^0}^*$ . In order to extract the resonance contribution from the  $\gamma^*N \rightarrow N\pi$  the observables should be defined through the multipole amplitudes: transverse amplitudes  $M_{l\pm}, E_{l\pm}$  and scalar (longitudinal) amplitudes  $S_{l\pm}$  (related to  $L_{l\pm} = k_0 S_{l\pm}/|\mathbf{k}|$ ), which are related respectively to the photons of magnetic, electric and Coulomb type with  $l$  - angular momentum of the pion in the CMS of the reaction  $\gamma^*N \rightarrow N\pi$  (Fig. 2.6). We will introduce transverse partial wave helicity amplitudes:

$$A_{l+} = \frac{1}{2}[(l+2)E_{l+} + lM_{l+}], \quad (2.9)$$

$$B_{l+} = E_{l+} - M_{l+}, \quad (2.10)$$

$$A_{l+1} = \frac{1}{2}[(l+2)M_{(l+1)-} - lE_{(l+1)-}], \quad (2.11)$$

$$A_{(l+1)-} = \frac{1}{2}[(l+2)M_{(l+1)-} - lE_{(l+1)-}], \quad (2.12)$$

$$B_{(l+1)-} = E_{(l+1)-} + M_{(l+1)-}. \quad (2.13)$$

The amplitudes  $A_{l\pm}, B_{l\pm}$  and  $S_{l\pm}$  are related to the  $\gamma^*N \rightarrow N\pi$  helicity

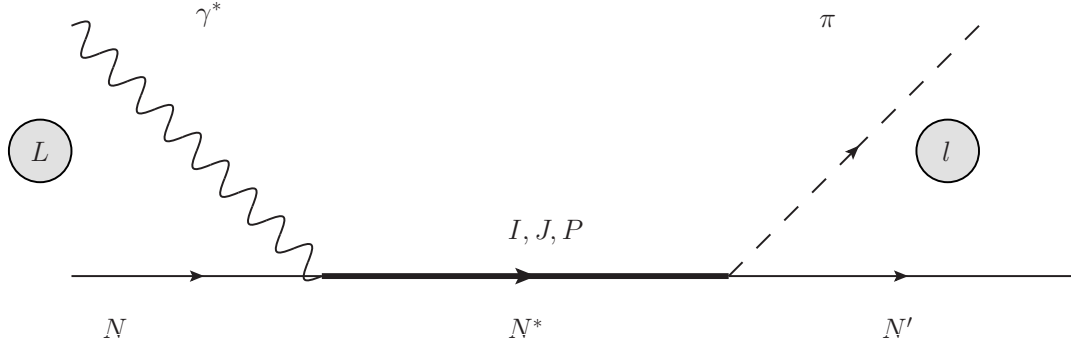


**Fig. 2.6:** Multipole notation for the pion photoproduction. The photon with orbital angular momentum  $L$  excites the  $N^*$  state with isospin  $I$ , spin  $J$  and parity  $P$  which then decays into pion with orbital angular momentum  $l$  and nucleon.

amplitudes in the CMS of the reaction in the following way:

$$H_1 = \frac{1}{\sqrt{2}} \sin\theta \cos\frac{\theta}{2} \sum (B_{l+} - B_{(l+1)-}) [P'_l(\cos\theta) - P'_{l+1}(\cos\theta)], \quad (2.14)$$

$$H_2 = \sqrt{2} \cos\frac{\theta}{2} \sum (A_{l+} - A_{(l+1)-}) [P'_l(\cos\theta) - P'_{l+1}(\cos\theta)], \quad (2.15)$$

$$H_3 = \frac{1}{\sqrt{2}} \sin\theta \sin\frac{\theta}{2} \sum (B_{l+} + B_{(l+1)-}) [P'_l(\cos\theta) + P'_{l+1}(\cos\theta)], \quad (2.16)$$

$$H_4 = \sqrt{2} \cos\frac{\theta}{2} \sum (A_{l+} + A_{(l+1)-}) [P'_l(\cos\theta) + P'_{l+1}(\cos\theta)], \quad (2.17)$$

$$H_5 = \frac{Q}{|\mathbf{k}|} \sin\frac{\theta}{2} \sum (l+1)(S_{l+} + S_{(l+1)-}) [P'_l(\cos\theta) - P'_{l+1}(\cos\theta)], \quad (2.18)$$

$$H_6 = \frac{Q}{|\mathbf{k}|} \cos\frac{\theta}{2} \sum (l+1)(S_{l+} - 5S_{(l+1)-}) [P'_l(\cos\theta) + P'_{l+1}(\cos\theta)], \quad (2.19)$$

where  $H_1 \dots H_6$  are the elements of the matrices  $H_{\mu 2 \mu 1}$ ,

$$\lambda_\gamma = 1 : \begin{pmatrix} H_4 & H_3 \\ H_2 & H_1 \end{pmatrix}$$

$$\lambda_\gamma = -1 : \begin{pmatrix} H_1 & -H_2 \\ -H_3 & H_4 \end{pmatrix}$$

$$\lambda_\gamma = -0 : \begin{pmatrix} -H_5 & H_6 \\ H_6 & H_5 \end{pmatrix}$$

,

the structure functions in equation 2.8 are related to the helicity amplitudes  $H_1 \dots H_6$  by

$$\sigma_T = \frac{\mathbf{q}}{2K} (|H_1|^2 + |H_2|^2 + |H_3|^2 + |H_4|^2), \quad (2.20)$$

$$\sigma_L = \frac{\mathbf{q}}{K} (|H_5|^2 + |H_6|^2), \quad (2.21)$$

$$\sigma_{TT} = \frac{\mathbf{q}}{K} (H_3 H_2^* - H_4 H_1^*), \quad (2.22)$$

$$\sigma_{LT} = -\frac{\mathbf{q}}{\sqrt{2}K} \text{Re}[(H_1 - H_4)H_5^* + (H_2 + H_3)H_6^*], \quad (2.23)$$

$$(2.24)$$

where  $K = \frac{W^2 - m^2}{2W}$ ,  $\mathbf{k}$  and  $\mathbf{q}$  are, respectively, the photon equivalent energy, the virtual photon and pion 3-momenta in the  $\gamma^* N \rightarrow N\pi$  CMS.

The  $\gamma^* N \rightarrow N\pi$  total cross section can be rewritten through partial wave

helicity amplitudes as

$$\sigma^{tot} = \sigma_{1/2} + \sigma_{3/2} + \epsilon\sigma_L^{tot}, \quad (2.25)$$

$$\sigma_{1/2} = 2\pi \frac{|\mathbf{q}|}{K} \sum 2(l+1)[|A_{l+}|^2 + |A_{(l+1)-}|^2], \quad (2.26)$$

$$\sigma_{3/2} = 2\pi \frac{|\mathbf{q}|}{K} \sum \frac{l}{2}(l+1)(l+2)[|B_{l+}|^2 + |B_{(l+1)-}|^2], \quad (2.27)$$

$$\sigma_L^{tot} = 4\pi \frac{|\mathbf{q}|}{K} \sum \frac{Q^2}{\mathbf{k}^2}(l+1)^3[|S_{l+}|^2 + |S_{(l+1)-}|^2]. \quad (2.28)$$

Experimental results on the  $\gamma^*N \rightarrow N^*$  helicity amplitudes (transverse  $A_{1/2}$  and  $A_{3/2}$  and longitudinal (or scalar)  $S_{1/2}$ ), extracted from the data on  $\gamma^*N \rightarrow N\pi$  correspond to the contribution of the diagram  $D$  (Fig. 2.5) to this reaction. They are related to the resonance portions of the corresponding multipole amplitudes at the resonance position in the following way:

$$A_{1/2} = \mp \hat{A}_{l\pm}, \quad (2.29)$$

$$A_{3/2} = \pm \sqrt{\frac{(2J-1)(2J+3)}{16}} \hat{B}_{l\pm}, \quad (2.30)$$

$$A_{1/2} = -\frac{2J+1}{2\sqrt{2}} \hat{S}_{l\pm}, \quad (2.31)$$

where

$$\hat{A}_{l\pm}(\hat{B}_{l\pm}, \hat{S}_{l\pm}) \equiv aImA_{l\pm}^R(B_{l\pm}^R, S_{l\pm}^R)(W=M), \quad (2.32)$$

$$a \equiv \frac{1}{C_I} [(2J+1)\pi \frac{|\mathbf{q}|_r}{K_r} \frac{M}{m} \frac{\Gamma}{\beta_{\pi N}}], \quad (2.33)$$

$\Gamma$ ,  $M$ ,  $J$  and  $I$  are total width, mass spin and isospin of the resonance  $J = L \pm \frac{1}{2}$  for  $l\pm$  amplitudes,  $\beta_{\pi N}$  is the branching ratio of the resonance to the pion channel  $K_r$  and  $|\mathbf{q}_r|$  are the photon equivalent energy and the pion 3-momentum at the

resonance position in the CMS of the  $\gamma^* N \rightarrow N\pi$ , and  $C_I$  are the isospin Clebsch-Gordon coefficients in the decay  $N^* \rightarrow \pi N$ :

$$C_{1/2} = -\sqrt{\frac{1}{3}}, C_{3/2} = \sqrt{\frac{2}{3}}. \quad (2.34)$$

Many theoretical approaches, among them the Lattice QCD, use the definition of the  $\gamma^* N \rightarrow N\pi$  helicity amplitudes in terms of the resonance transitional form factors. For the  $J^P = \frac{1}{2}^\pm$  resonances the definition for the  $\langle N^* | J_{em}^\mu | N \rangle$  matrix element is

$$\langle N^* | J_{em}^\mu | N \rangle \equiv e\bar{u}(p^*) \begin{pmatrix} 1 \\ \gamma_5 \end{pmatrix} \tilde{J}_\mu u(p), \quad (2.35)$$

$$\tilde{J}_\mu = [k k_{mu} - k^2 \gamma_{mu}] G_1(Q^2) + [k P_{mu} - (Pk) \gamma_{mu}] G_2(Q^2), \quad (2.36)$$

where  $P \equiv \frac{1}{2}(p^* + p)$ . The relation between the  $\gamma^* N \rightarrow N^*$  helicity amplitudes and the form factors  $G_1(Q^2)$ ,  $G_2(Q^2)$ :

$$\tilde{A}_{1/2} = b[2Q^2 G_1(Q^2) - (M^2 - m^2) G_2(Q^2)], \quad (2.37)$$

$$\tilde{S}_{1/2} = \pm \frac{|\mathbf{k}|}{\text{sqr}t{2}} [2(M \pm m) G_1(Q^2) + (M \mp m) G_2(Q^2)] \quad (2.38)$$

$$b \equiv e \sqrt{\frac{(M \mp m)^2 + Q^2}{16mMK_r}}. \quad (2.39)$$

The equations for other  $J^P$  are more complicated and can be found in [26].

### 2.3.3 Theoretical approaches for the analysis of the pion electroproduction

There is a number of approaches to analyze the experimental data with the common formalism for the pion photoproduction developed in the [27] (CGLN amplitudes). This work used the fixed-t dispersion relations (DR) to analyze the reaction. The CGLN formalism and DR were later extended to pion electroproduction [28].

The basis for another widely used approaches, the isobar model and the effective Lagrangian description, were originally developed in the [30] and [31] respectively. The isobar model parametrizes the resonance contribution to the partial waves with the Breit-Wigner distribution with the energy-dependent partial widths  $\Gamma_\gamma$  and  $\Gamma_\pi$ .

The Unitary Isobar Model (UIM) was developed in the [32] with the following separation of the background and resonance terms: the background includes the Born and vector mesons exchange terms, while the resonance part has a Breit-Wigner energy dependence. The electromagnetic vertices of the processes (Fig. 2.5)  $\gamma NN$  and  $\gamma\pi\pi$  have a well defined structure:

$$L_{\gamma NN} = -e\bar{\psi}[\gamma_\mu A^\mu F_1^{p,n}(Q^2) + \frac{\sigma_{\mu\nu}}{2m_N}\partial^{mu} A^\nu F_2^{p,n}(Q^2)]\psi, \quad (2.40)$$

$$L_{\gamma NN} = e[(\partial_\mu \boldsymbol{\pi})^\dagger \times \boldsymbol{\pi}]A^\mu F_\pi(Q^2), \quad (2.41)$$

where  $A^\mu$  is electromagnetic vector potential,  $\psi$  and  $\boldsymbol{\pi}$  are the nucleon and pion

field operators, respectively. Note the explicit  $Q^2$  dependence of the electromagnetic form factors.

The description of the hadronic  $\pi NN$  system is more sophisticated part of the theory of the photo- and electroproduction. There are two possibilities for the construction of the Lagrangian, the pseudoscalar (PS):

$$L_{\pi NN}^{PS} = ig\bar{\psi}\gamma_5\boldsymbol{\tau}\dot{\psi}\boldsymbol{\pi} \quad (2.42)$$

and the pseudovector (PV):

$$L_{\pi NN}^{PV} = -\frac{f}{m_\pi}\bar{\psi}\gamma_5\boldsymbol{\gamma}_\mu\boldsymbol{\tau}\dot{\partial}^\mu\boldsymbol{\pi}\psi, \quad (2.43)$$

where  $g^2/4\pi = 14.28$  and  $f/m_\pi = g/2m_N$ . At lower pion energies the PV coupling is to be preferred, while at higher energies it has a problem with the renormalization and the PS model leads to the better description. The approach of the model is to use a hybrid Lagrangian in the form

$$L_{\pi NN}^{HM} = \frac{\Lambda_m^2}{\Lambda_m^2 + \mathbf{q}_0^2}L_{\pi NN}^{PV} + \frac{\mathbf{q}_0^2}{\Lambda_m^2 + \mathbf{q}_0^2}L_{\pi NN}^{PS}, \quad (2.44)$$

where  $\mathbf{q}_0$  is the asymptotic pion momentum in the  $\pi N$  frame which depend only on  $W$ . The most appropriate value for the mixing parameter is established to be  $\Lambda_m = 450MeV$ .

There are also terms in the effective Lagrangian which correspond to the vector meson ( $\omega$ ,  $\rho$ ) contribution which in general are dominated by the Born term but can be important for some multipoles (see [32] for more details).

The resonance contributions to the multipole amplitude are written assuming the Breit-Wigner energy dependence of the form

$$aA_{l\pm}^R(B_{l\pm}^R, S_{l\pm}^R) = \hat{A}_{l\pm}(\hat{B}_{l\pm}, \hat{C}_{l\pm}) \frac{M\Gamma_{tot}e^{i\phi}}{M^2 - W^2 - iM\Gamma_{tot}} f_{\gamma N}(W), \quad (2.45)$$

where  $a$  and the  $\gamma^*N \rightarrow N$  helicity amplitudes  $\hat{A}_{l\pm}$ ,  $\hat{B}_{l\pm}$  and  $\hat{C}_{l\pm}$  are defined in Eq. 2.33,  $\phi \equiv \phi(W, Q^2)$  are the phases, which are found empirically for each resonances, and  $f_{\gamma N}(W)$  defines the  $W$  dependence of the  $\gamma^*NN^*$  vertex beyond the resonance peak. The fitting parameters of the model are the helicity amplitudes  $\hat{A}_{l\pm}$ ,  $\hat{B}_{l\pm}$  and  $\hat{C}_{l\pm}$  and the phases  $\phi(W, Q^2)$ .

The UIM of the reference [33] is based on the MAID model [32] with the incorporation of the Regge poles into the background amplitudes with increasing energies:

$$Background = [N + \pi + \rho + \omega]_{UIM} \text{ at } s < s_0 \quad (2.46)$$

$$= [N + \pi + \rho + \omega]_{UIM} \frac{1}{1 + (s - s_0)^2} + Re[\pi + \rho + b_1 + a_2]_{Regge} \frac{(s - s_0)^2}{1 + (s - s_0)^2} \text{ at } s > s_0. \quad (2.47)$$

The Regge-pole amplitudes are constructed using the Regge-trajectory exchange model and consist of reggezide  $\pi$ ,  $\rho$ ,  $\omega$ ,  $b_1$ , and  $a_2$  contributions in the t-channel. The value of  $s_0 = 1.2 \text{ GeV}^2$  was found from the description of the SAID multipole amplitudes. The good description of the  $\pi^+$  electroproduction

data was obtained at  $Q^2 = 0.4$  and  $0.65 \text{ GeV}^2$  in the first, second and third resonance region [40], [41].

The dispersion relation (DR) connects the real part of the eight invariant amplitudes  $B_i(s, t, Q^2)$  for the reaction  $\gamma^*N \rightarrow \pi N$ , defined according to the definition of the hadron EM current  $I^\mu$  ([42]):

$$I^{mu} = I'^{mu}u(p)\phi_\pi, \quad (2.48)$$

$$I'^{mu} = \frac{B_1}{2}[\gamma^{mu}\not{k} - \not{k}\gamma^{mu}] + 2P^\mu B_2 \\ + 2q^\mu B_3 + 2k^{mu}B_4 - \gamma^\mu B_5 + \not{k}P^\mu B_6 + \not{k}k^{mu}B_7 + \not{k}q^{mu}B_8, \quad (2.49)$$

to their imaginary parts, where  $B_i(s, t, Q^2), i = 1, 2 \dots 8$  are invariant amplitudes that are functions of the invariant variables  $s = (k+p)^2$ ,  $t = (k-q)^2$ ,  $P \equiv \frac{1}{2}(p+p')$  and  $u(p), U(p')$  are the Dirac spinors of the initial and final nucleons and  $\phi_\pi$  is the pion field.

The conservation of current leaves only six independent amplitudes, usually chosen to be:  $B_1, B_2, B_3, B_5, B_6$  and  $B_8$ . The dispersion relation defines the real part of the amplitudes  $B_1 \dots B_8$  through integral of their imaginary parts, reducing the construction of the  $\gamma^*N \rightarrow \pi N$  amplitudes to their imaginary parts. The SAID analysis of the world data on the pion photoproduction shows that the imaginary parts of the multipole amplitudes for  $W < 2 \text{ GeV}$  are determined dominantly by the resonance contribution. A good description of the imaginary parts of the amplitudes at  $W > 1.3 \text{ GeV}$  can be obtained using resonance parametrization of the Breit-Wigner form. At lower  $W$  the imaginary parts of the amplitudes

can have significant non-resonant contributions and can be described by using the DR to calculate their real part and then applying the Watson theorem for the construction of the imaginary part:

$$ImM(W, Q^2) = \frac{\sin\delta}{\cos\delta} ReM(W, Q^2). \quad (2.50)$$

The SAID model [43] is a T-matrix approach to extract  $N^*$  parameters by fitting the resulting amplitude  $T_{\gamma N, \pi N}$  near the resonance position using the Breit-Wigner parametrization of the resonance contribution. The  $Q^2$  dependence of the extracted parameters are accounted for using additional factors.

#### 2.3.4 Properties of the selected resonances

Each resonance in the covered region has some unique and interesting features which we will discuss below.

Extensively studied in both neutral and charged pion production channels,  $\Delta$  resonance has the following multipole content (see Table 1):  $M_{1+}$ ,  $E_{1+}$  and  $S_{1+}$ . Historically, it has been studied in terms of magnetic-dipole transition form factors,  $G_E$ ,  $G_M$ , and  $G_S$ . They correspond to  $E$ ,  $M$ , or  $S$  multipoles. The  $G_E$  and  $G_S$  values are small compared to the dominant  $G_M$ , so their ratios to the  $G_M$  ( $R_{EM}$  and  $R_{SM}$ , respectively) are usually presented.

The  $Q^2$  region, covered in this analysis, is shown to be very sensitive to the contribution of the meson cloud (Fig. 2.7, left panel). The different calculations of the  $R_{EM}$ , obtained in the large- $N_c$  limit of QCD (Fig. 2.7, right panel), show

different values and  $Q^2$  evolution at the  $Q^2 < 1 \text{ GeV}^2$ .

The Constituent Quark Model (CQM) [94] predicts both the  $R_{EM}$  and  $R_{SM}$  to be zero, while experimental data show significant negative values for both ratios. A satisfactory description of  $R_{EM}$  and  $R_{SM}$  is achieved in the models which includes contribution from the meson cloud [15, 16].

The Roper, or  $P_{11}(1440)$ , is the lowest excited state of the nucleon. The internal structure of the resonance has been a puzzle for many years. First calculation of the non-relativistic CQM could not reproduce the mass or width of the resonance. More recent attempts treat the resonance as the  $3q$  state with  $qqq\bar{q}$  components, or as a hybrid state  $qqqG$ . Results from the CLAS data on the helicity amplitudes of the Roper resonance [62, 63] helped to rule out  $qqqG$  hypothesis and supported the representation of the  $P_{11}(1440)$  as the first radial excitation of the system of three quarks with a strong effect from the meson cloud.

The CLAS results on the  $S_{1/2}$  amplitude, extracted from  $\pi^+$  and  $\pi^+\pi^-$  electroproduction channels, demonstrate different evolution in the region of  $Q^2 < 1 \text{ GeV}^2$ . The trend of nearly constant behavior from the single pion data is in the contradiction with the model calculations (Fig. 2.8).

Interesting feature of the  $S_{11}(1535)$  resonance is a slow fall-off of  $A_{1/2}$  amplitude, observed in both single pion and  $\eta$  electroproduction channels from the CLAS data. The model predictions for both the  $A_{1/2}$  and  $S_{1/2}$  helicity amplitudes, including the sign for the latter, are very diverse (Fig. 2.9), especially in the  $Q^2$

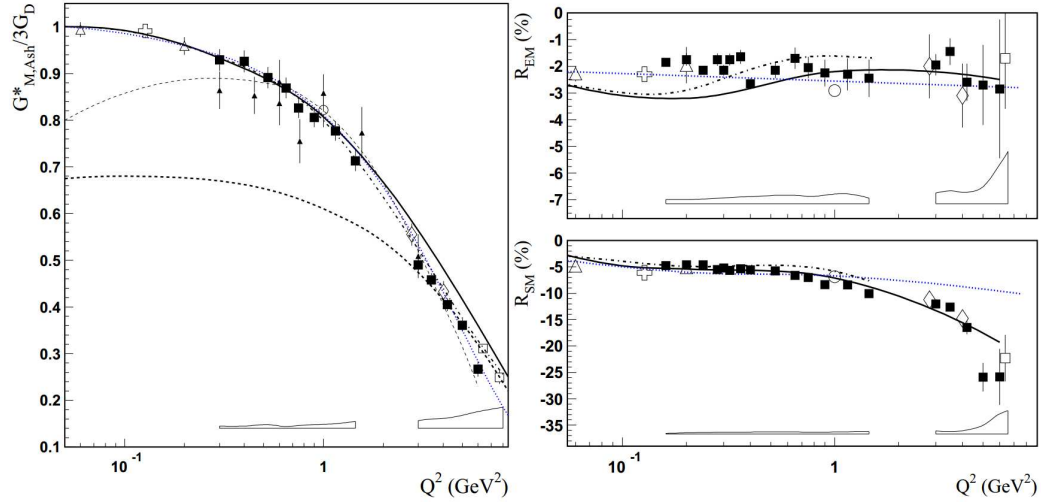


**Fig. 2.7:** Left: form factor  $G^*(Q^2)$  for the  $\gamma^* \rightarrow \Delta(1232)$  transition relative to the  $3G_D(Q^2)$ ,  $G_D(Q^2) = 1/(1 + \frac{Q^2}{0.71\text{GeV}^2})$ . Right: ratios  $R_{EM}$ ,  $R_{SM}$  [39]. The full boxes and uncertainties are from the JLab analysis [63]. The results of the Mainz group analysis using the MAID2007 [57] are shown by dotted curves. MAMI [52], [53]- open triangles, MIT/Bates ([54], [55], [56]) - open crosses; JLab/Hall C ([50]) - open rhombuses, JLab/Hall C [51] - open boxes, JLab/Hall A [45, 46] - open circles. The older results from NINA [69] and MAMI [70], [71] are shown in full triangles. The solid and dashed curves are dressed and bare contributions from [72], for  $R_{EM}$  and  $R_{SM}$  only dressed contributions are shown. The dashed-dotted and thin dashed lines are obtained in the large- $N_c$  limit of QCD of Refs [73, 74, 75].

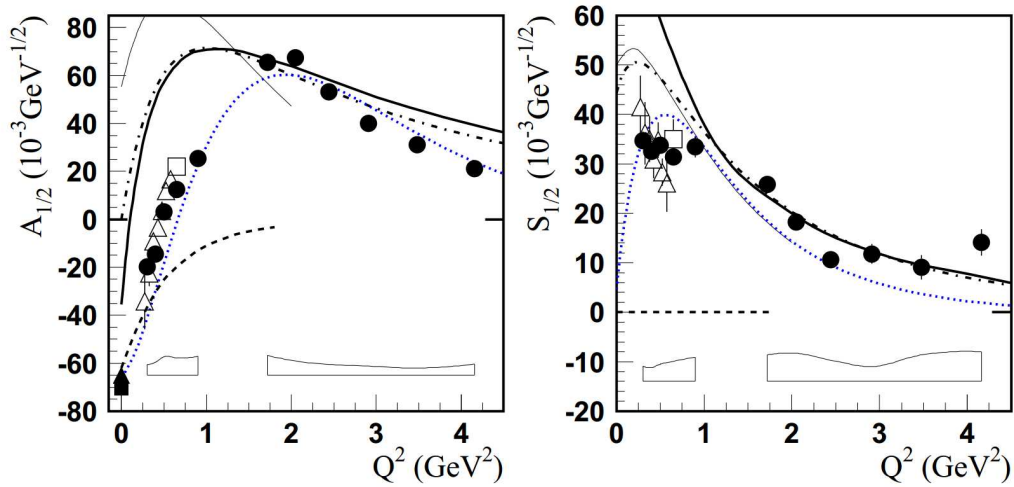


**Fig. 2.8:** Helicity amplitudes for the  $\gamma^* N \rightarrow N(1440)P_{11}$  transition [39]. The full circles and uncertainty bands are from the Jlab analysis [62], [63]. The results of the Mainz group analysis using the MAID2007 [57] are shown by dotted curves. The solid box at  $Q^2 = 0$  is the result extracted from the pion photoproduction data [76]. The results above correspond to the  $M = 1440$  MeV,  $\Gamma_{tot} = 350$  MeV,  $\beta_{\pi N} = 0.6$ . The solid triangle at  $Q^2 = 0$  is the RPP estimate [77]. The open boxes are from the combined analysis of CLAS single and double pion electroproduction data [41]. The open triangles are from CLAS  $2\pi$  electroproduction data with  $\beta_{2\pi N} = 0.4$  [64]. The solid and dashed-dotted curves are obtained in the LF relativistic quark model [78] and the covariant spectator quark model [79] assuming that the Roper resonance is a first radial excitation of the  $3q$  ground state. The thin solid curves are non-relativistic quark model predictions from [67]. The dashed curves are obtained assuming that the  $N(1440)P_{11}$  is a gluonic baryon excitation ( $q^3G$  hybrid state) [67].

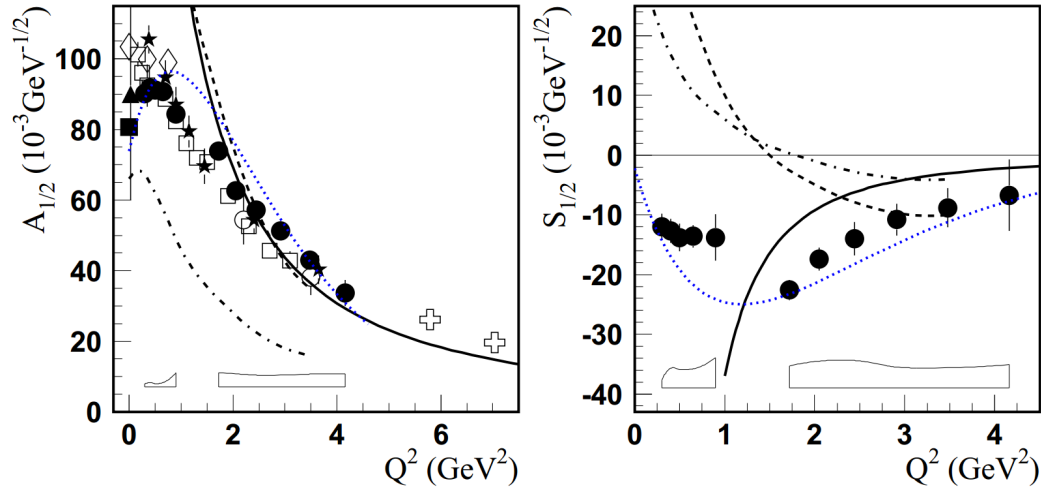


**Fig. 2.9:** Helicity amplitudes for the  $\gamma^* N \rightarrow N(1550)S_{11}$  transition [39]. For the amplitudes from the single pion channels the legend is the same as on the Fig. 2.8. The amplitudes from the  $\eta$  electroproduction: the stars [80], the open boxes [81], open circles [82], the crosses [83] and the rhombuses [40], [84]. The dashed and dashed-dotted curves show predictions of LF relativistic quark models [85] and [86] respectively. The solid lines show the amplitudes found within light-cone sum rules using lattice results for the light-cone distribution amplitudes of the  $N(1535)S_{11}$  resonance [87].

region of this experiment. The structure of the resonant state is an open question. Considered possibilities include strong effect from the meson cloud and admixture of the  $s\bar{s}$  to the  $qqq$  state.

The helicity amplitudes of  $D_{13}(1520)$  are extracted from the CLAS data on  $\pi^+$  and  $\pi^+\pi^-$  channels, and shown in Fig 2.10. The sign and the overall shape of all three amplitudes  $A_{1/2}$ ,  $A_{3/2}$  and  $S_{1/2}$  are described in general, though at

the  $Q^2 \approx 0.5 \text{ GeV}^2$  there is a significant shortfall in the quark models predictions with regard to the  $A_{3/2}$ . This shortfall may be an indication of the strong meson cloud effects. Another characteristic feature of this resonance is the change of the dominant amplitude: the  $A_{3/2}$  is more important at the  $Q^2 < 0.6 \text{ GeV}^2$ , however at the higher photon virtuality the  $A_{1/2}$  plays a leading role.

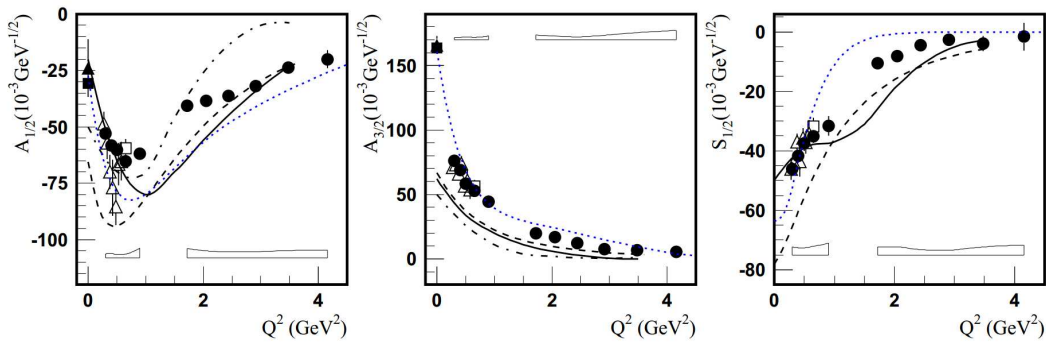


**Fig. 2.10:** Helicity amplitudes for the  $D_{13}(1520)$  state. The full boxes and circles are from the Jlab analysis [62, 63]. The results of the Mainz group analysis using the MAID2007 [57] are shown by dotted curves. MAMI [52, 53] - open triangles, [51] - open boxes. The older results from NINA [69] and MAMI [70, 71] are shown in full triangles. Curves are different model predictions.

Existing information on the higher-lying resonances is rather limited. The  $A_{1/2}$  and  $A_{3/2}$  amplitudes of the  $F_{15}(1680)$ , shown in Fig 2.11, behave similarly to the  $D_{13}(1520)$  and demonstrate same “helicity switch”, meaning that at the  $Q^2$  of the order of  $1 \text{ GeV}^2$  the relative importance of the amplitudes switches. The model predictions for the  $A_{3/2}$  at lower  $Q^2$  are in disagreement from the MAID

Facility	$Q^2, GeV^2$	W, GeV	Reference
JLab/Hall A	1.0	1.1-1.95	[44]
	1.0	1.17-1.35	[46]
JLab/Hall B	0.16 - 0.36	1.1 - 1.38	[47]
	0.4 - 1.8	1.1 - 1.68	[48]
	3.0 - 6.0	1.1 - 1.39	[49]
JLab/Hall C	2.8, 4.2	1.115 - 1.385	[50]
	6.4, 7.7	1.11 - 1.39	[51]
MAMI	0.06 - 0.2	1.22 - 1.3	[52], [53]
MIT-Bates	0.127	1.23	[54], [55], [56]

**Table 2.1:** Existing data on the  $\pi^0$  electroproduction cross sections from different facilities.

calculations.

### 2.3.5 Current state of the data and analysis

Existing measurements of the  $\pi^0$  electroproduction cross sections are summarized in the table 2.1. Substantial part of the measurements is concentrated in the first resonance region, they also cover the second region and touch the higher-lying resonance states. The present analysis will cover the region up to  $W = 1.8$  GeV with  $Q^2 = 0.4 - 1.0$   $GeV^2$  and full angular coverage.

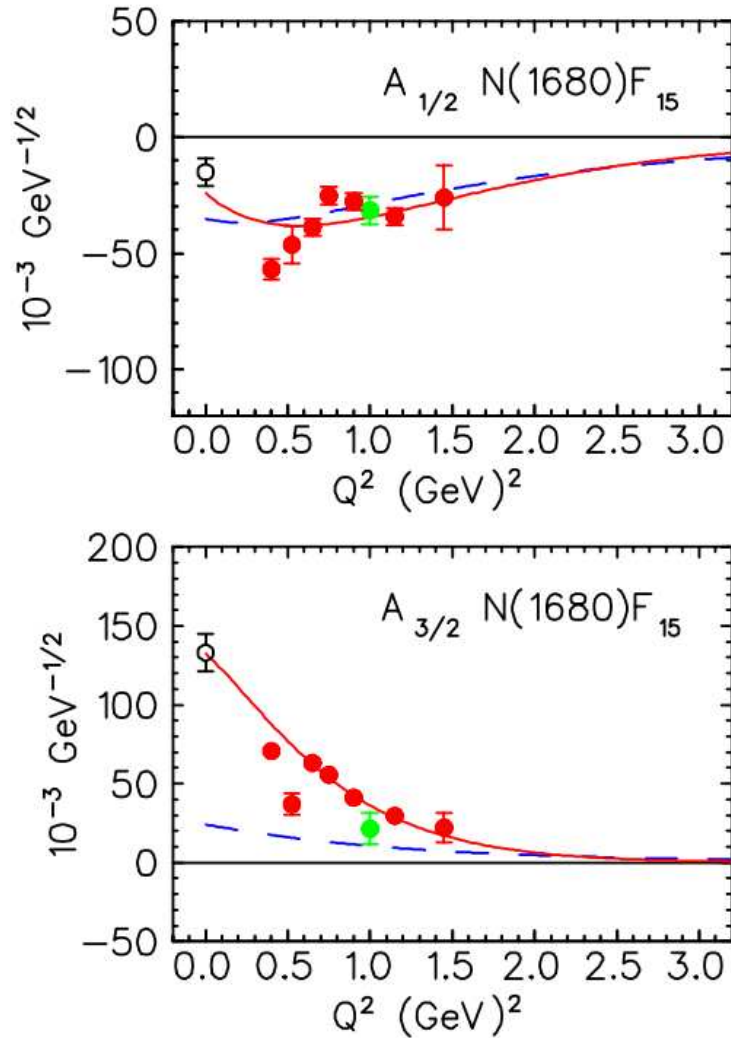


**Fig. 2.11:** The helicity amplitudes for the  $F_{15}(1680)$  [91]. The dots are MAID results from the data in Table 2.1. The solid and dashed curves are the results of the MAID superglobal fit and the predictions of the hyperspherical constituent quark model [92]. The dotted lines show the pion cloud contributions calculated with DMT [93]. The data points at finite  $Q^2$  are the results of the single- $Q^2$  fits. At  $Q^2 = 0$  the photon couplings from the PDG are shown [1].

MAMI results on the  $\pi^0$  electroproduction include the cross section at the  $Q^2 = 0.06, 0.127$  and  $0.2 \text{ GeV}^2$  and structure functions  $\sigma_L + \epsilon\sigma_L, \sigma_{LT}, \sigma_{TT}$ , and  $\sigma_{LT'}$  in the limited range of the polar angle [52, 53]. These data cover the low  $Q^2$  region.

MIT/Bates results are obtained in three experiments using out-of-plane scattering facility (OOPS). The  $ep \rightarrow ep\pi^0$  cross section at  $Q^2 = 0.127 \text{ GeV}^2$  was measured for several values of polar and azimuthal angles [54], [55], [56]. The choice of the azimuthal angle allows the separation of the structure functions  $\sigma_L + \epsilon\sigma_L, \sigma_{LT}$ , and  $\sigma_{TT}$ . Limited kinematical and angular coverage makes this data poorly suited to extraction of transitional amplitudes.

JLab/Hall A experiment [44] was performed using the polarized electron beam and a pair of high resolution magnetic spectrometers. It produced the cross section in the W region up to 2 GeV at the single  $Q^2$  value of  $1 \text{ GeV}^2$  and backward  $-1 < \cos\theta^* < -0.8$ . The structure functions  $\sigma_T + \epsilon\sigma_L, \sigma_{TT}$ , and  $\sigma_{LT}$  were extracted from the azimuthal angle fit. These data have the same limitation, as the MIT/BATES data above: single  $Q^2$  point does not allow to understand the evolution of  $N^*$ .

JLab/Hall C performed two measurements of  $ep \rightarrow ep\pi^0$  cross section in the region of the  $\Delta$  resonance at  $Q^2 = 2.8$  and  $Q^2 = 4.2 \text{ GeV}^2$  [50] and  $Q^2 = 6.4$  and  $Q^2 = 7.7 \text{ GeV}^2$  [51]. High  $Q^2$  and low W data covers region completely different from the one discussed in this work and will provide the complimentary

information for the next level analysis.

The CLAS detector at the Jefferson Lab is the first full acceptance apparatus designed for the investigation of the exclusive meson production in a wide kinematics regime with nearly  $4\pi$  angular acceptance. The cross section was measured in the  $\Delta$  resonance region in the wide range of the  $Q^2$ , in the second and in part of the third resonance region [48]. The advantages of the results presented in this analysis are broader kinematical coverage, extending up to  $W = 1.8$  GeV, along with the significantly higher statistics, allowing for more precise determination of the resonance parameters.

The CLAS measurement allowed the extraction of the helicity amplitudes of the Roper resonance  $P_{11}(1440)$  in the range of the  $Q^2 < 4.5$   $GeV^2$  mostly from the  $\pi^+$  and  $\pi^+\pi^-$  electroproduction data [41, 62, 63, 64]. The argument toward the nature of the Roper resonance as the first radial excitation of the three quark ground state can be tested by this data. It will provide the highly accurate information about the  $\pi^0$  channel which currently has a limited impact on the analysis.

The  $S_{11}(1535)$  resonance was studied in both the  $\pi^+$  and  $\eta$  electroproduction channels, though the results on the  $S_{1/2}$  amplitude are solely from the  $\pi^+$  channel. We can provide the important information on the the channel which has not been included in the analysis.

The helicity amplitudes for the  $D_{13}(1520)$  resonance are extracted from the

CLAS data on  $\pi^+$  and  $\pi^+\pi^-$  electroproduction [39]. All three amplitudes,  $A_{1/2}$ ,  $A_{3/2}$  and  $S_{1/2}$  are determined. The data presented will add another channel with completely different non-resonant mechanism in the  $Q^2$  region, where the models predictions disagree with the experimental results. The “helicity flip” region, described above, will also be covered by the presented data.

The  $F_{15}(1680)$  resonance, depicted in Fig. 2.11, have just a few points measured from both single and double pion measurements. The presented data have a very high statistical accuracy in the third resonance region, and will provide reliable results. The data on the  $S_{1/2}$  amplitude is limited to double pion electroproduction channel.

## Chapter 3

### Experimental setup

#### 3.1 CEBAF accelerator

The electron accelerator of the Jefferson Laboratory is based on superconducting RF cavities operating in a continuous wave mode. The schematics of the machine is shown in Fig. 3.1. Electrons are produced in the injector by directing a laser beam on the Gallium Arsenide (GaAs) photocathode. They are accelerated by the static electric field and then by RF field in injector and reach energy of 67 MeV before they are released to the North LinAc. Such energy allows them to be in phase with the electrons already in LinAc. Two parallel linear accelerators along with the 9 arcs are built in the race-track configuration, and boost the beam energy by maximum of 1.140 GeV per turn. Each LinAc contains twenty cryomodules, operating at the 2K (the liquid Helium to maintain this temperature is supplied by the Central Helium Liquifier not shown on the picture). Cryomodule consists of five niobium cavities that have gradient of the acceleration 10 MeV/meter. Arcs at the end of accelerators designed to bend electrons of different energies (number of

passes through accelerator) and recombine them for a new pass through a LinAc.

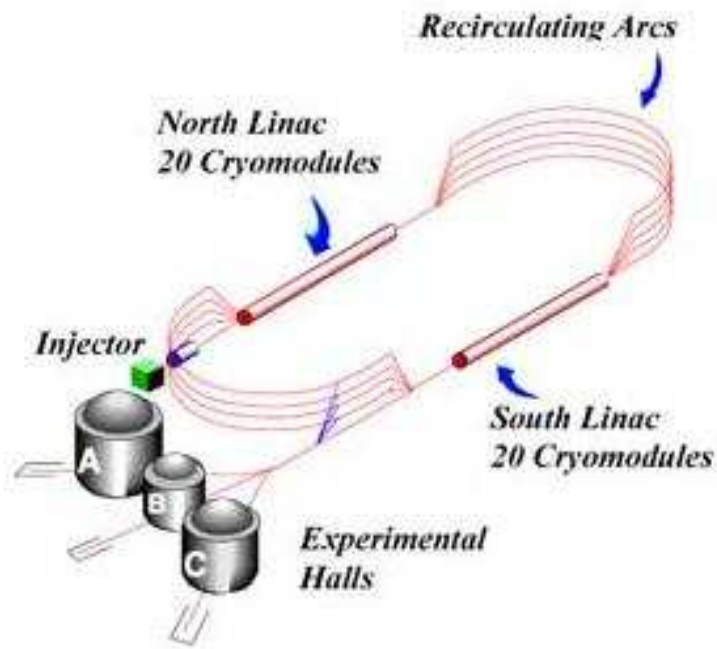


**Fig. 3.1:** CEBAF accelerator and three experimental Halls. Injector serves as a source of electrons.

The machine can deliver beam to each Hall at either the same energy or at the multiples of  $1/5$  of the maximum energy, since beam can be extracted at each pass. RF frequency of  $1.497\text{GHz}$  set the time profile for the beam, and experimental Halls receive bunches separated by  $2\text{ ns}$ .

### 3.2 CLAS detector

The experiment was carried out in the middle experimental Hall in the picture above. It houses CLAS (CEBAF Large Acceptance Spectrometer), the detector specifically designed for spectroscopic measurements. It consists of six identical independent detectors with the total azimuthal coverage almost  $4\pi$  with the polar coverage of  $8^\circ - 140^\circ$  for the charged particles and  $8^\circ - 45^\circ$  for neutrals.

Fig. 3.2 shows the schematic cross section of the detector. Charged particles are bent by a magnetic field generated by the toroidal magnet (yellow), which changes the azimuthal angle for the purpose of the momentum determination while leaving the polar angle intact.

In case of e1e setup each of the six sectors was composed by:

- Three regions of the drift chambers (shown in blue) covering the azimuthal angle  $[8^\circ - 140^\circ]$  to determine the trajectory of the charged particles in the magnetic field, and, therefore, the momentum (Eq. 3.1):

$$P = Bq\rho, \tag{3.1}$$

where  $B$  is the magnetic field,  $q$  is the particle charge,  $\rho$  is the radius of the curvature of the trajectory and  $P$  is the momentum we want to measure;

- Cerenkov counter (purple), covering  $[8^\circ - 45^\circ]$ , range separates electron from negative pions;

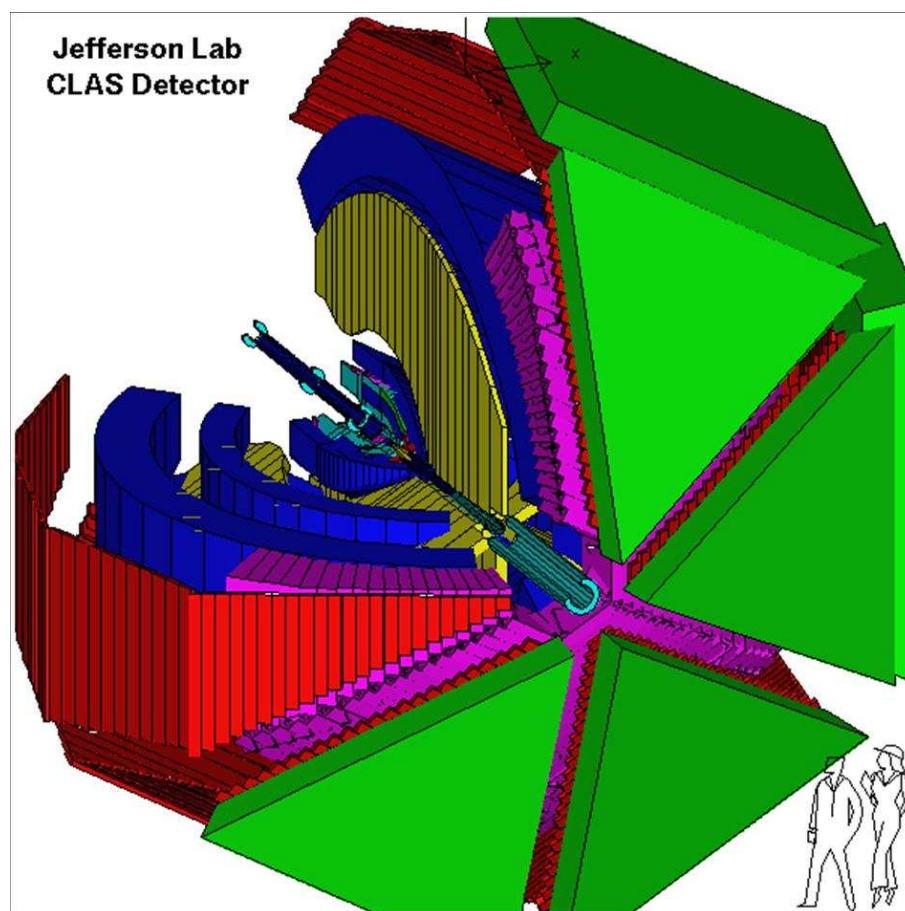


**Fig. 3.2:** Cross section of CLAS detector. Different subsystems shown in color and will be explained below.

- Time of flight system, represented by array of scintillators (red),  $[8^\circ - 140^\circ]$  in  $\theta$ , measures time it takes for a particle to travel from the point of interaction to the detector. We use it for proton -  $\pi^+$  separation;
- Electromagnetic calorimeter (green) with the angular range  $[8^\circ - 45^\circ]$  can identify both electrons and neutral particles (photons, neutrons);
- Minitorus magnet is used to deflect the Moller electron into the beam dump.

The Faraday cup, not shown in picture, is a metal cup, located 29 m downstream of the CLAS center, accumulates the beam charge and is used to determine the incident electron flux through the target. It is crucial part for the analysis yielding the absolute quantities, such as the reported one.

### 3.2.1 Torus magnet

The advantages of the toroidal magnet (Fig. 3.3) compared to others geometries - dipolar and solenoidal - are conservation of the polar angle, uniform momentum resolution over the broad momentum range and absence of the field in the wide region around the target, allowing to use a target with the own magnetic field and perform polarized target experiments.

On the other hand, the very structure of the magnet limits the  $\phi$  acceptance due to presence of coils.

The magnet used in CLAS is made of the 6 groups of the superconducting coils and is capable of producing the magnetic field of up to 2 Tesla at the

maximum coil current of 3680A.

### 3.2.2 Drift chambers

Drift chambers system [95] of the CLAS detector is designed to measure the momentum of the charged particle: the charged particle traveling through the gas ionizes it, and, in the presence of the electric field, creates positive and negative currents. Wires in drift chambers collect ions and distribution of currents represent the track of the particle. The momentum resolution depends on the position and density of wires inside the detector.

Drift chambers consist of three regions, with the first one being inside the magnet coils, where we have a low magnetic field, the second one between the coils and the third one outside of them.

Each region is organized in two superlayers, where the first (axial) superlayer has its wires along with the magnetic field lines and the other one (stereo) at the angle of  $6^\circ$ . Layers of positively biased sense layers and negatively biased field layers are forming hexagonal drift cells (Fig. 3.4). Each superlayer in R2 and R3 is six cells wide while Region One has four cells due to spacing constraints.

The drift chamber gas mixture (90% of argon and 10% of  $CO_2$ ) is chosen for the high drift velocity provided by the argon and the ability of carbon dioxide to protect the system against the ionization avalanches.

Track reconstruction is done in two stages. During step one (Hit Based

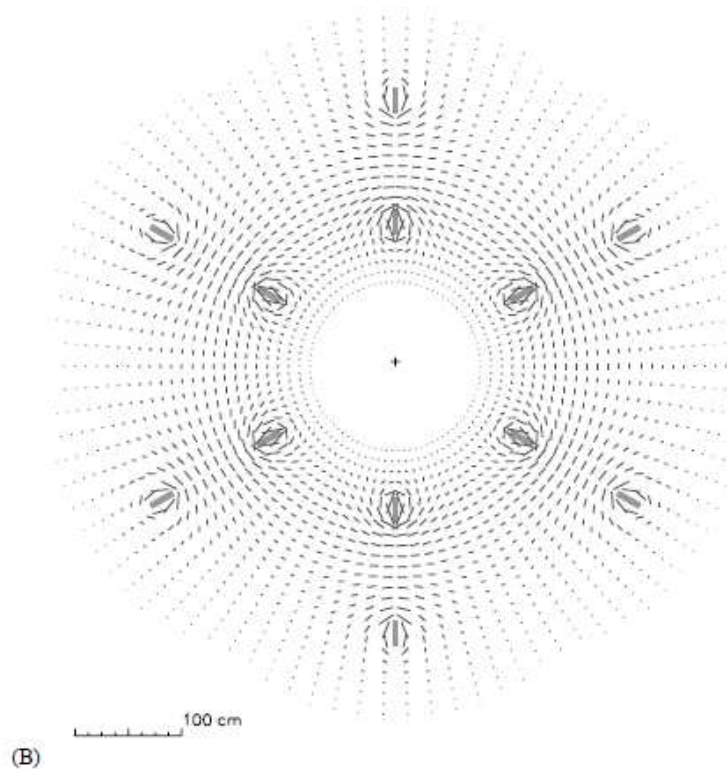
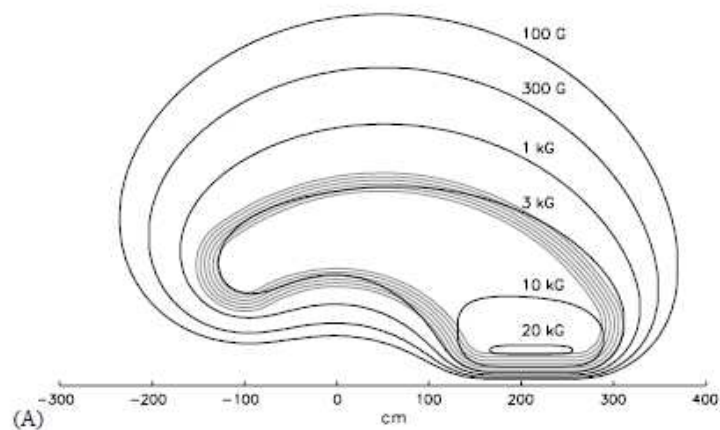


**Fig. 3.3:** (A) Contours of constant magnetic field for the magnet in the midplane between coils. Thin gray lines represent projection of the magnet coils; (B) Magnetic field map for the CLAS toroid transverse to the beam in the midplane of the target. The cross section of coils is shown.

Tracking) hits within the superlayer are recognized as belonging to the segment of the track (Fig. 3.4), with different track segments from different superlayers linked to form a track by comparison to reference table from the simulation.

In the second stage (Time Based Tracking) the drift time for each cell converted into the distance from the center of the cell. The trajectory, defined by these points, is then fitted (Fig. 3.4) and momentum of the particle is obtained from the fit.

The drift chambers were designed to provide the resolution of less the 0.5% for the momentum and 2 mrad for the  $\theta$  and  $\phi$ .

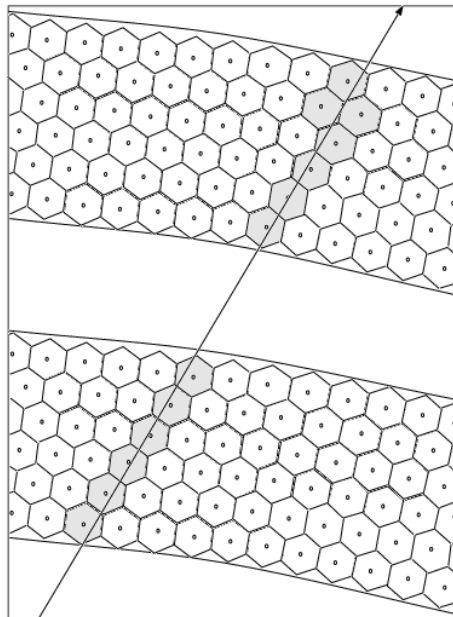


**Fig. 3.4:** Picture of the layer. The field wires form a hexagonal cell surrounding the sense wire. Particle traveling through the gas (solid line) will produce current in the nearby cells.

### 3.2.3 Cerenkov counter

When a charged particle traveling at speed close to that of light in vacuum enters the media, in which the light would travel at lower speed, it emits the radiation, called the Cerenkov radiation after the Russian scientist who first described it rigorously.

The electrons in our experiment even after interaction in the target have a energy of a few hundreds MeV (up to 1.8 GeV) and certainly produce a Cerenkov radiation (the threshold is 9 MeV). Negative pions, which can be misidentified for electrons, do not emit the radiation until they reach 2.5 GeV in momentum. Pion and electron thresholds are fixed by the choice of the gas inside the Cerenkov detector, perfluorbutane  $C_4F_{10}$ , with refraction index of 1.00153.

The CLAS Cerenkov detector [96] consists of six independent modules (Fig. 3.5), one for each sector, covering the azimuthal angle of up to  $45^\circ$ . Each of them contains 36 modules, 18 on the each side of the symmetry axis of the sector. Combination of elliptical and hyperbolic mirrors directs the emitted Cerenkov radiation into the PMTs, located in the shadow of the torus coils, so that the PMTs do not introduce additional holes in the geometrical acceptance of the detector. The centerline of the Cerenkov mirror, where the elliptical mirrors from different halves of the sector meet (Fig. 3.5), can slightly affect the efficiency of the electron registration.

### Optical Mirror System

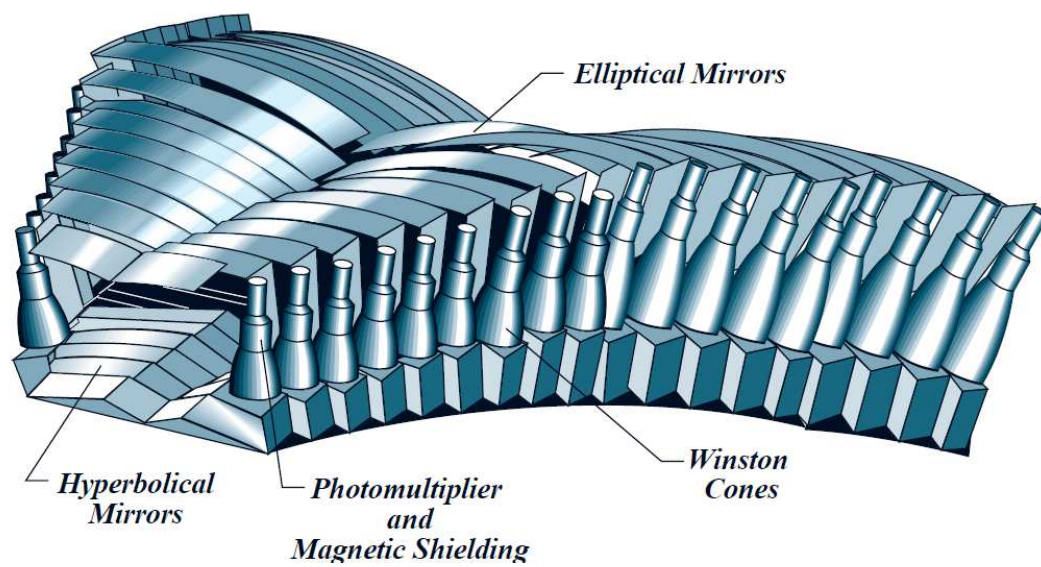


**Fig. 3.5:** Active gas volume is surrounded by elliptical and hyperbolic mirrors, directing particle radiation toward the Winston cones and photomultipliers.

### 3.2.4 Time of flight system

The information from the time of flight system (TOF) [97], along with the information about particle momentum from the DC, is used for the identification of the charged particles. TOF systems measure the time it takes a charged particle to reach from the target to the one of the scintillator bars.

The TOF detector schematics is shown in Fig. 3.6. Each sector consists of four panels, for a total of 57 Bicron-408 scintillators per sector, with the thickness of 5 cm and variation in length from 32 to 450 cm. Smaller bars are used at forward angles and longer covers backward direction. Charged particle passing through the scintillator produces ionization radiation which excites the media and in turn it emits photons. Some of them are internally reflected and reach the ends of scintillator bar, where they are collected into the light guides and then directed into PMTs.

Time resolution varies from 120 ps at the lower angle to 250 ps at the higher angle.

### 3.2.5 Electromagnetic calorimeter

The electromagnetic calorimeter [98] of the CLAS serves three main purposes:

- Electron and  $\pi^-$  discrimination, especially at higher momentum;
- $\pi^0$  and  $\eta$  reconstruction from  $2\gamma$  events;

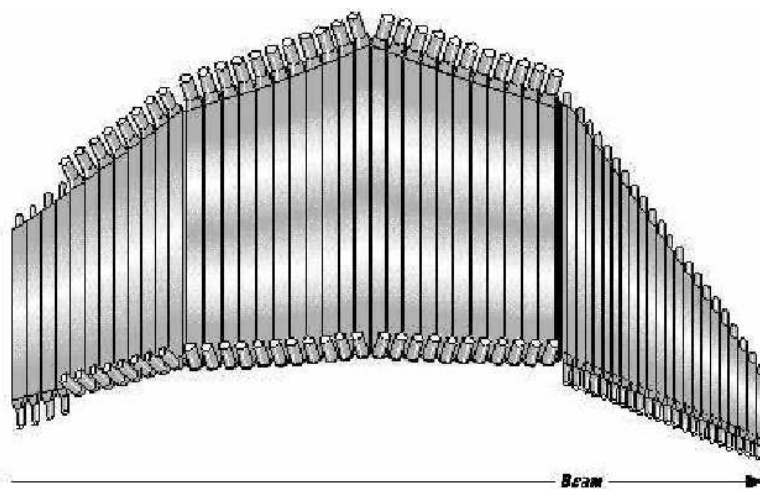


**Fig. 3.6:** One sector of the TOF counters. Scintillators at the forward direction (on the right) are shorter than at the higher angles. Each scintillator has two PMT to collect light.

- Neutron detection and identification.

Electrons have an easily distinguishable pattern of the interaction with the media - relativistic electron loses most of its energy via bremsstrahlung radiation proportionally to its momentum, while heavier particles emit constant amount of energy mostly via the process of the ionization.

Calorimeter covers the angular range from  $8^\circ$  to  $45^\circ$ . Each sector of the calorimeter is composed of 13 submodules, each consisting of the W, U and V scintillator and lead layer. The ratio of lead to the scintillating material (40 cm of scintillator and 8 cm of the lead per module) let the electron lose  $1/3$  of its energy in the scintillating material. The W, U and V layers (Fig. 3.7) are rotated

at the  $120^\circ$  with respect to each other, thus improving the spatial resolution of the calorimeter. Each of the 13 submodules is divided in the inner and outer stack (5 and 8 modules respectively) with the optical signal summed within a stack and sent to the PMT. Totally, for one sector number of PMTs used is equal to 216 (36 layers, 2 stack, 3 views - U, V, W).

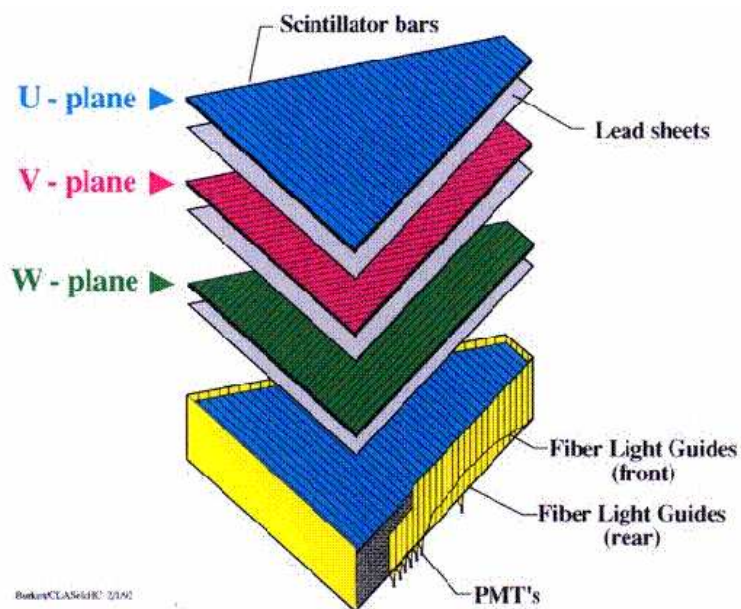


**Fig. 3.7:** Three scintillator layers (U, V, W) are rotated at  $120^\circ$  with respect to each other to improve the spatial resolution in the EC. Optical readout scheme is also shown.

### 3.3 Run conditions

The current experiment was performed with CLAS detector, the polarized electron beam of 2.039 GeV at nominal current 10 nA, and with the unpolarized liquid hydrogen target 2 cm long located in the center of the detector. We accumulated

about 1.5 billion triggers over a month of a beamtime.

The target is specific to our experiment and its setup is presented in Fig. 3.8. It has a conical shape with diameter varying from 0.6 to 0.4 cm. In some instances cooling system could not evacuate all the heat coming from the beam and hydrogen in target cell could boil. If bubbles would stay along beamline, real luminosity would be different from expected value and absolute measurement will lack accuracy. Conical shape helps to direct bubbles upwards and into wider area of the target, thus clearing the beamline. Forward aluminum window is made exactly the same as the entry/exit windows of target cell and can serve for both estimation of the number of events originated in the target windows and to precisely measure target Z position in the beamline.

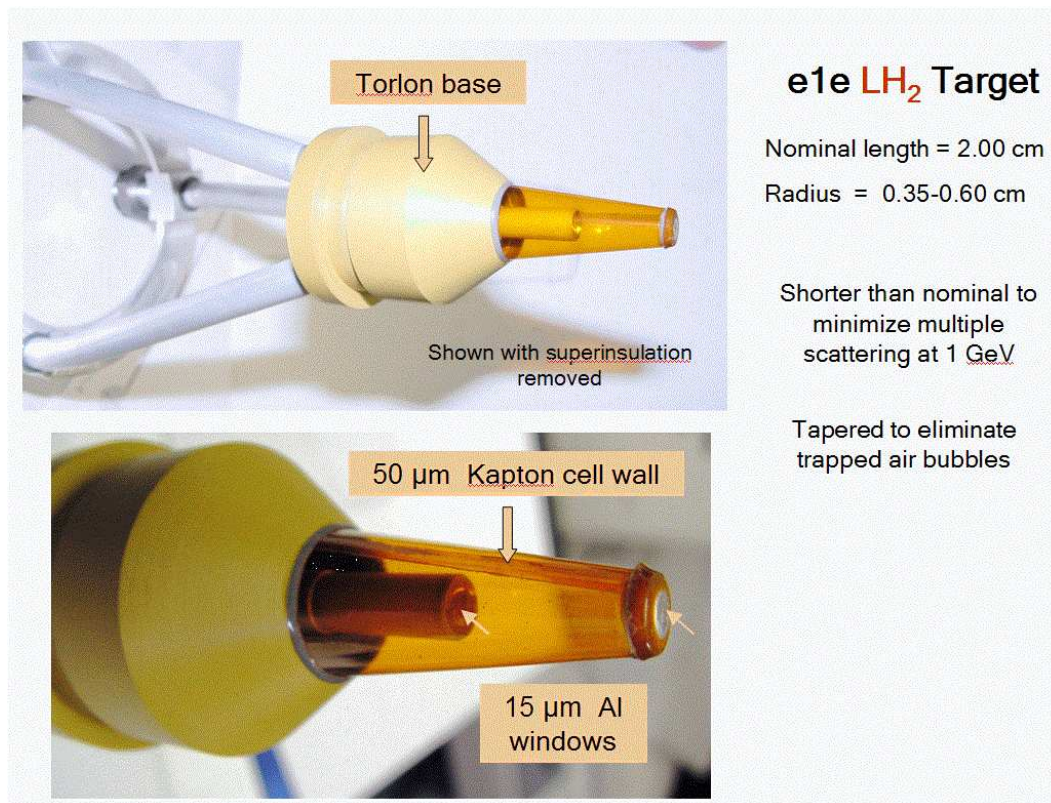


**Fig. 3.8:** Photograph of the target cell for e1e run. Above: target cell and support structure. Below: closeup of the target cell.

## Chapter 4

### Data analysis

#### 4.1 Data handling

During the experiment at Hall B at Jefferson Lab the raw data from the every subsystem of the CLAS detector is captured by the Data Acquisition System (DAQ) and stored in the BOS format. The original data files are processed, or “cooked”, with the reconstruction software (*recsis*) to extract information about the detector response in terms of the variables which characterizes tracks and events directly - particle momentum, tracks coordinates and timing information.

The processed data is stored in different formats including BOS banks (since the cooking process introduces the new variables, the structure of the reconstructed BOS files is different from the file with the raw data), PAW or ROOT ntuples or mu files. In this analysis the latter was used because of its small size, flexible structure and well developed interface to the files along with existing functions for the data manipulations.

## 4.2 Event selection

An event has to have at least one negative track to be considered as a candidate for the further analysis. Electron ID on such track is performed using the set of the cuts described below, and, if it satisfies them, we look for a positive track within the same event which latter may or may not be associated with the proton, depending on the cuts developed for the proton ID. The correction of the vertex position for both the electrons and protons helps select events originating within a target.

Momentum corrections are performed to account for possible drift chambers misalignments and particle energy loss within the detector.

CLAS simulation has some flaws in description of the border regions of the detector. There are also dead wires and inefficient PMTs which are not always accounted for in the simulation. Hence, for the charged particles we cut out these regions and select the areas with well-known acceptance by designing and applying the fiducial cuts.

For the events with electron and proton after all the corrections the  $\pi^0$  ID was performed based on the kinematical relationships between the charged particles.

Since  $\pi^0$  events can originate not only in the hydrogen filling the target, but also in entry/exit target windows, we use empty runs results to subtract such events.

Cut name	CLAS subsystem
U, V and W cuts	EC
Threshold	EC
$E_{in}$ vs $E_{out}$	EC
Sampling fraction	DC + EC

**Table 4.1:** Electron ID cuts and detector subsystem used for them.

Details of each procedures will be detailed below.

### 4.3 Particle ID

#### 4.3.1 Electron ID

Electron ID consists of the following four cuts which are applied to the negatively charged particle and use information from several subsystems of the detector (see Table 4.1). The purpose and details of each cut will be discussed below.

##### UV cut

Electron hitting the calorimeter is expected to deposit energy proportional to its momentum, but in case when electron hit the calorimeter near its edge there is a chance that the shower it produces will not be fully deposited in the calorimeter. To avoid it, border region of the calorimeter is cut out in each sector with the cut

presented in Eq. 4.1 and illustrated in Fig. 4.1.

$$U < 400cm,$$

$$U > 40cm,$$

$$V < 362cm,$$

$$W < 395cm. \tag{4.1}$$

There was a change in the condition of the calorimeter during the run number

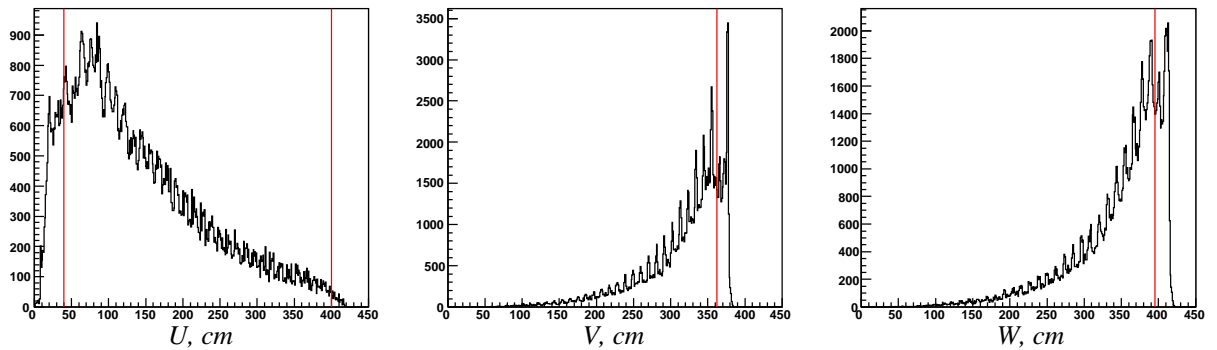


**Fig. 4.1:** U, V and W events distributions in calorimeter along with cut lines.

36430 which affected the data quality for all consecutive runs: the additional hole (Fig. 4.2) in third sector of the calorimeter, most likely connected to the failed photo tube or High Voltage board, has appeared. It is cut out for entire run period with the cut in Eq. 4.2:

$$V > 305cm,$$

$$V < 322cm. \tag{4.2}$$

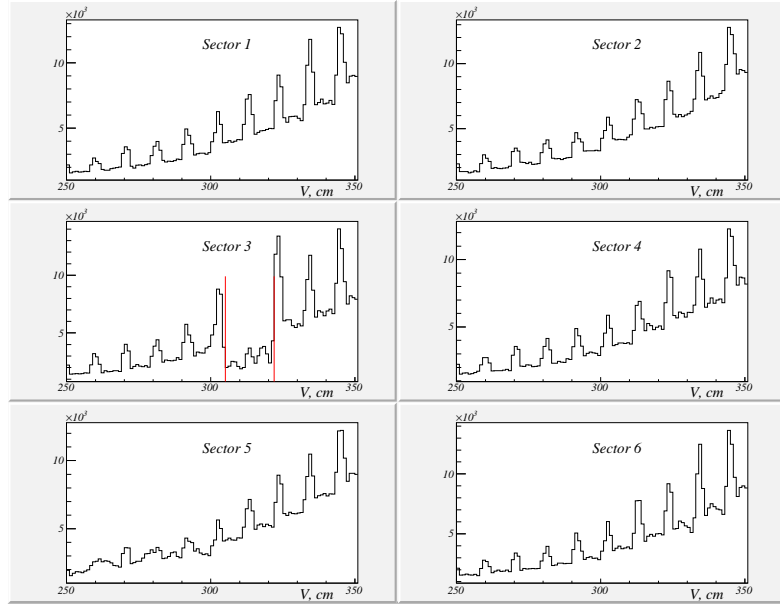


**Fig. 4.2:** Ineffective region of sector three is excluded from the further analysis.

### Minimum momentum cut

A study [101] of the inclusive cross-sections at different beam energies resulted in the minimum momentum cut, depending on the calorimeter low total threshold (in millivolts) (Eq. 4.3):

$$p_{min} = 214 + 2.47 * EC_{thr} MeV. \quad (4.3)$$

In case of discussed run  $EC_{thr} = 100$  mV and  $p_{min} = 461$  MeV. This cut is illustrated in Fig. 4.4.

### E inner versus E outer cut

This cut is based on the fact, that charged pions and electrons have different patterns of interaction with the media. While electrons deposit energy proportional to their momentum, pions lose a constant amount of energy per scintillator, about 2 MeV. Fig. 4.3 shows how the usage of this property helps us to clear up electron selection. The negative pions are concentrated at the lower values of the  $E_{in}$  and are eliminated with the  $E_{in} > 0.05 \text{ GeV}$

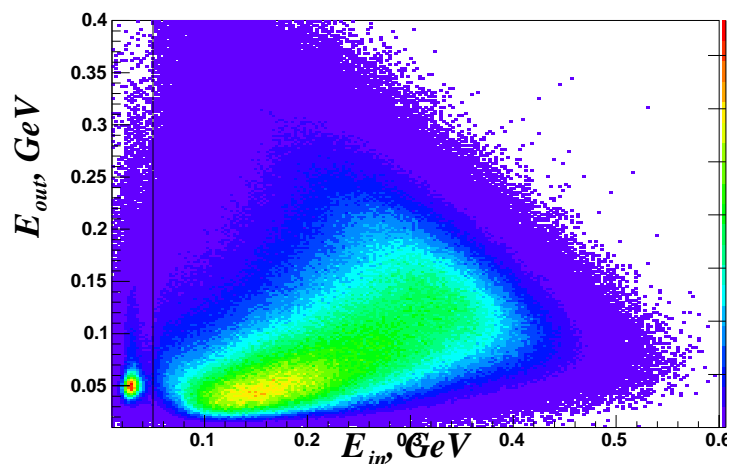


**Fig. 4.3:** Energy deposited in inner calorimeter versus energy in outer calorimeter. Events on the left of the black line are negative pions.

### Sampling fraction cut

The difference between radiation patterns of pion and electron, mentioned in the last paragraph helps us derive one more cut: distribution of total energy  $E_{tot}$ , deposited in calorimeter, versus momentum  $P$  for negative particles should follow

a straight line for electrons and  $1/x$  for pions. To perform  $e\text{-}\pi^-$  selection, all events are divided in bins along P axis, and each of them is fitted with Gaussian distribution. Then in each bin we select events which lie inside  $4\sigma$  from the center point (Eq. 4.4) and fit these  $4\sigma$  borders with second degree polynomial (plot and some more details can be found in Fig. 4.4). The CLAS calorimeter is a full deposition calorimeter which allows for the precise reconstruction of the electron momentum. The reason for the sampling fraction to be around  $1/3$  is that the  $2/3$  of the energy of the electrons is deposited in the lead, sandwiched between the inner and outer parts of the calorimeter.

$$\frac{E_{tot}}{P_{center}} - 4\sigma < \frac{E_{tot}}{P_e} < \frac{E_{tot}}{P_{center}} + 4\sigma. \quad (4.4)$$

### 4.3.2 Proton ID

The separation of the protons from other positively charge particles is based on the timing information from the TOF detector and the DC track length.

$$M = P\sqrt{\frac{T^2}{L^2} - 1} \quad (4.5)$$

If the particle mass is reconstructed by using this information (see Eq. 4.5) and is plotted as a function of the particle momentum for all positively charged particles (Fig. 4.5) we immediately notice the problem with the mass determination which leads to the appearance of different spurious structures, especially prominent in

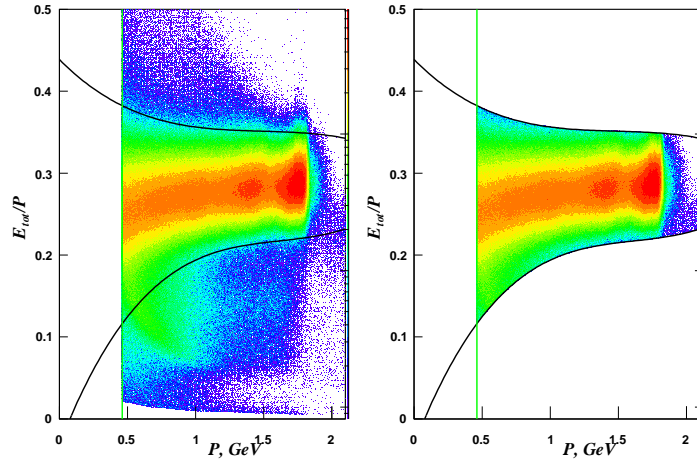


**Fig. 4.4:** Total energy, deposited in calorimeter, divided by momentum, versus momentum for negatively charged particles. The pions manifest themselves as  $\frac{1}{x}$  band on the left plot at lower values of momentum. Red solid lines is resulting sampling fraction cut position. Vertical green line is minimum momentum cut.

sector three. Careful analysis reveals, that the reason for this is the inefficient timing calibration for the run. It can be improved based on the known beam structure coming from the accelerator: each event has to originate from particular beam bunch separated by 2 ns interval. To do that, we loosely (TOF mass square  $> 0.3 \text{ GeV}^2$ ) select a proton and for these events calculate the time it would take a proton with momentum  $P$  to reach the TOF detector (calculations are performed for each of the 48 counters inside each sector) and subtract the measured time:

$$\Delta T = L\sqrt{M_p^2 + P_p^2}/P_p - T_{measured}. \quad (4.6)$$

Possible distributions of  $\Delta T$  versus momentum are presented in Fig. 4.6.

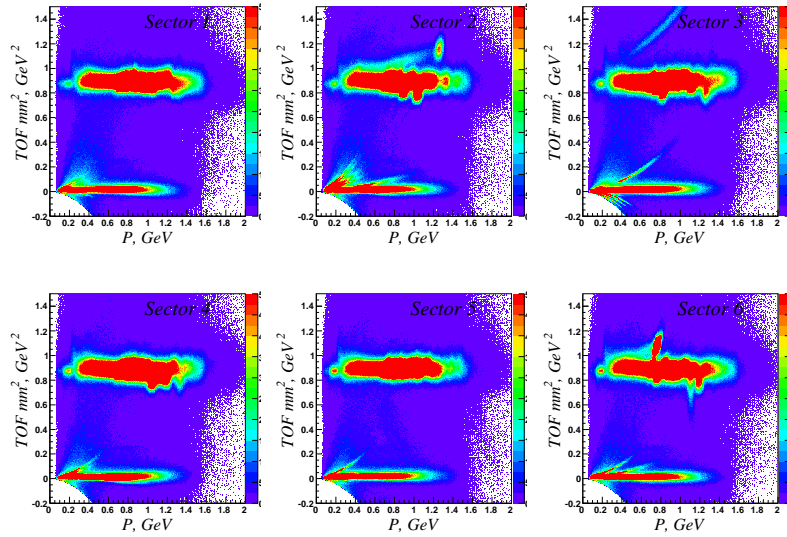


**Fig. 4.5:** TOF mass distribution versus momentum for different sectors. Note the erroneous structures especially prominent in the third sector.

First step of correction is to visually apply 2 ns correction to the paddles where we have type b) (Fig. 4.6) distribution. It means, that the beam bunch for this event was initially misidentified. Second, the  $\Delta T$  for each paddle was fitted with a Gaussian to determine smaller correction for the cases, when event was determined to originate in between the bunches. Overall effect of correction is presented in Fig. 4.7.

The proton identification procedure is based on the  $\Delta T$  used above. The whole momentum range is divided into bins and each individual distribution is fitted with a Gaussian. Then position of the  $\pm 4\sigma$  cut is determined in each bin and fitted as a function of the particle momentum (Fig. 4.8).

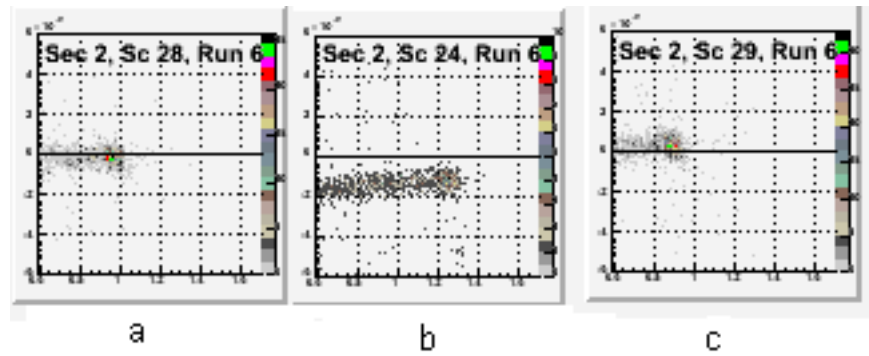


**Fig. 4.6:**  $\Delta T$  (Eq. 4.6) versus particle momentum for one scintillator. *a*) correct picture; *b*) 2 ns shift (wrong beam bunch); *c*) small shift (scintillator not calibrated to the bunch).

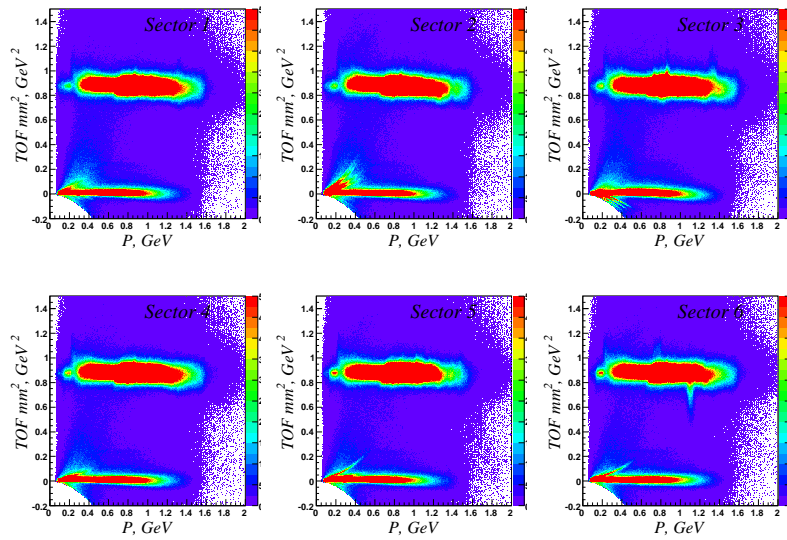


**Fig. 4.7:** TOF mass distribution versus momentum for different sectors. The major structures in Sectors 2 and 3 are eliminated

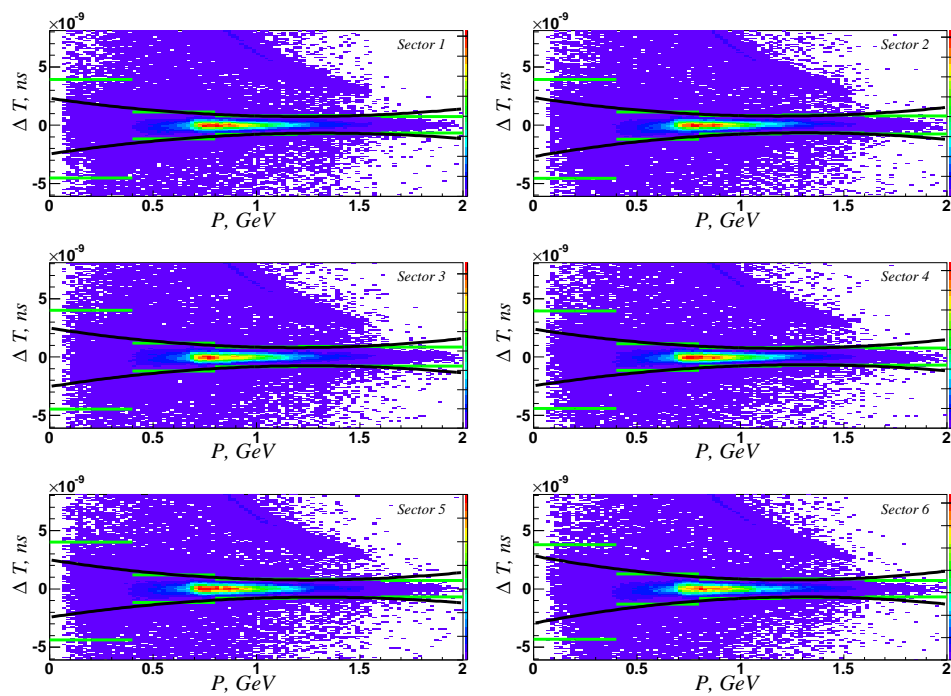


**Fig. 4.8:**  $\Delta T$  versus momentum distribution for positively charged particles along with the cut lines to select protons.

## 4.4 Vertex and momentum corrections

### 4.4.1 Vertex correction

For each track found, reconstruction software calculates  $(x, y, z)$  coordinates of the interaction point. Since the tracking code assumes, that all tracks are originated on the CLAS centerline, the shift of the beam position from the  $(0, 0)$  can lead to wrong determination of the coordinates (Fig. 4.9). Offset  $(x, y)$  has to be introduced.

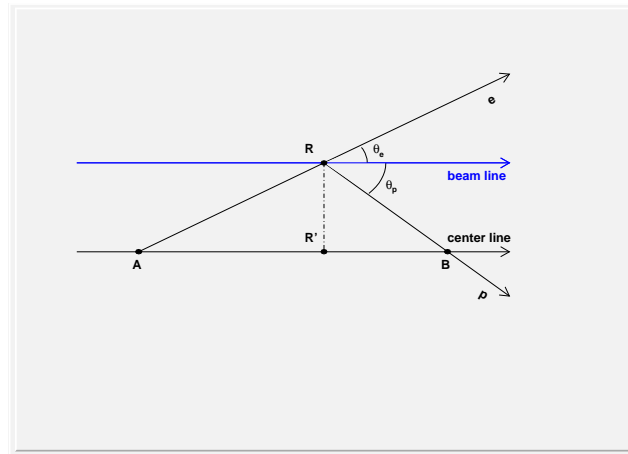


**Fig. 4.9:** Reason of incorrect vertex reconstruction: when beam line and CLAS center line do not coincide, event, occurred in  $R$ , will be projected on the centerline with electron  $Z$  coordinate  $A$  and  $Z$  proton coordinate  $B$ , while real position should be  $R'$ .

Possible way to perform it is to reconstruct the actual beam position using elastic events kinematics: for each event, we plot quantity  $\frac{Z_e - Z_p}{1/\tan\theta_e + 1/\tan\theta_p}$ , (where  $Z_e$  and  $Z_p$  are the  $Z$  position of the electron and proton vertex respectively, and

the  $\theta_e(\theta_p)$  is the polar angle of the electron (proton)) as a function of the azimuthal angle of the electron. Then distribution is fitted with  $a + b\sin(\phi + c)$ , where  $b$  and  $\phi$  are the distance and polar angle between the CLAS centerline and the beamline. The actual position of the center of the target is found as:  $z_{corr} = z - b(\sin\phi)/\tan(\theta_e)$ . Applying this offset in calculation on event by event basis leads to determination of correct position of  $Z$  coordinate of the vertex.

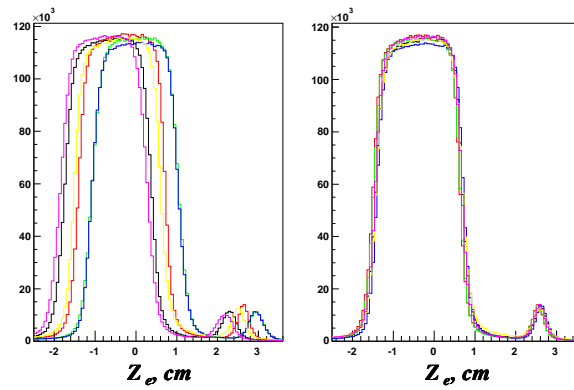


**Fig. 4.10:**  $Z$  coordinate of electron vertex before (left) and after (right) correction.

Different colors correspond to different sectors.

#### 4.4.2 Cut on the vertex position

While the most of the interactions occur within the target, some events can originate in the foil or, alternatively, there might be an error in tracking, and the event origination point can be reconstructed to be outside of the target. To exclude these events the cut  $-4 < Z < 2\text{cm}$  is applied on the  $Z$  coordinate of both proton and electron (illustrated in Fig. 4.11). The electron and proton coming

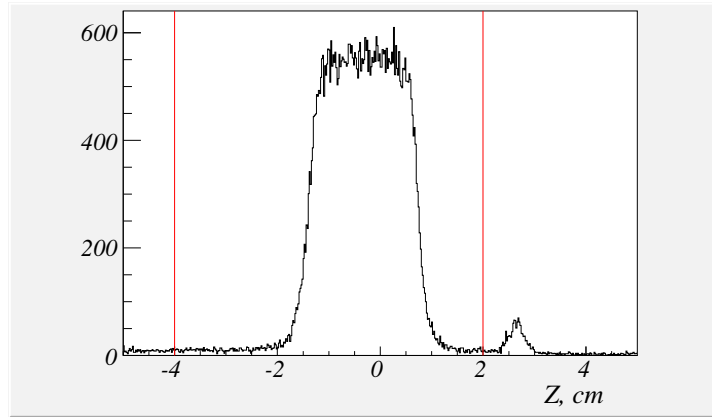


**Fig. 4.11:** Z coordinate of the electron vertex before the vertex cut along with the cut lines (red). The spike around  $Z = 3$  cm is the foil.

from the same event should originate from the same point in the target. The situation, in which the electron is coming from one event and the proton from another, or there is an error in the vertex position reconstruction, is excluded by the cut on the difference of the electron and proton vertex positions  $|Z_E - Z_P| < 4\text{cm}$  (Fig. 4.12).

#### 4.4.3 Proton energy loss

While traveling through the detector and the target, the proton loses part of its energy due to interaction with media and, hence, the measured momentum is different from the one the proton actually had right after the interaction. This effect is especially important for the low-energy protons, and can lead to misdetermination of the important kinematical quantities such as pion angular coordinates

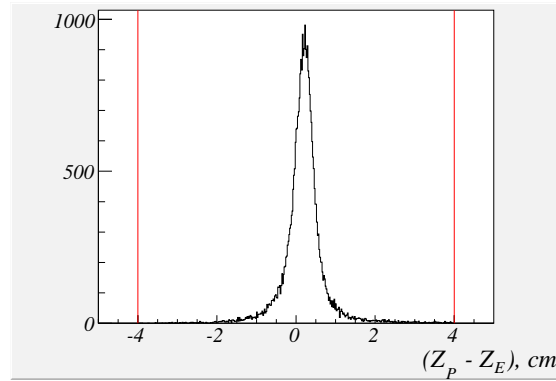


**Fig. 4.12:** Difference between the electron and proton  $Z$  in the target. The cut  $|\Delta Z| < 4 \text{ cm}$  is presented by red lines.

or momentum. GSIM simulation of the CLAS detector (more on it in the Chapter 5) correctly propagates proton through the media, and is used to account for this by using both information about the generated and reconstructed protons. The quantity  $\Delta P = \frac{P_{\text{generated}} - P_{\text{reconstructed}}}{P_{\text{reconstructed}}}$  as a function of the proton momentum is a good measure of proton energy loss and it emphasizes the importance of the correction at lower value of  $P$ .  $\Delta P$  is divided in bins over  $P$  and is fitted with the  $\frac{a}{bx+c}$  to determine  $a$ ,  $b$ , and  $c$ . Then this function is used to correct the momentum both in the simulation and the data. Results of the correction of simulation has a significant improvement at lower momentum of proton.

#### 4.4.4 Electron momentum correction

The need for the electron momentum correction arises mainly from drift chamber misalignment and an inaccurate magnetic field map. These inaccuracy are re-

sulted in slightly wrong determination of particle momentum, which then affects crucial quantities like  $W$  or missing mass. It is illustrated in Fig. 4.13, where  $W$  distribution for sector two is shown along with the theoretical peak position.

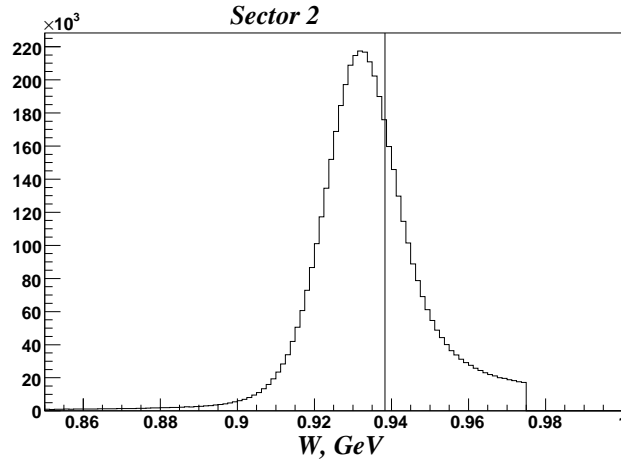


**Fig. 4.13:**  $W$  spectrum for elastic events. Black vertical line is true peak position at  $W = 938.3$  MeV.

One has quite limited choice of reaction available for the momentum correction, since constrained kinematics is needed in order to be able to reconstruct one quantity while trusting others. Typical examples include elastic and Bethe-Heitler processes. For the purpose of the correction, these two processes complement each other in a sense that elastic events provide huge statistics in the region of high electron momentum (low  $\theta_e$ ), and BH events provide wide coverage, spanning over all kinematical regions of  $\pi^0$  events. Figures 4.14 and 4.15 illustrate this thesis.

For the purpose of momentum correction it is important to divide BH events

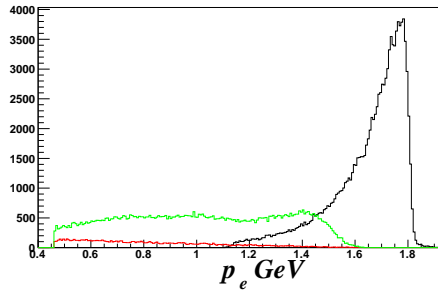


**Fig. 4.14:** Electron momentum coverage for elastic (black), BH(red) and  $\pi^0$  events (green).

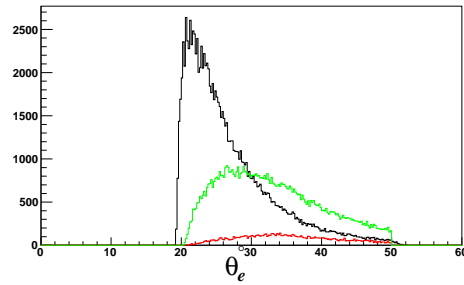


**Fig. 4.15:**  $\theta_e$  coverage for elastic (black), BH(red) and  $\pi^0$  events (green).

in pre- and post radiative (schematically shown in Fig. 4.16), since only former one can be used in correction procedure: the final momentum of the electron is the quantity we correct and it is correctly measured only for the postradiative events.

Several cuts used to identify processes of interest:  $0.775 \leq W \leq 0.975$  GeV used for elastic, while BH selection includes  $\phi_e - \phi_p$  cut, Fig. 4.17, and limitation on the angle of the missing particle  $\theta_x < 1^\circ$  cut, Fig. 4.18, to explicitly select pre-radiated process. The latter cut select events in which the photon was emitted along the direction of the incoming electron (beam).

The approach used in this analysis is two-fold: both  $ep \rightarrow ep'$  and  $ep \rightarrow ep'\gamma$  reactions were taken into account with binning for the BH process shown in the Table 4.2. For each event, theoretical electron momentum was reconstructed, using initial beam energy and final electron angle (Eq. 4.7 used for the elastic

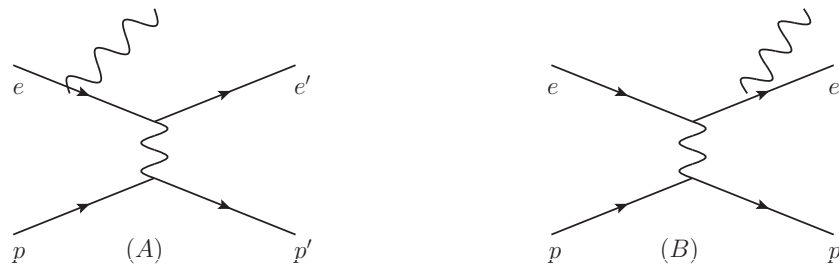


**Fig. 4.16:** Preradiative (A) and postradiative (B) BH processes. Electron momentum after interaction can be measured in the first case.

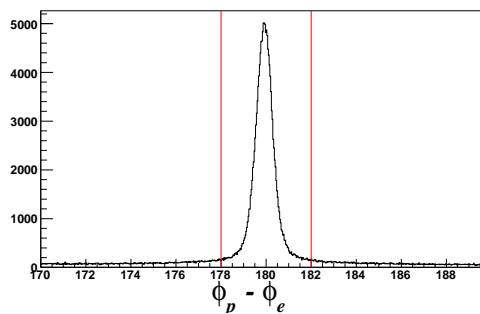


**Fig. 4.17:** BH events selection using  $\phi_p - \phi_e$  cut. Events between red lines selected as a candidate BH events.

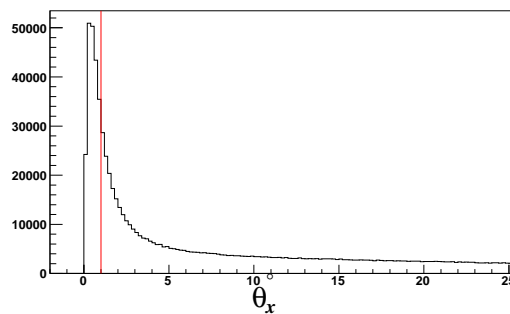


**Fig. 4.18:** BH events selection using  $\theta_x$  cut. Events on the left of red line selected as a candidate BH events.

Variable	Bin size	Number of bins	Low border	High border
$\theta_e$	$5^\circ$	6	$20^\circ$	$50^\circ$
W	100 MeV	9	1100 MeV	2000 MeV
$\phi_e$	$1^\circ$	60	$-30^\circ$	$30^\circ$

**Table 4.2:** Angular, momentum and invariant mass bins for electron momentum correction with BH events.

events, while Eq. 4.8 used for the BH):

$$P_{elas} = \frac{P}{1 + \frac{P(1-\cos\theta_e)}{M_p}}, \quad (4.7)$$

$$P' = \frac{M_p}{1 - \cos\theta_e} \left( \cos\theta_e + \frac{\cos\theta_p \sin\theta_e}{\sin\theta_p - 1} \right)$$

$$P_{eBH} = \frac{P'}{1 + \frac{P'(1-\cos\theta_e)}{M_p}}, \quad (4.8)$$

$$f(x) = a + b\phi_e + c\phi_e^2. \quad (4.9)$$

Elastic part of the correction is treated as an additional W bin with center at 0.938 GeV. Difference between measured and theoretical momentum was fitted with Gaussian in each W -  $\theta_e$  -  $\phi_e$  bin and plotted as a function of  $\phi_e$ . Then obtained distribution was fitted with 2<sup>nd</sup> order polynomial (Eq. 4.9) as a function of  $\phi_e$  (Fig. 4.20 shows the distribution for elastic events and Fig. 4.19 for BH

events).

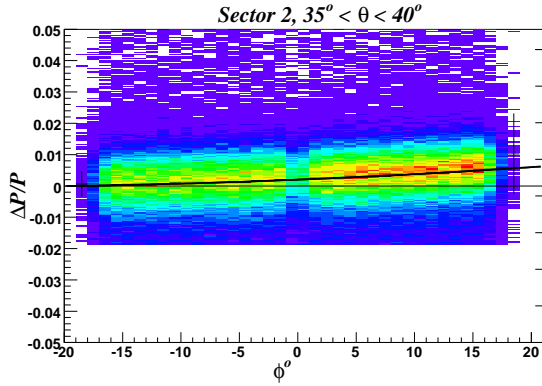


**Fig. 4.19:**  $\frac{\Delta P_e}{P_e}$  for elastic events before correction with fit with 2<sup>nd</sup> order polynomial (solid black line).

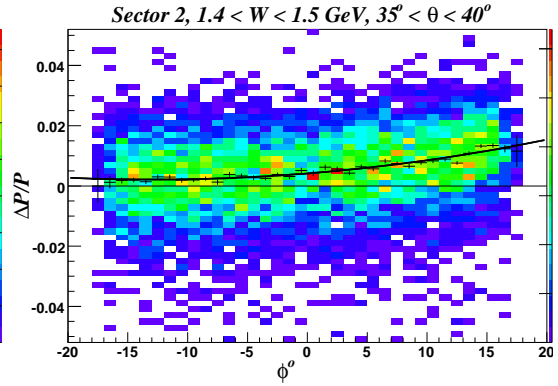


**Fig. 4.20:**  $\frac{\Delta P_e}{P_e}$  for elastic events before correction with fit with 2<sup>nd</sup> order polynomial (solid black line).

Finally, we linearly interpolate fit coefficients  $a$ ,  $b$  and  $c$  as a function of  $W$  (Fig. 4.21).

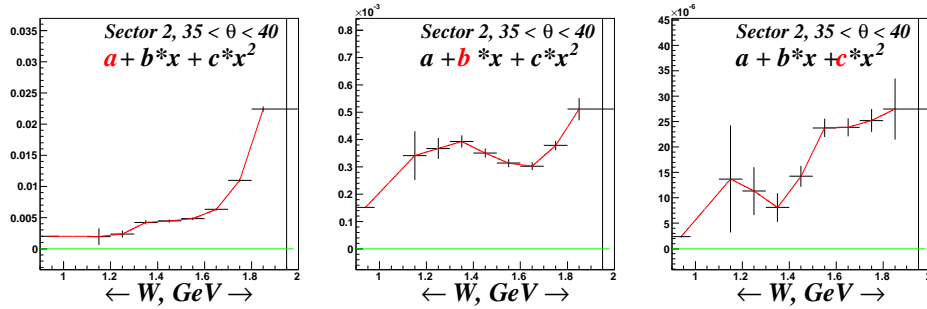


**Fig. 4.21:** Linear interpolation of  $a$ ,  $b$  and  $c$  (Eq. 4.9) as a function of  $W$ .

Corrected results are presented in terms of:

- $\frac{\Delta P_e}{P_e}$  as function of  $\phi_e$  for elastic and BH events (Fig. 4.22 and Fig. 4.23);

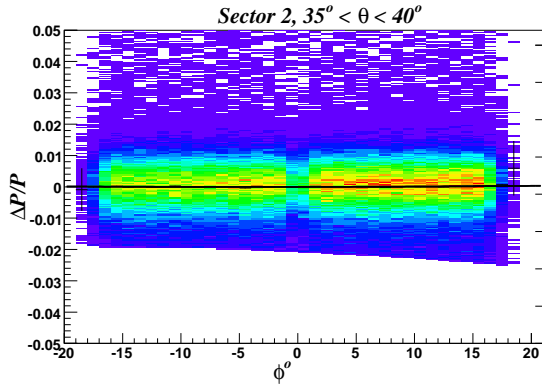


**Fig. 4.22:**  $\frac{\Delta P_e}{P_e}$  for elastic events along with  $2^{nd}$  order fit after correction.

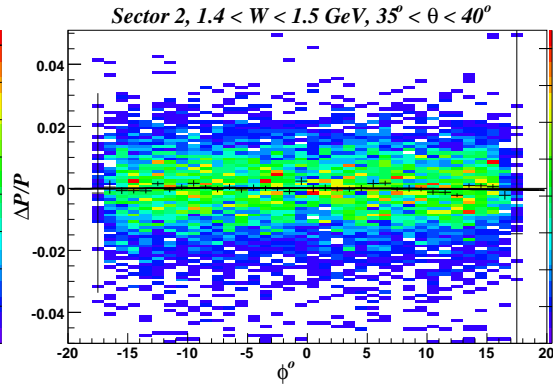


**Fig. 4.23:**  $\frac{\Delta P_e}{P_e}$  for BH events along with  $2^{nd}$  order fit after correction.

- W spectrum for elastic events and  $M_x^2$  spectrum for Bethe-Heitler events before and after correction (Fig. 4.24 and Fig. 4.25);

We summarize the correction by plotting peak position (Fig. 4.26 and Fig. 4.28) and width (Fig. 4.27 and Fig. 4.29) for elastic and BH channels as a function of sector number. A significant improvement in both elastic peak position and width as well as in missing mass distribution for the Bethe-Heitler events is achieved. It is important for the calculations of the  $\pi^0$  kinematical quantities.

#### 4.4.5 Proton momentum correction

After electron momentum correction, described in the previous chapter, we have elastic W spectrum and missing mass of the BH process at the correct position. The pion peak position is shown in the Table 4.4. From these numbers it is

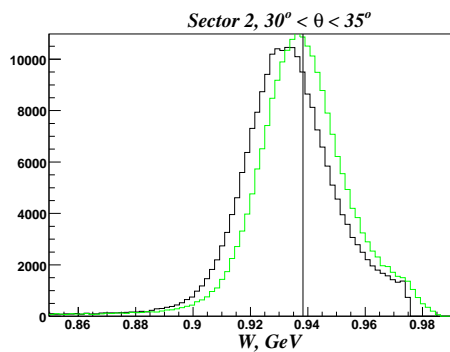


**Fig. 4.24:**  $W$  distribution before (black) and after (green) correction. Vertical black line is at the proton mass (938.3 MeV).

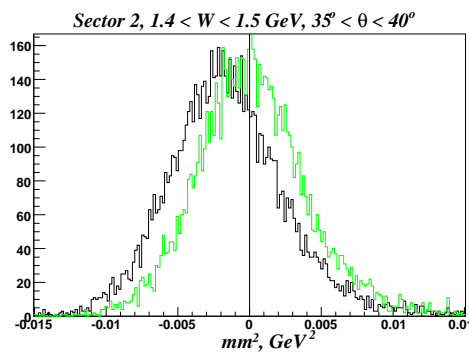


**Fig. 4.25:**  $M_x^2$  distribution before (black) and after (green) correction. Vertical black line shown at zero.

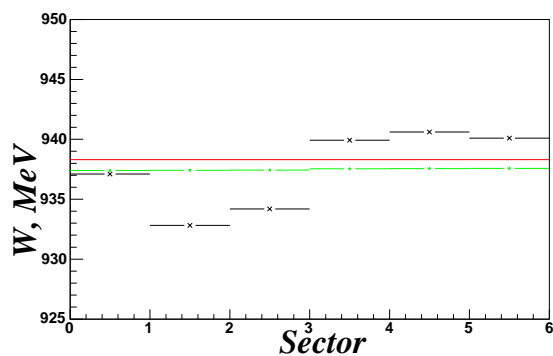


**Fig. 4.26:**  $W$  peak position as a function of sector before (black) and after (green) correction. Horizontal red line is at the nominal value of 939.3 MeV.

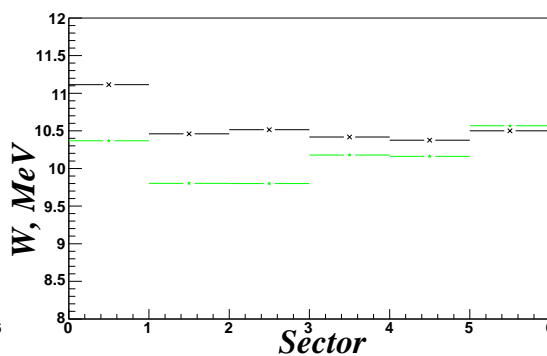


**Fig. 4.27:** Width of  $W$  peak as a function of sector before (black) and after (green) correction.

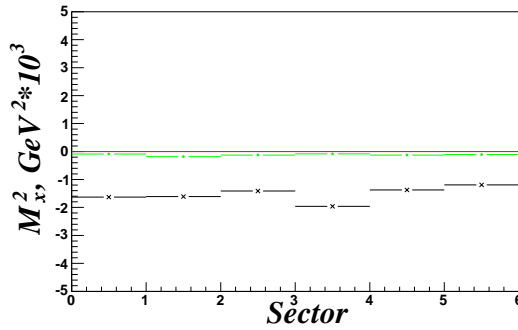


**Fig. 4.28:**  $M_x^2$  peak position as a function of sector before (black) and after (green) correction. Horizontal red line is at zero, nominal position of the missing mass peak.

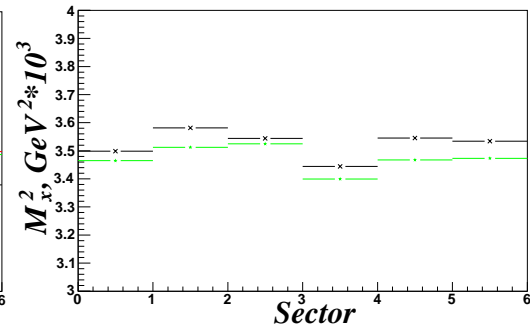


**Fig. 4.29:** Width of missing mass peak as a function of sector before (black) and after (green) correction.

hard to conclude if it necessary to correct the proton momentum, but if one reconstruct it using the restricted kinematics of the  $ep \rightarrow ep'\pi^0$  reaction and plot  $\frac{P_{measured} - P_{calculated}}{P_{measured}}$  as a function of the proton  $\phi$ , it is clear that for some bins deviation can reach up to 2% (Fig. 4.31).  $ep \rightarrow ep'\pi^0$  reaction kinematics allows for reconstruction of the value of proton momentum using electron angles and momentum and proton angles and will be used to perform a correction.

For the purpose of the momentum correction the regular  $\pi^0$  identification procedure (Chapter 4.6) will be aided by the set of cuts to have a very strict events selection. The events after the ID are divided in the proton momentum and  $\theta$  bins independently for all six sectors and cut ( $peak - \sigma \leq M_x^2 \leq peak + 0.8 * \sigma$ ) is developed in each bin independently (Fig. 4.30). Then the position of the cut is

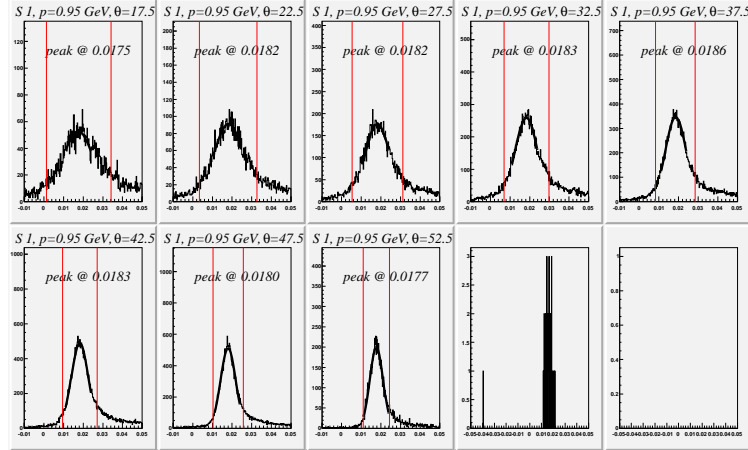


**Fig. 4.30:**  $\pi^0 M_x^2$  distribution for sector 1 along with the proposed cuts.

fitted as a function of the proton  $\theta$  and we apply it to strictly select  $\pi^0$  events.

After the event selection, momentum correction procedure is very similar to the one used for the electron side, with only noteworthy difference arising from the fact, that  $\frac{\Delta P}{P}$  distribution in individual 4-differential bins can not be fitted correctly with pure Gaussian, hence Gaussian plus second order polynomial is used. Binning used for the correction is shown in the Table 4.3. Fig. 4.31 and Fig. 4.32 show the procedure and its result, respectively, in terms of the  $\frac{\Delta P}{P}$  versus  $\phi_p$ .

The final peak position and width in different sectors are presented in the Table 4.4. On the average, there is an improvement in the peak position, and the width of the peak is reduced in every sector. The plots of the  $\frac{\Delta P}{P}$  after corrections (Fig. 4.32) are important as well since they show how the correction works for the value of the proton momentum itself.

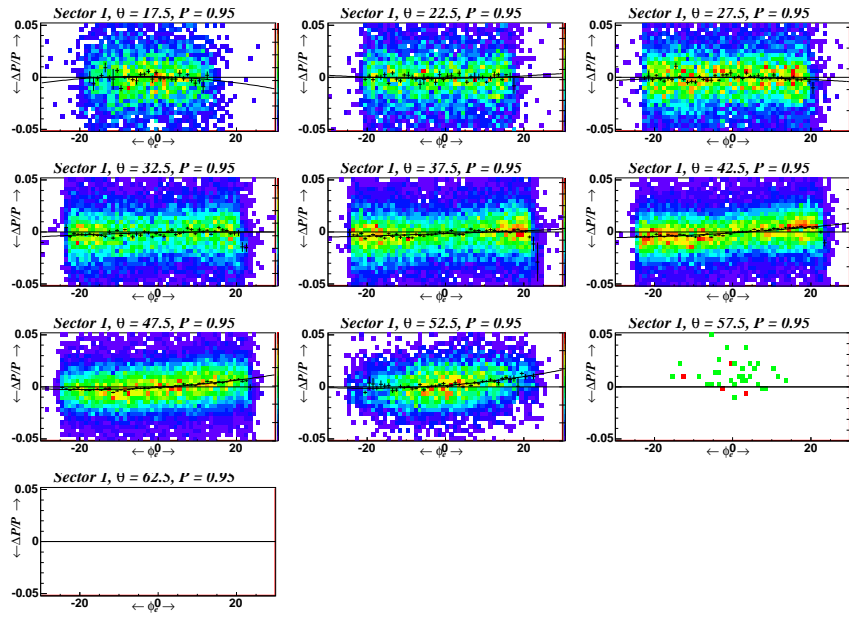


Fig. 4.31:  $\frac{\Delta P}{P}$  as a function of  $\phi$  of the proton before correction.

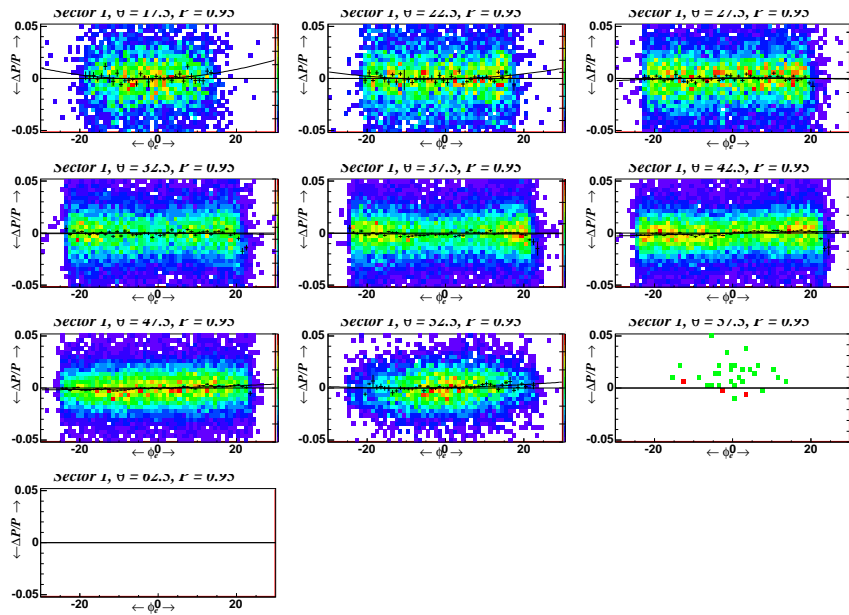


Fig. 4.32:  $\frac{\Delta P}{P}$  as a function of  $\phi$  of the proton after correction.

Variable	Bin size	Number of bins	Low border	High border
$\theta_p$	$5^\circ$	10	$20^\circ$	$70^\circ$
$P_p$	300 MeV	5	200 MeV	1700 MeV
$\phi_p$	$1^\circ$	60	$-30^\circ$	$30^\circ$

**Table 4.3:** Angular and momentum binning for proton momentum correction.

Sector	1	2	3	4	5	6
Peak, before( $GeV^2$ )	0.0181	0.0181	0.0173	0.0174	0.0174	0.0173
Peak, after( $GeV^2$ )	0.018	0.081	0.0177	0.0175	0.0176	0.0176
$\sigma$ , before ( $GeV^2$ )	0.0046	0.0047	0.0049	0.0047	0.0049	0.0048
$\sigma$ , after( $GeV^2$ )	0.0045	0.0046	0.0047	0.0046	0.0048	0.0047

**Table 4.4:** Momentum correction results. Both pion missing mass position and width show improvement.

## 4.5 Fiducial cuts

### 4.5.1 Electron fiducial cut

CLAS detector does not have uniform acceptance in all phase space due to different properties of its subsystems. The Cerenkov counter, for example, has a drop in optical efficiency which is not reconstructed in Monte-Carlo simulation. Drift chambers and time of flight inefficiencies (dead wires or photo tubes) can cause drops or holes. Some of them are reproduced in Monte Carlo simulation, while others are not, and the purpose of the fiducial cut is to select regions of phase space with maximum and stable efficiency and where it is reproduced in simulation.

#### $\theta_e$ and $\phi_e$ cut

The inefficiencies are sector dependent and are not necessarily symmetric within the sector. Boundaries in  $\phi_e$  are selected empirically such that the distribution of events inside them is flat (Fig. 4.34). Studies [102] show, that analytical shape of such cut can be expressed as in Eq. 4.10, where we have 5 different parameters  $C_i$  adjusted for each sector and explicit momentum dependence. The results of fiducial cut implementation are shown in Fig. 4.33:

$$\begin{aligned}
 \theta_{cut} &= C_1 + \frac{C_2}{p+C_6}, \\
 E &= C_3 p^{C_5}, \\
 \Delta\phi &= C_4 \sin(\theta - \theta_{cut}).
 \end{aligned}
 \tag{4.10}$$

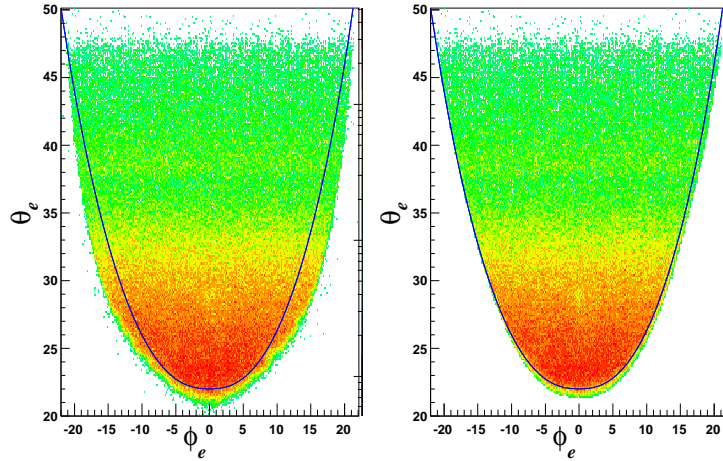


**Fig. 4.33:**  $\theta_e$  vs  $\phi_e$  distribution of electrons in sector 1 with  $1.2 \leq p \leq 1.4$  GeV before (left) and after fiducial cut. Blue line shows cut position.

#### 4.5.2 Proton fiducial cuts

##### $\theta - \phi$ cut

The reason to perform the proton fiducial cut is very similar to one that motivated us to do electron cuts - we do not fully understand the depletions of detector efficiency in some regions (border of sectors, for example), and, hence, can not incorporate these effects in simulation. The solution is to cut out those regions in data and then apply the same cuts in simulation.

The geometrically limited electron acceptance at low  $\theta_e$  (Fig. 4.33) has the following effect on the  $\theta - \phi$  distribution of the protons (Fig. 4.35, left panel). Prominent peak at  $\theta$  around  $50 - 60^\circ$  and  $\phi$  around  $0^\circ$  is the reflection of the

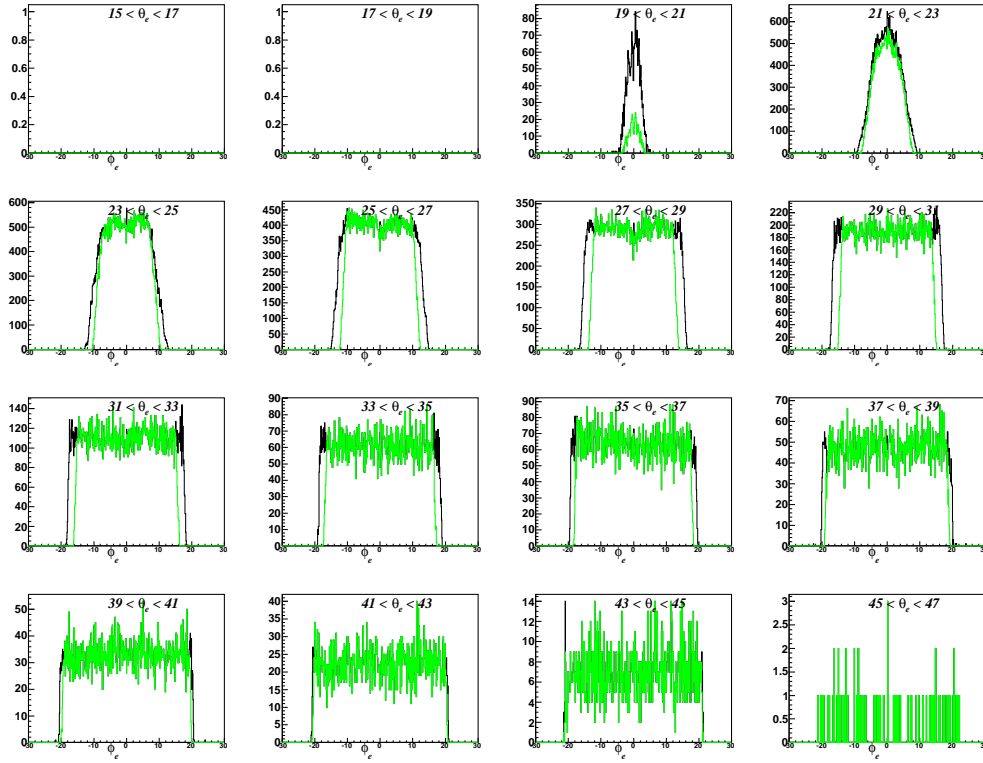


**Fig. 4.34:**  $\phi_e$  distribution of electrons in sector 1 with  $1.2 \leq P \leq 1.4$  GeV before (black) and after (green) fiducial cut. Note that shoulders found in original data absent after the cut.

low- $\theta$  elastic electrons. It alters the picture of the proton angular distributions and to be removed by the cuts on the  $(\phi_e - \phi_p)$  and  $W$  (Eq. 4.11) with results shown in Fig. 4.35, right panel.

$$|\phi_e - \phi_p| > 182^\circ \text{ or}$$

$$|\phi_e - \phi_p| < 178^\circ \text{ and}$$

$$W > 1.1 \text{ GeV}. \quad (4.11)$$

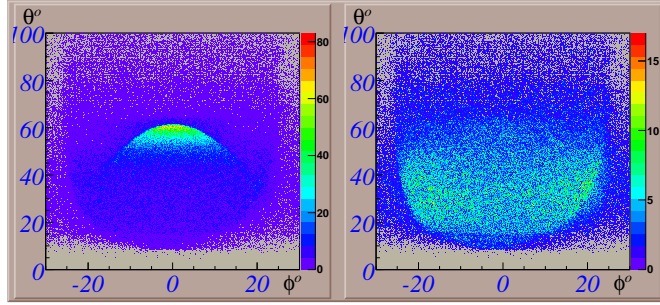


**Fig. 4.35:** Proton  $\theta - \phi$  distribution before (left) and after (right) elastic events subtraction.

With the cleaned sample, all events are divided in  $\theta_p$  and  $p_p$  bins, with  $\theta_p$  divided in 27 bins from  $6^\circ$  to  $60^\circ$  and variable binning in the proton momentum with first bin  $[0, 0.4)$  GeV, and then 7 bins 0.2 GeV width each up to 1.8 GeV. In each bin we select regions with uniform events distributions by adjusting parameters of fiducial cut (same formula as for the electrons). With parameters at hand, resulting cuts are applied on the protons(Fig. 4.36).

### **P - $\theta$ cut**

The holes found in the  $P_p - \theta_p$  distributions in Fig. 4.37 are not reproduced in the simulation, so these regions are cut out for both. The cut shape (Eq. 4.12):

$$a_1 - b_1(c_1 - P)^2 < \theta < a_2 - b_2(c_2 - P)^2 \quad (4.12)$$

is found empirically and properly describes the observed depletions.

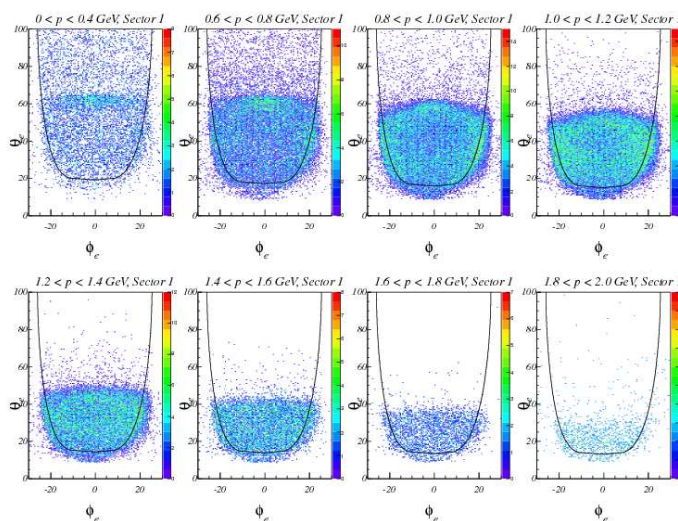


**Fig. 4.36:** Proton  $\theta - \phi$  distribution in momentum bins with proposed cut lines.

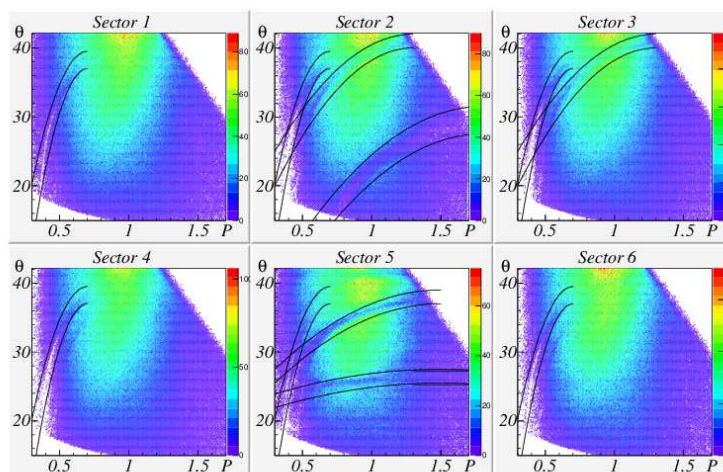


**Fig. 4.37:**  $\theta - P$  events distribution for the data. There are two prominent holes in the sector 2 and 5 and few smaller ones. Black lines illustrate the cuts. Exactly same cuts will be applied to the simulation.

#### 4.6 Bethe-Heitler processes

On the plot of the square of the  $ep \rightarrow epX$  missing mass ( $M_x^2$ ) versus  $W$  (Fig. 4.38) for the e1e run period after charged particle ID, vertex and fiducial cuts one can see two distinctive region, with BH events mostly concentrated at lower missing mass and  $\pi^0$  around  $0.02 \text{ GeV}^2$ .

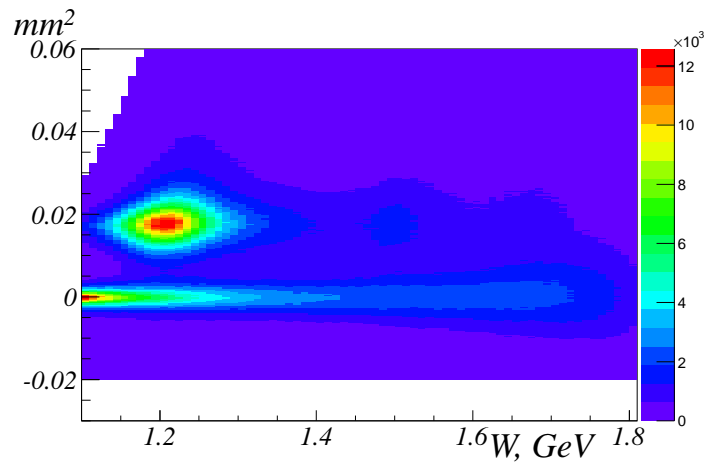


**Fig. 4.38:**  $W$  versus  $M_x^2$  for all events. Structure around  $0.02 \text{ GeV}^2$  shows pions.

Although CLAS detector is capable of neutral pion identification via detecting of products of its decay in two gamma quanta (it is predominant mode accountable for almost 99% of all pion decays), the need to detect two additional neutral particles would significantly drop our statistics. Instead, if one is able to directly measure two particles out of three, then momentum conservation will provide him all the constrains to identify missing particle.

We need to design a set of cuts to identify a  $\pi^0$  using momentum conservation

and available complete information on proton and electron.

Here one important assumption, called peaking approximation, will be used to reconstruct the proton angles from the reaction kinematics: the direction of emitted photon coincide with the direction of the incident electron. To perform  $\pi^0$  separation, we use the following variables:

- $\phi_{\pi^0}^*$ : center of mass azimuthal angle of the pion;
- $\Delta\theta_1 = \theta_{meas}^p - \theta_1$ :  $\theta_{meas}^p$  is measured polar angle of proton in the CLAS frame and  $\theta_1$  is proton angle reconstructed from outgoing electron energy and angle (Eq. 4.13);
- $\Delta\theta_2 = \theta_{meas}^p - \theta_2$ :  $\theta_2$  is the proton angle calculated from the incoming electron energy and outgoing electron angle (Eq. 4.14).

$$\tan\theta_1 = \frac{1}{\left(1 + \frac{E}{M_p}\right)\tan\frac{\theta_{e'}}{2}}. \quad (4.13)$$

$$\tan\theta_2 = \frac{1}{\left(1 + \frac{E'}{M_p - E' + E'\cos\theta_{e'}}\right)\tan\frac{\theta_{e'}}{2}}. \quad (4.14)$$

Since contamination is W- and  $\cos\theta_{\pi^0}^*$  dependent, all events are divided in 28 bins over W (from 1.1 to 1.8 GeV), each bin 25 MeV wide, and ten bins in  $\cos\theta_{\pi^0}^*$ . The two cuts, used to select the BH candidate events, are shown in Fig. 4.39 and explicitly written in the Eqs. 4.15 and 4.16. Coefficients  $a$ ,  $b$  and  $d$  are both W

and  $\cos\theta_{\pi^0}^*$  dependent, while  $c$  empirically is found to be equal  $2 * 10^{-8}$ .

$$M_x^2 < -a + \sqrt{(b + c * (\Delta\phi_{\pi^0}^*)^2)}. \quad (4.15)$$

$$M_x^2 < \frac{d}{\phi_{\pi^0}^*}. \quad (4.16)$$

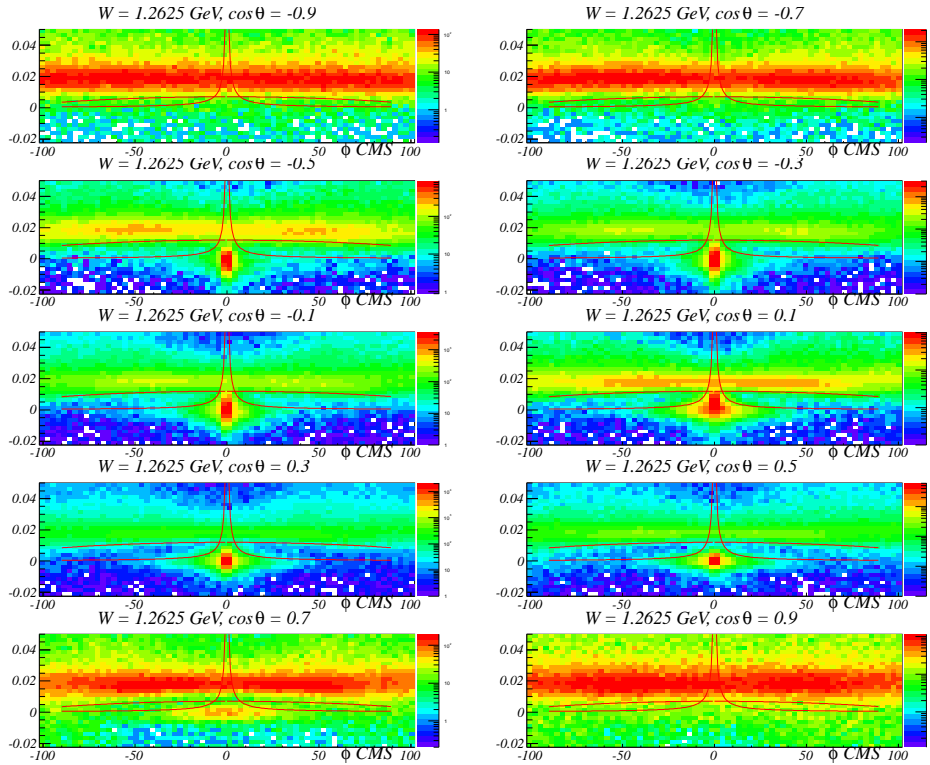


**Fig. 4.39:** The  $\phi_{\pi^0}^*$  of the pion versus missing mass squared. Events below red cut lines are BH candidates.

BH events tend to concentrate around 0 in  $\Delta\theta_i$  in the appropriate topology: preradiative events in the case of  $\theta_1$  and postradiative for the  $\theta_2$ . The candidate

events, determined with the cuts above are checked against the criteria based on the proton angles:  $\Delta\theta_1 < 5^\circ$  and  $\Delta\theta_2 < 20^\circ$  in a way that most of contamination stays on the left of the cut (Figs. 4.40 and 4.41). Such a big difference in the cut positions is explained by the different kinematical distributions of the BH events which spread up to high  $\Delta\theta$  in the second case. The final criteria of the Bethe-Heitler event is  $BH = (\phi_{\pi^0}^*) \times (\Delta\theta_1) \times (\Delta\theta_2)$ , while the rest is treated as pions.

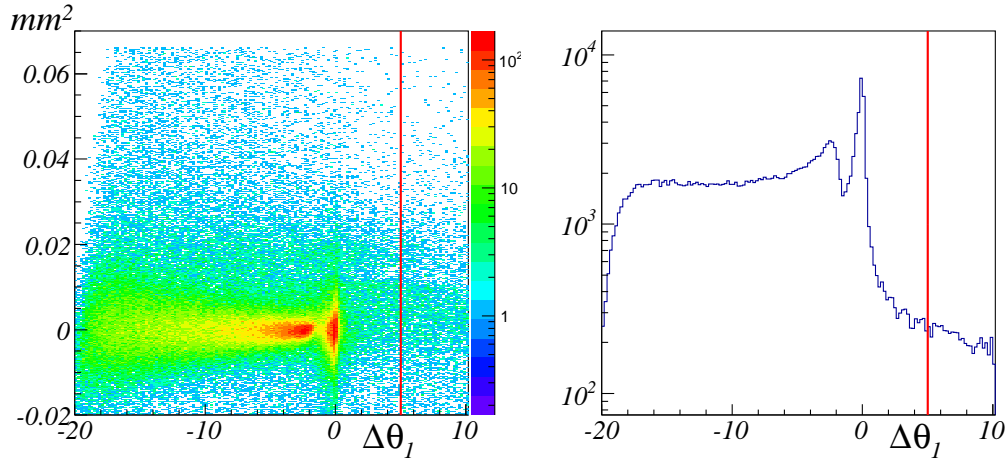


**Fig. 4.40:**  $\Delta\theta_1$  versus  $M_x^2$  (left plot) and its projection on the X axis. Events on the left of the cut line are BH contamination.

The illustration to the quality of the pion events selection is shown in Fig. 4.42. The cleanup of the BH events is satisfactory, but we unavoidably cut out good  $\pi^0$  events, especially at  $\phi_{\pi^0}^*$  around 180 degree. They are to be recovered using the simulation, where same cuts will be applied to pure pion events and should account for misidentified BH events.

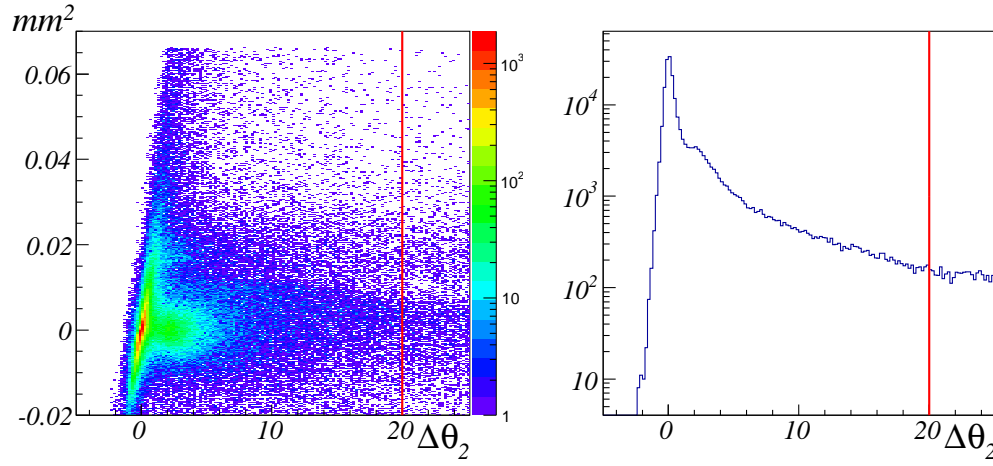


**Fig. 4.41:**  $\Delta\theta_2$  versus  $M_x^2$  (left plot) and its projection on the X axis. Events on the left of the cut line are BH contamination.

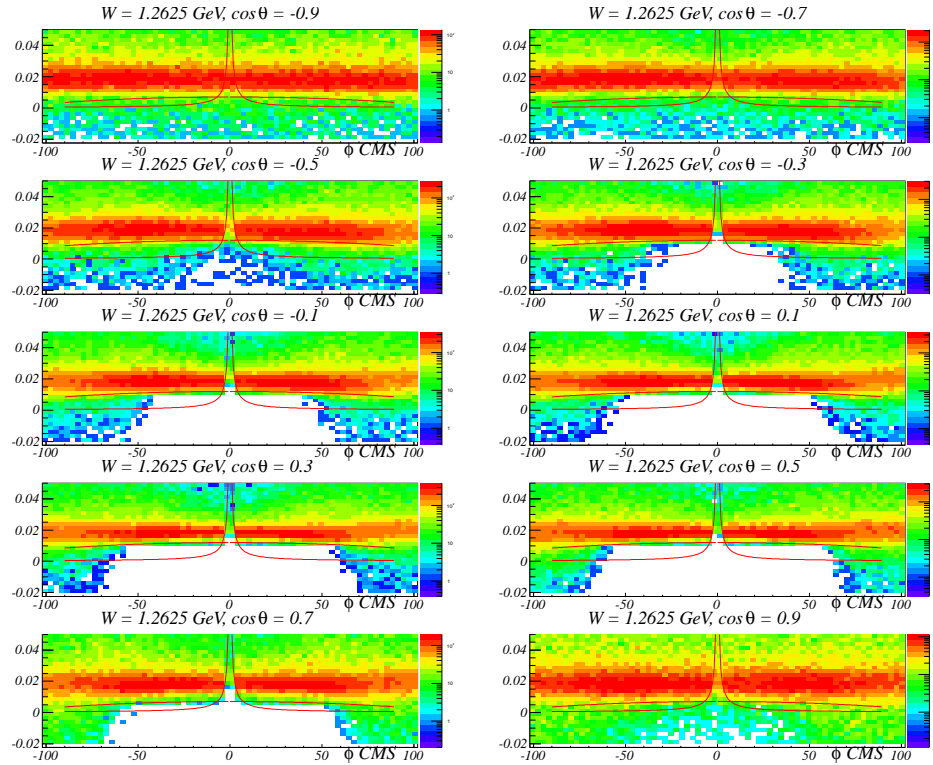


**Fig. 4.42:** The  $\phi_{\pi^0}^*$  of pion versus missing mass squared for selected single pion events.

## Chapter 5

### Simulation

#### 5.1 Overview

There are two major factors determining the detector efficiency: geometrical acceptance (i.e. the location of the active detector elements, capable of the particle registration) and efficiency in the active regions. For the measurements involving absolute normalization (like the cross section measurement in this analysis) we need to have a good understanding of the detector behavior.

The complete CLAS detector geometry, including the active and passive (support structures, etc) materials with their electromagnetic properties and magnetic fields is incorporated in the GSIM package (Geant SIMulation). This package is written in the Hall B of the Jefferson Lab using the GEANT 3 and provides the detector response in terms of the same raw signal (TDC, ADS) as the actual CLAS detector.

As an input GSIM accepts events which have to be generated elsewhere. For the reaction of interest  $ep \rightarrow ep'\pi^0$  we use the *aao\_rad* generator with the

MAID07 as the input model. It generates  $\pi^0$  events with the realistic radiative effects.

The raw data from the simulated detector are then reconstructed with the same reconstruction software used for the actual data with a certain modification: the GPP (GSIM Post Processor) is used to better match the resolution between data and simulation as discussed below. The full data flow is illustrated in the scheme 5.1:

$$\text{event generator}(aao\_rad \text{ with } MAID07 \text{ as input}) \Rightarrow GSIM \Rightarrow GPP \Rightarrow recsis. \quad (5.1)$$

Although the GSIM simulation involves all of the detector geometry and properties, it still overestimates the resolution of the drift chambers and TOF system. The following steps are taken to better match simulation to the data.

## 5.2 Drift chambers resolution

We can improve the agreement between data and simulation by using calDOCA (calculated distance of close approach), obtained from the charge collection time, compared to the more accurate fitDOCA, obtained from the fit to all the DC cells along the track (Fig. 5.1). The difference between them is a good measure of the DC resolution.

We plot the  $|calDOCA - fitDOCA|$  as a function of the fitDOCA, and fit

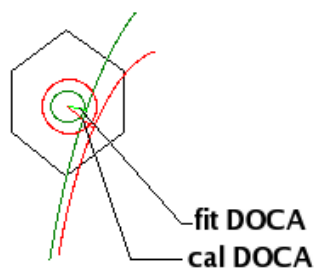


**Fig. 5.1:** calDOCA and fitDOCA measured from the charge collection time and from the track fitted using all the DC cells.

it with the 8<sup>th</sup> order polynomial (Fig. 5.2). By means of the *mysql* database the fit coefficients are accessible to the GPP code and are applied to the simulation. The same plot is produced for the simulation (Fig. 5.3) and shows the good match with the data.

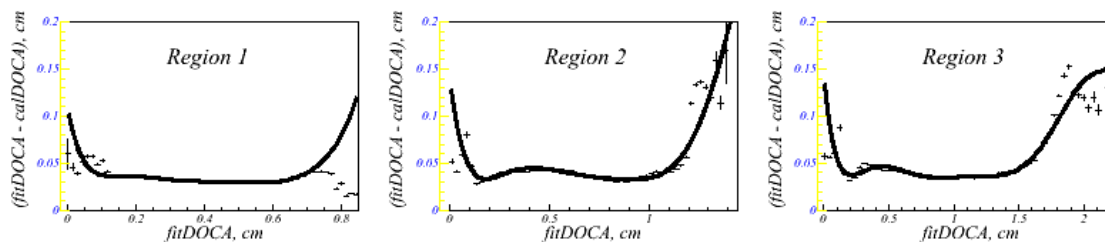


**Fig. 5.2:** The fit to the  $|fitDOCA - calDOCA|$  as a function of the fitDOCA. Black points are data, black solid line - 8<sup>th</sup> order polynomial fit.

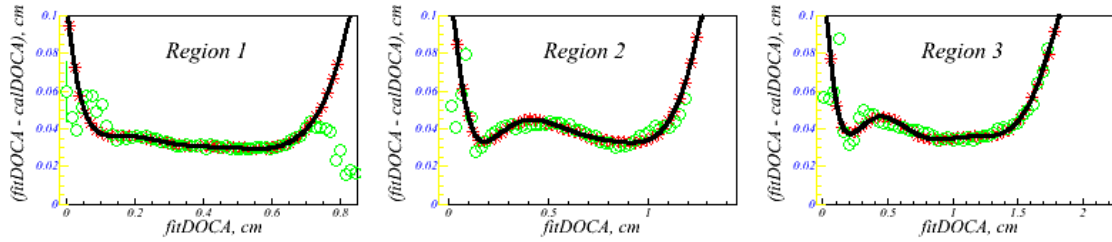


**Fig. 5.3:** The fit to the  $|fitDOCA - calDOCA|$  as a function of the fitDOCA. Green circles are data, red - simulation, black solid line -  $8^{th}$  order polynomial fit to the data points.

### 5.3 Time of flight and drift chambers smearing

The GSIM simulation of the TOF system of CLAS detector gives a better resolution than we obtain in data (Figs. 5.4, 5.5). Since our proton identification procedure is based on the TOF mass reconstruction, it is important to match the resolution between data and simulation. The mean position deviation, also found between data and simulation, does not affect results since this shift is easy to take into account. Correction procedure for resolution consists of adjusting the smearing parameters for simulation as follows: we vary the value of  $f$ , which is the parameter of the GPP code to add the additional TOF smearing, and fit TOF mass distribution with Gaussian. Width of the peak as a function of  $f$  along with resolution for data gives us the correct value of  $f$  (see Fig. 5.6). By means of the *mysql* database this parameter is used during the simulation processing.

Another discrepancy between data and simulation, which later can affect our

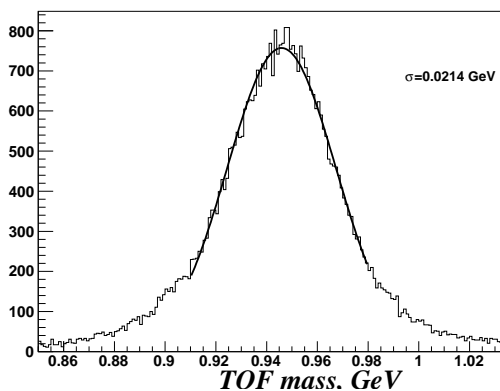


**Fig. 5.4:** TOF proton mass peak width for data.

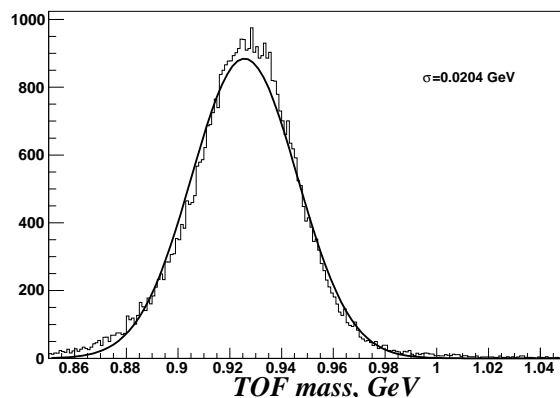


**Fig. 5.5:** TOF proton mass peak width for simulation without additional smearing.

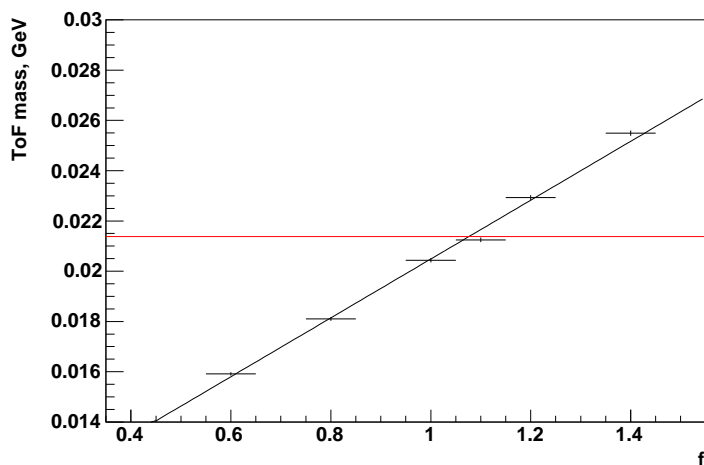


**Fig. 5.6:** Width of TOF proton mass peak versus smearing factor  $f$ . Horizontal red line represents width of the peak in data. Intersection at  $f = 1.1$  corresponds to the correcting factor to be used in simulation.

results, is the difference in the drift chambers resolution, which leads to different peak width of the  $M_x^2$ . In Figs. 5.8 and 5.9 missing mass squared distribution  $ep \rightarrow ep'X$  missing mass is plotted for both data and simulation. By the procedure similar to one used in TOF width matching we adjust width of the missing mass square peak in simulation (Fig. 5.7). In Figs. 5.8 and 5.9 the resulting distribution is plotted, showing that we have a match between the resolution in data and simulation with the smearing parameters  $a = b = c = 2.5$ . The more

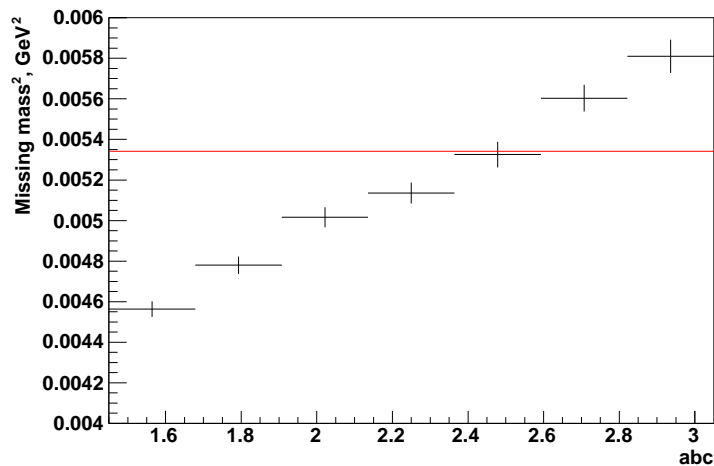


**Fig. 5.7:** Width of  $\pi^0$  missing mass peak versus smearing factor. Horizontal red line represents width of the peak in data. Intersection at  $a = b = c = 2.5$  corresponds to the correcting factor to be used used in simulation.

comprehensive comparison between data and simulation for a certain kinematical region is shown in Fig. 5.10. The agreement of the  $M_x^2$  position and width is very good and it holds independently of the particular kinematical bin.

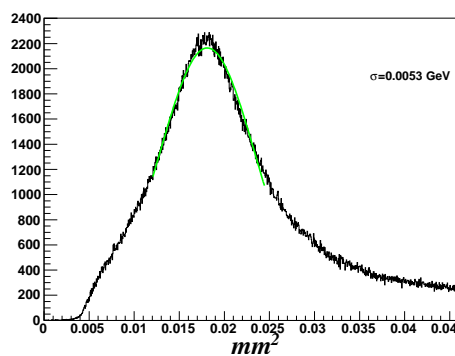


**Fig. 5.8:**  $\pi^0$  missing mass peak width for data. Width is  $0.0053 \text{ GeV}^2$ .

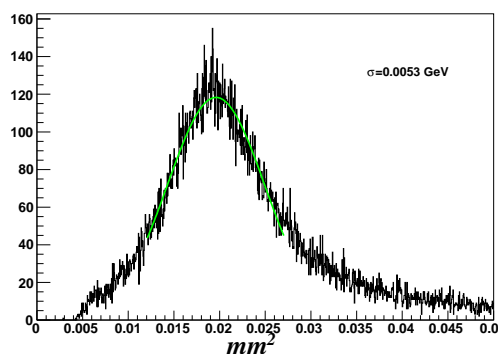


**Fig. 5.9:**  $\pi^0$  missing mass peak width for simulation with smearing factors  $a = b = c = 2.5$ . Width is  $0.0053 \text{ GeV}^2$ .

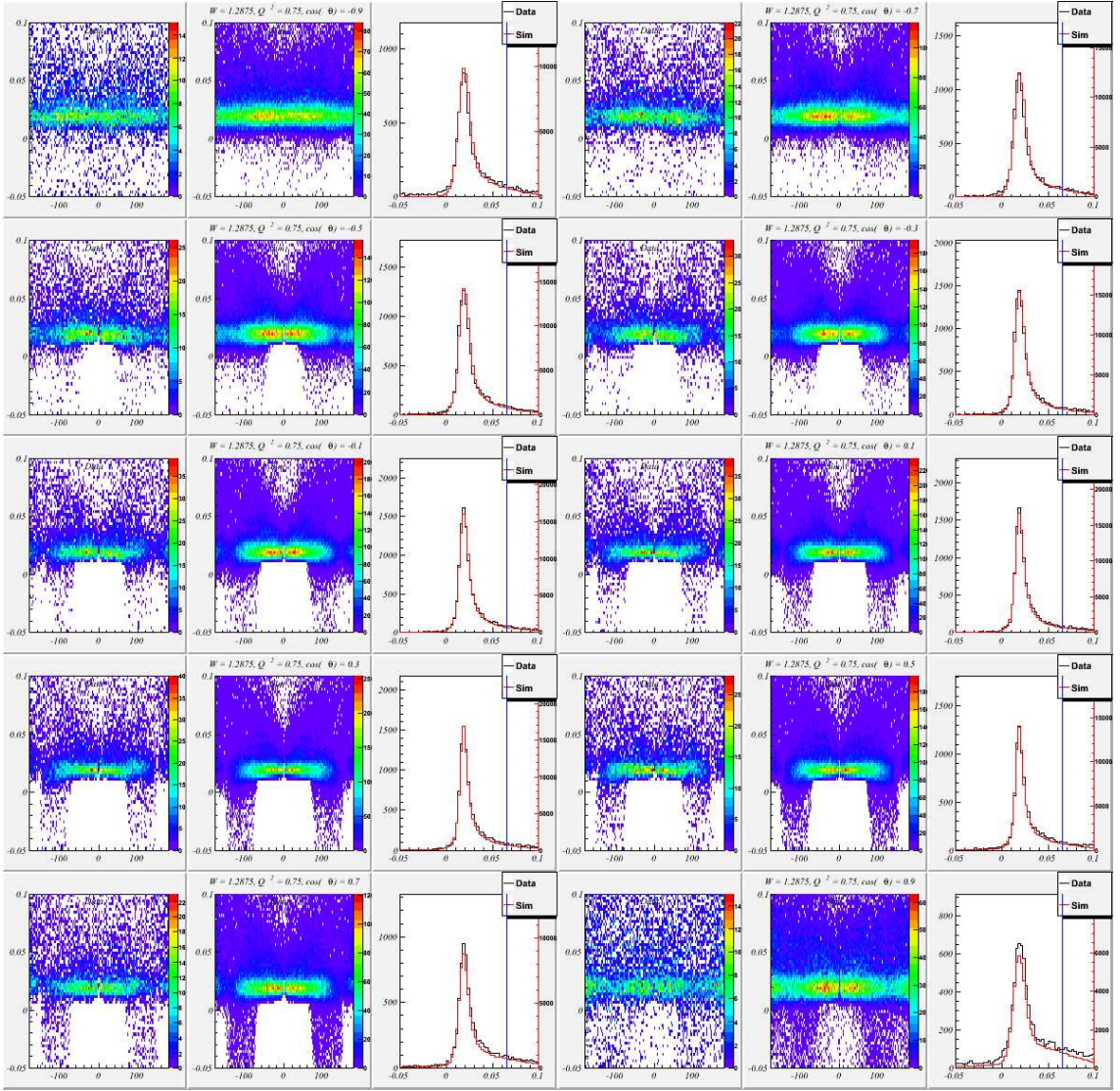


**Fig. 5.10:** Left to right:  $mm^2$  versus  $\phi_{\pi^0}^*$  for the data after  $\pi^0$  id,  $mm^2$  versus  $\phi_{\pi^0}^*$  for the simulation after  $\pi^0$  id, missing mass distribution for data and simulation overlapped for the  $W = 1.2875 \text{ GeV}$ ,  $Q^2 = 0.75 \text{ GeV}^2$  and different  $\cos\theta_{\pi^0}^*$  bins. The normalization factor is chosen as a ratio of the total number of the  $\pi^0$  events in data and simulation and is the same for all bins.

## Chapter 6

### Results

#### 6.1 Binning

The choice of the bin size is illustrated on the Fig. 6.1. The bin size and position choice was made keeping in mind that we need as fine bin as possible to address structure of the cross-section, and at the same time we need to have enough statistics in each bin to minimize statistical uncertainties. The compromise is presented in Table 6.1. All three resonance region, from the lower region of the  $\Delta$  resonance to the high lying third resonance region are covered.  $Q^2$  coverage is broader at lower W and due to kinematical limitations drops at higher invariant mass.

Angular binning in terms of  $\cos\theta_{\pi^0}^*$  and  $\phi_{\pi^0}^*$  can be found in Table 6.2 and coverage is illustrated on the Fig 6.2. Very important feature is virtually full angular coverage achieved in the experiment. It is necessary for the extraction of structure functions and subsequent Legendre multipole truncation analysis. Fine binning in  $\phi_{\pi^0}^*$  enables us to pick up subtle details of the cross section behavior.

Variable	Bin size	Number of bins	Lower limit	Upper limit
$W, GeV$	0.025	28	1.1	1.8
$Q^2, GeV^2$	0.1	6	0.4	1.0

**Table 6.1:**  $W$  and  $Q^2$  binning of the experiment.

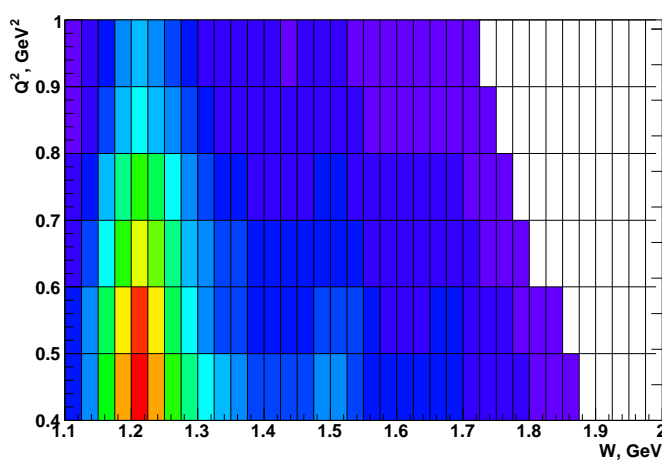


**Fig. 6.1:**  $W$  and  $Q^2$  binning for the  $\pi^0$  electroproduction events. Full resonance region is extensively covered.

Variable	Bin size	Number of bins	Lower limit	Upper limit
$\cos\theta^*$	0.2	10	-1	1
$\phi^*$	$15^\circ$	24	$0^\circ$	$360^\circ$

**Table 6.2:** Binning in  $\cos\theta_{\pi^0}^*$  and  $\phi_{\pi^0}^*$ .

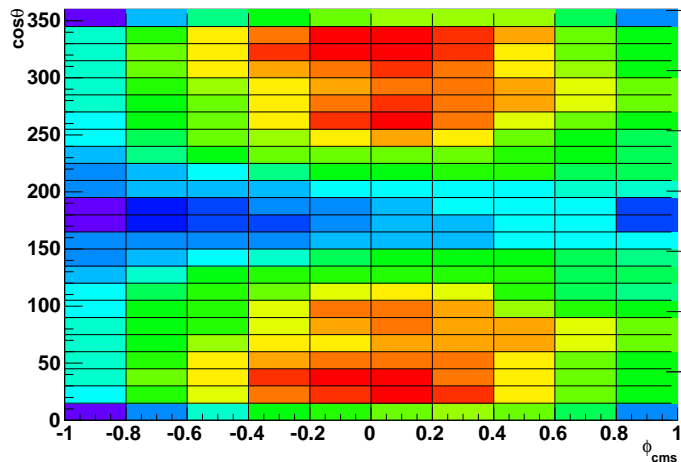


**Fig. 6.2:**  $\cos\theta_{\pi^0}^*$  and  $\phi_{\pi^0}^*$  binning for the  $\pi^0$  electroproduction events. Full angular coverage with fine  $\phi_{\pi^0}^*$  binning is crucial for future analysis.

## 6.2 Corrections

### 6.2.1 Radiative correction

$\pi^0$  production is not the only process contributing to the electroproduction cross section we measure. Other reactions affecting our results (Fig. 6.3), in the lowest order of the fine structure constant,  $\alpha$ , are:

- The bremsstrahlung process, when photon is emitted by incoming or outgoing electron;
- Vertex correction, when electron is emitted by incoming and absorbed by outgoing electron;
- Vacuum polarization, when virtual photon produces the  $e^-e^+$  pair, which

later annihilates back to the virtual photon.

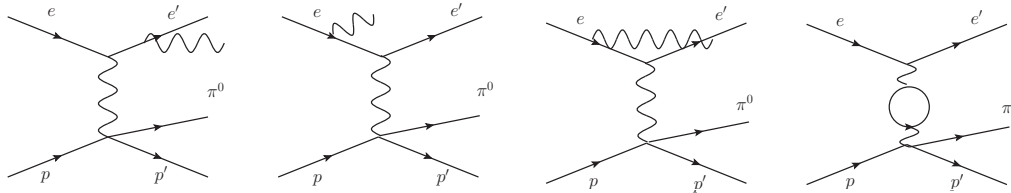


**Fig. 6.3:** Left to right: postradiative bremsstrahlung radiation, postradiative bremsstrahlung radiation, vertex modification, vacuum polarization.

These processes will be hard or even impossible to distinguish on the level of the event selection, especially when the energy of the emitted photon is within the detector resolution, so we need to correct for them. It brings in the radiative corrections procedure. The procedure used in the current analysis is based on the approach, developed in the [99] on the base of the covariant method for the infrared cancellation. This method has the following advantages over the widely adopted Mo-Tsai procedure:

- It allows us to calculate correction in case of the exclusive electroproduction, when the outgoing hadron is detected, as opposed to the inclusive case considered in Mo- Tsai;
- It uses all six structure functions, compared to two structure functions used in the inclusive case;
- The cancellation of infrared divergence, performed in Mo and Tsai approach

with the help of unphysical division of the phase space in the hard and soft part, is now done without such division.

A FORTRAN code named *EXCLURAD*, described in [99], was used to calculate radiative corrections. The program can take existing models (like MAID or SAID) to calculate the cross section and then radiate it to obtain the ratio

$$C(W, Q^2, \cos\theta_{\pi^0}^*, \phi_{\pi^0}^*) = \frac{\sigma_{rad}}{\sigma_{norad}}. \quad (6.1)$$

The complication arises from the fact that to calculate the detector acceptance we use the  $\pi^0$  events, generated with the *aao\_rad*, which incorporates its own method of the radiative correction calculations. So, in the final cross section the radiative events come to play two times, see Eqs. 6.2 (more detailed discussion is in [107]):

$$\begin{aligned} \sigma &= \sigma_{MEAS} * Acc * RadCorr, \\ Acc &= \frac{RADGEN_{aao\_rad}}{RADREC_{aao\_rad}}, \\ RadCorr &= \frac{NORADGEN_{exclurad}}{RADGEN_{exclurad}}, \end{aligned} \quad (6.2)$$

where

- $RADGEN_{aao\_rad}$  - number of events generated using *aao\_rad* (includes radiative correction);
- $RADREC_{aao\_rad}$  - number of events reconstructed from the Monte-Carlo simulation (above) after all the analysis cuts;

Cut type	$M_x^2$ cut	$V_{cut}$
Most loose	0.0874	0.0692
Loose	0.0766	0.058
Usual	0.0657	0.0475
Strict	0.0549	0.0367
Most strict	0.044	0.0258

**Table 6.3:** Position of missing mass cut on the data and corresponding  $V_{cut}$  used in *exclurad*.

- $RADGEN_{exclurad}$  - number of events generated with the radiative corrections from the *exclurad*;
- $NORADGEN_{exclurad}$  - number of events generated without the radiative corrections.

In case we use the same model for the radiative correction for events used in both *Acc* and *RadCorr* calculations the  $RADGEN_{aao\_rad}$  and  $RADGEN_{exclurad}$  should be identical and cancel out. However, in the present analysis the models used are slightly different, and one should be very cautious and try to minimize the divergence between the two. It is done by applying missing mass cut on both the *exclurad* calculation and for the events generated with *aao\\_rad*. Same cut is applied on reconstructed events (Table 6.3).

The effect of this cut will be discussed later in the section dedicated to the systematics studies. The correction itself as a function of the  $\cos\theta_{\pi^0}^*$  and  $\phi_{\pi^0}^*$  for one bin is presented in Fig. 6.4.

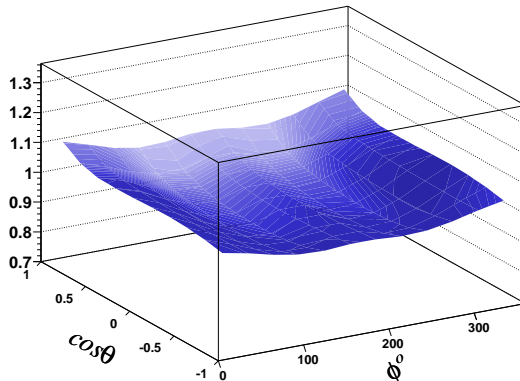


**Fig. 6.4:** Radiative corrections as a function of  $\cos\theta_{\pi^0}^*$  and  $\phi_{\pi^0}^*$  for  $W = 1.2625 \text{ GeV}$  and  $Q^2 = 0.75 \text{ GeV}^2$ .

### 6.2.2 Bin centering correction

When calculating the cross section, one actually obtain an average value inside the 4 dimensional  $W, Q^2, \cos\theta_{\pi^0}^*, \phi_{\pi^0}^*$  bin. Assigning this value to the center point of the bin is fully justified in case of the linear distribution of the variable of interest inside the bin (or in case of center-symmetric distribution), though in more realistic situation they do not coincide (Fig. 6.5).

The procedure was developed to calculate correction which takes this effect into account. By dividing each 4-fold  $W, Q^2, \cos\theta_{\pi^0}^*, \phi_{\pi^0}^*$  bin into 10 sub bins (total

of  $302 * 10^6$  bins), calculating cross section in each sub bin using MAID07 model predictions and then averaging them, we can obtain the correction as

$$C(W, Q^2, \cos\theta^*, \phi^*) = \frac{\sigma_{center}}{\sigma_{average}}. \quad (6.3)$$

Example of the correction for one  $W - Q^2$  bin is presented in Fig 6.6.

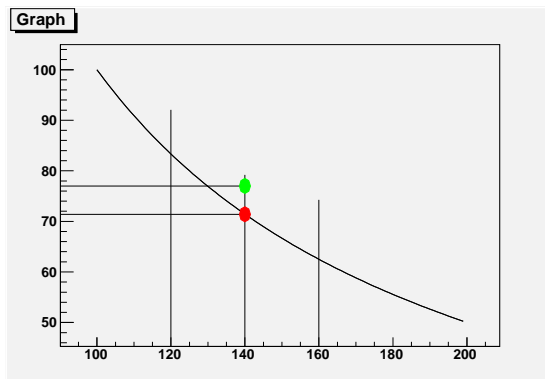


**Fig. 6.5:** Difference between center point of the bin (red circle) and bin average (green circle).

### 6.2.3 Acceptance correction

In order to calculate the acceptance of the detector in a given particular bin, we take number of events reconstructed in this bin and divide it by the number of events generated for the same bin (Eq. 6.4):

$$Acc = \frac{N_{rec}}{N_{gen}}. \quad (6.4)$$

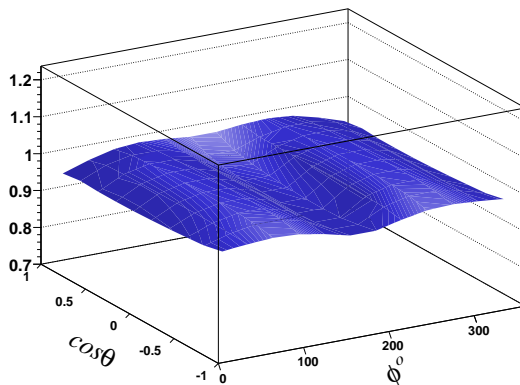


**Fig. 6.6:** Example of the bin centering correction as a function of  $\cos\theta_{\pi^0}^*$  and  $\phi_{\pi^0}^*$  for  $W = 1.2625 \text{ GeV}$  and  $Q^2 = 0.75 \text{ GeV}^2$ .

To smooth out possible variations of the final cross section due to acceptance, we divide each of the final bins in four subbins in  $\phi_{\pi^0}^*$  and calculate the acceptance for them. For that, all generated and reconstructed events are divided in 96 bins over the  $\phi_{\pi^0}^*$  (all other kinematical bins remain the same). The example of the acceptance is presented in Fig. 6.7

#### 6.2.4 Target wall subtraction

##### Using the forward foil

$\pi^0$  events can originate not only in the target media (hydrogen), but also in the walls of the target cell. Such events are to be excluded, and usual way to do so is by using the empty target runs, when the beam is projected onto the target without the hydrogen. The setup of the e1e target (Fig. 3.8) makes possible to extract the contribution from the target walls using the events originated in the

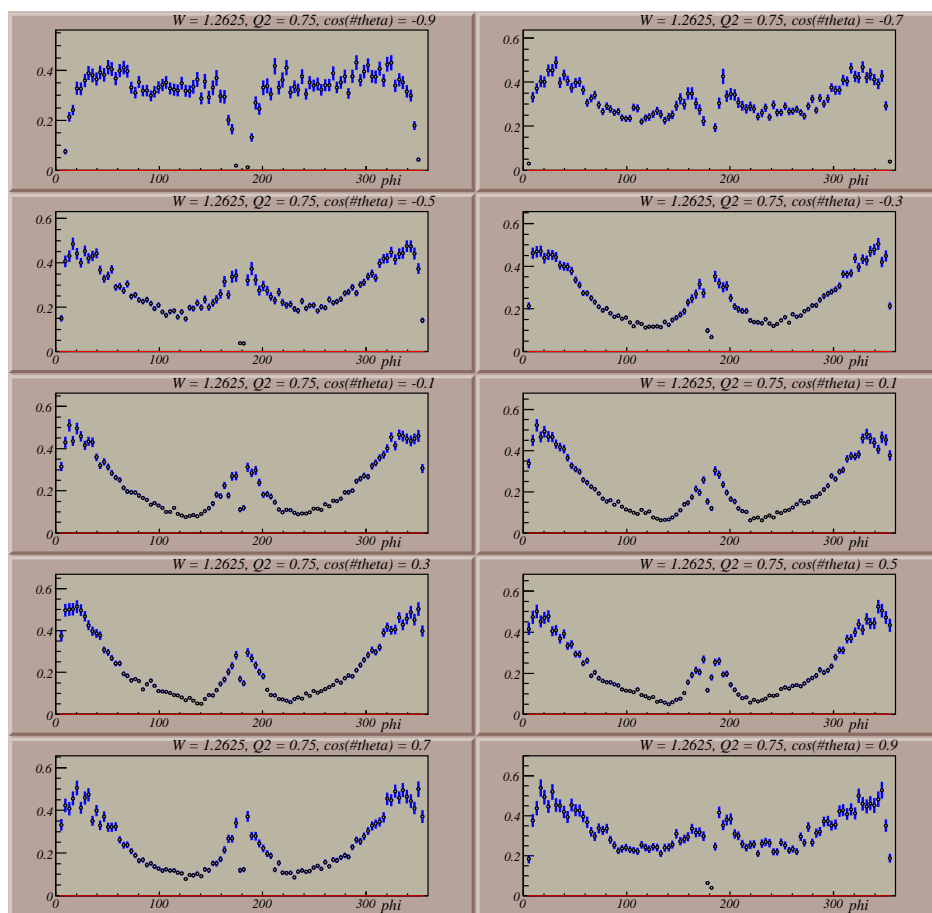


**Fig. 6.7:** Acceptance for one of the  $W - Q^2$  bins. Number of  $\phi_{\pi^0}^*$  bins is equal to 96, different panels correspond to different  $\cos\theta_{\pi^0}^*$  values.

forward foil, which is exactly the same as the entry/exit target windows.

First we apply exactly the same cuts and procedures to select  $\pi^0$  events, and then isolate events from the forward foil with the cuts on the vertex position illustrated in Fig. 6.8. The subtraction of the events is done bin by bin (foil events are divided exactly in the same kinematical bins as we divide our hydrogen data) using Equation 6.5 (note that we double the number of events since we need to subtract both events from the entry and exit windows of the target):

$$N_{final} = N_{target} - 2N_{foil}. \quad (6.5)$$

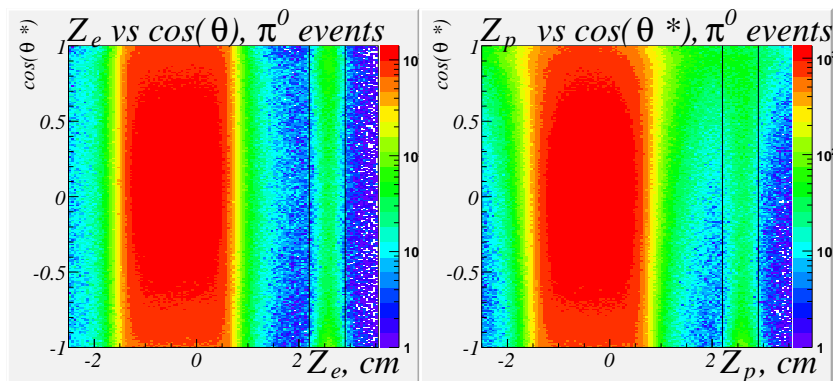


**Fig. 6.8:** For selected  $\pi^0$ , we isolate the events from the forward foil using the electron vertex coordinate  $1.5 < Z_e < 3.2\text{cm}$  (left plot).

The missing mass spectrum of the events, presented in Fig. 6.9, shows that the events from the empty target are clearly concentrated at lower  $M_x^2$  values, and although the proposed cleanup procedure works, there is still a contamination in

the region of lower  $M_x^2$ . Eliminated events are concentrated at lower  $W$ , so to have a better understanding of the events distribution in the wall of the target cell we will take a closer look at the lower  $W$  ( $W < 1.15 \text{ GeV}$ ) and  $\cos\theta_{\pi^0}^*$  ( $\cos\theta_{\pi^0}^* < -0.6$ ) region first. Fig. 6.10 shows, that the number of the events in the forward foil is smaller compared to the number of events in the target windows. It makes the method not reliable enough and forces us to look for a better procedure.

### **Empty target runs**

Out of the all data set, runs 36124, 36428, 36494 and 36495 were designed to address the problem with events contamination from the target cell windows: they were produced under the same conditions (magnet currents, beam energy, target position) as the other runs, but with the hydrogen chamber evacuated. They were reconstructed in the same way as the regular data files, and the same procedures for the events selection were applied.

The limited statistics obtained in these special runs virtually prohibits bin by bin subtraction, as we did using the forward foil, so we need to integrate out some of the variables. Careful inspection of the missing mass spectrum tells that the  $Q^2$  and  $\phi_{\pi^0}^*$  dependence are negligible compared to the  $W$  and  $\cos\theta_{\pi^0}^*$  and can be integrated out to increase the statistics. Event distributions as a function of  $W$  and  $\cos\theta_{\pi^0}^*$  are shown in Fig. 6.11. The binning in this variables is the same as for our final results.

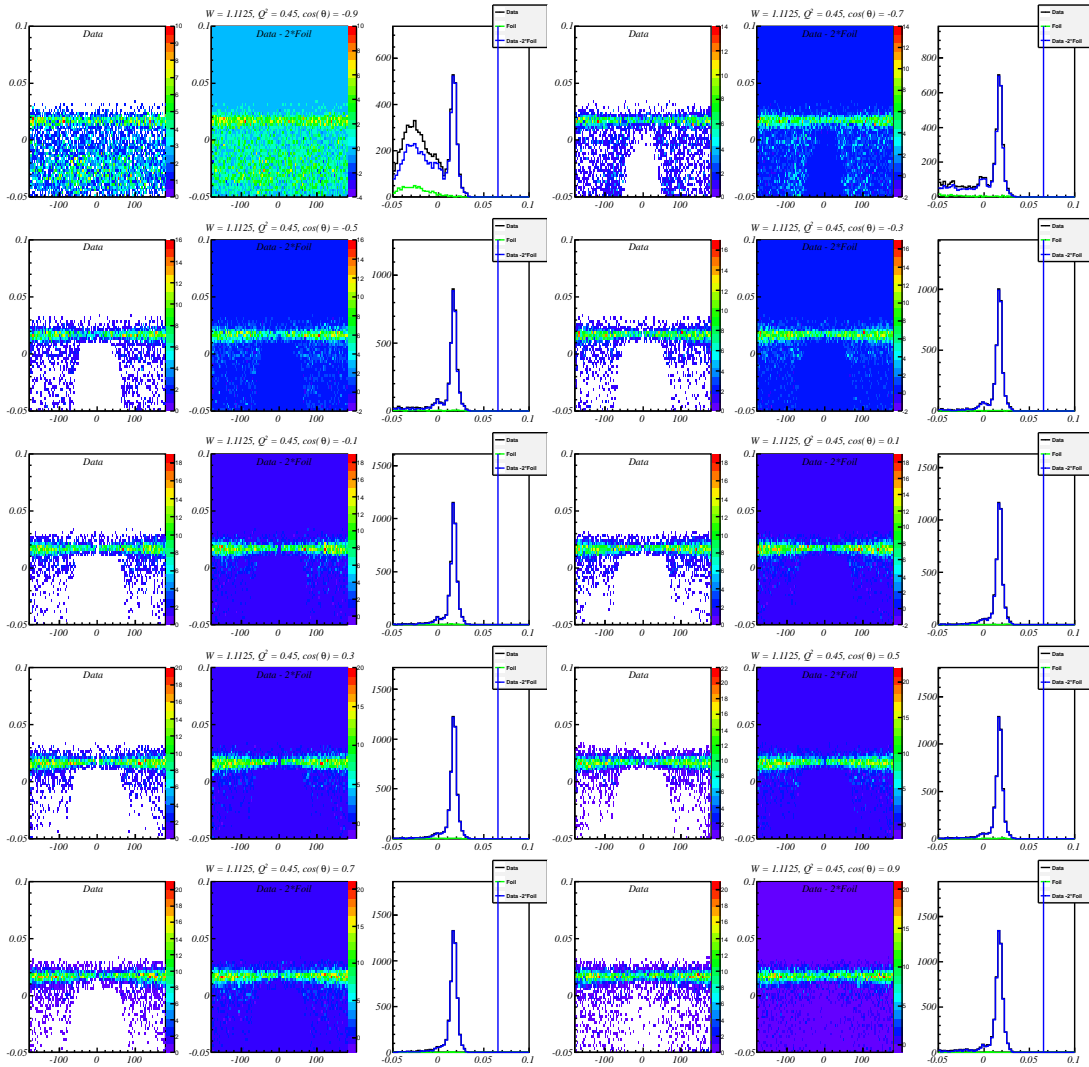


**Fig. 6.9:** All  $\pi^0$  events (black), events originated in the foil (green), result of the subtraction (blue) for lowest  $W$  bin. Different panels correspond to different values of the  $\cos(\theta_{\pi^0}^*)$ . Note the remaining contamination at the lowest  $\cos(\theta_{\pi^0}^*)$ .

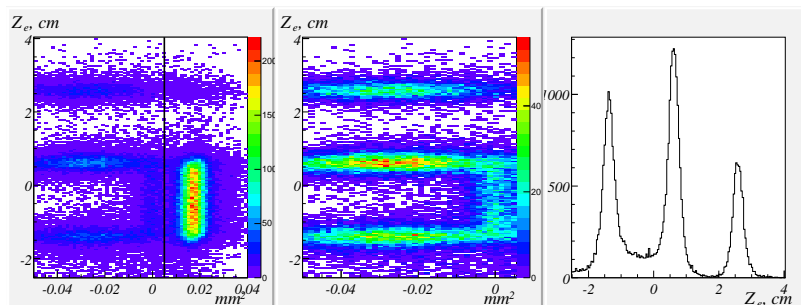


**Fig. 6.10:** Electron vertex coordinate versus missing mass squared for the  $W < 1.15$  GeV and  $\cos\theta_{\pi_0}^* < -0.6$  with proposed cut to select events at lower  $M_x^2$  (left plot); the same plot with the  $M_x^2$  cutoff at  $0.005 \text{ GeV}^2$  (middle plot); the projection of the middle plot on the Z axis. The right peak is the forward foil (right plot).

Now we have enough statistics accumulated in these bins and can proceed to the normalization of this events to the hydrogen data (it is done by taking the ratio of the charge on the Faraday Cup, corresponding to the empty target runs, to the charge, accumulated on the Cup during the data taking on the hydrogen, and dividing the number of events from the empty target by this coefficient, which is equal 0.022 for the present run conditions).

This correction is then applied to the data events on the bin by bin basis (it has the same value for different  $Q^2$  and  $\phi_{\pi_0}^*$  within one  $W - \cos\theta_{\pi_0}^*$  bin). The results obtained in both methods are compared for different W regions in Figs. 6.12 and 6.13. As expected, the correction is more important at lower W, and using the empty target gives larger effect, while at higher W the effect is very small for both methods.

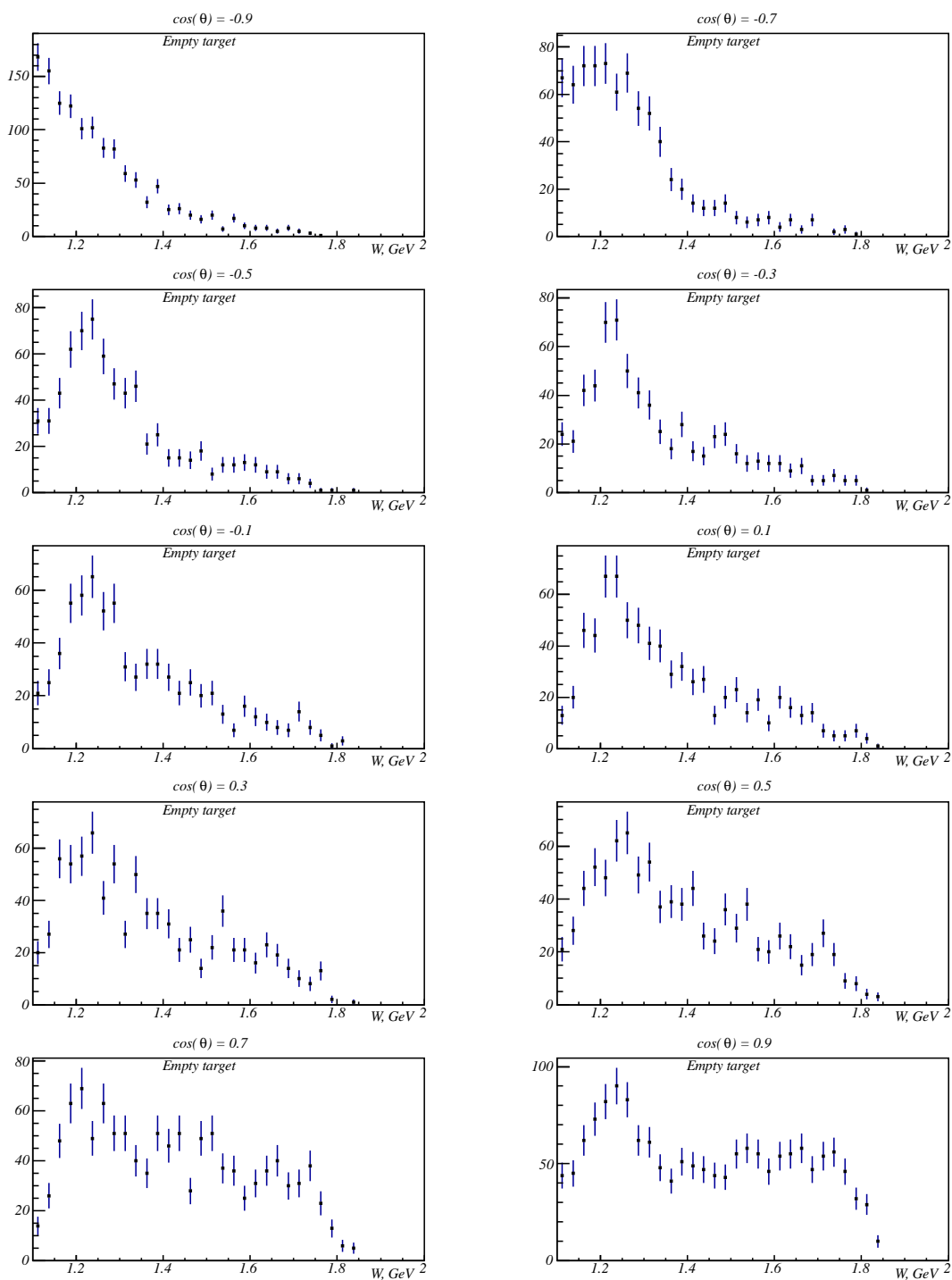


**Fig. 6.11:** Number of events from the empty target runs divided in the bins over  $W$  and  $\cos\theta_{\pi^0}^*$ .

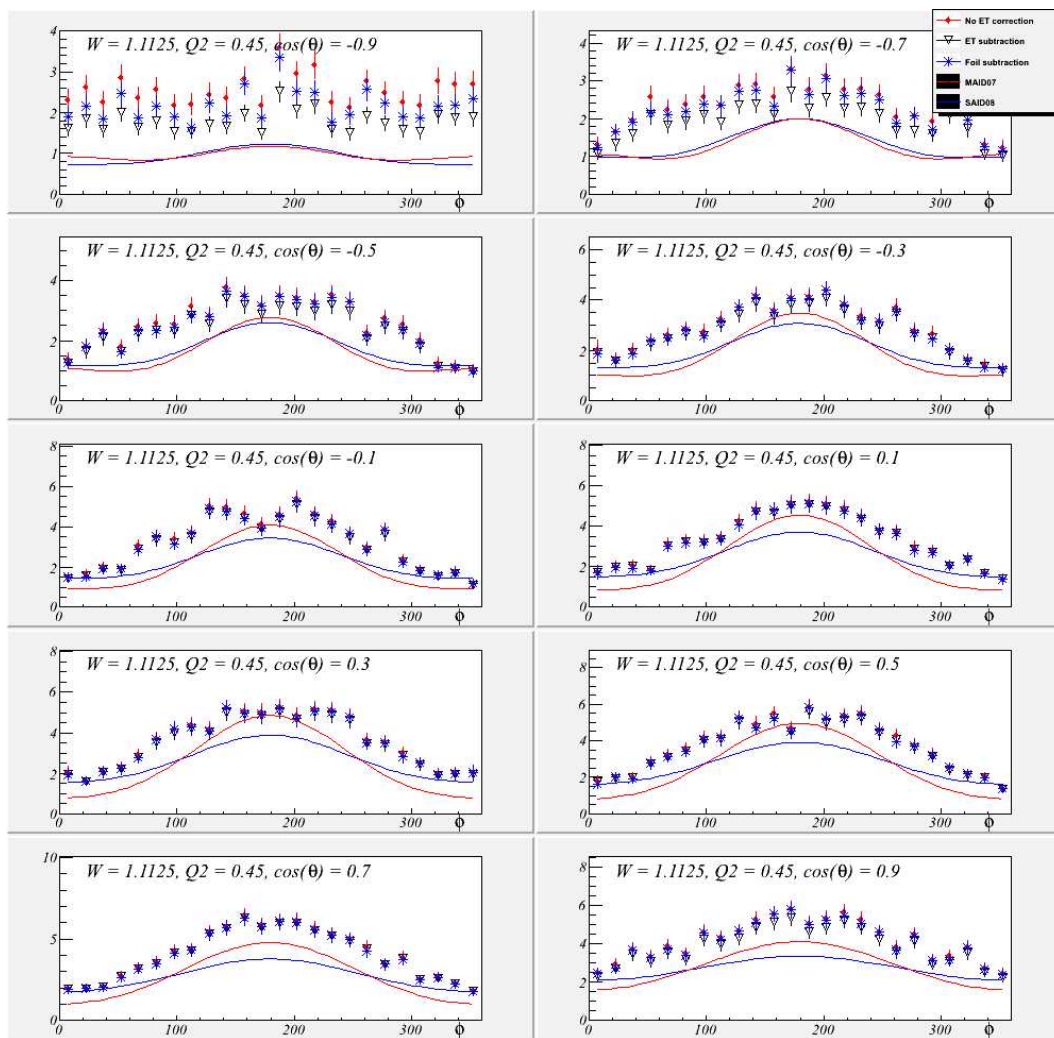


**Fig. 6.12:** Different methods of the target windows subtraction for different values of the  $\cos\theta_{\pi^0}^*$ . Red squares - data, no subtraction, black triangles - data, subtraction based on the empty target runs, blue stars - data, subtraction based on the forward foil events. Red solid line (MAID07 predictions) and blue solid line (SAID08 predictions) are shown for the reference. The correction is significant at lower  $\cos\theta_{\pi^0}^*$  values and is negligible as we go higher.

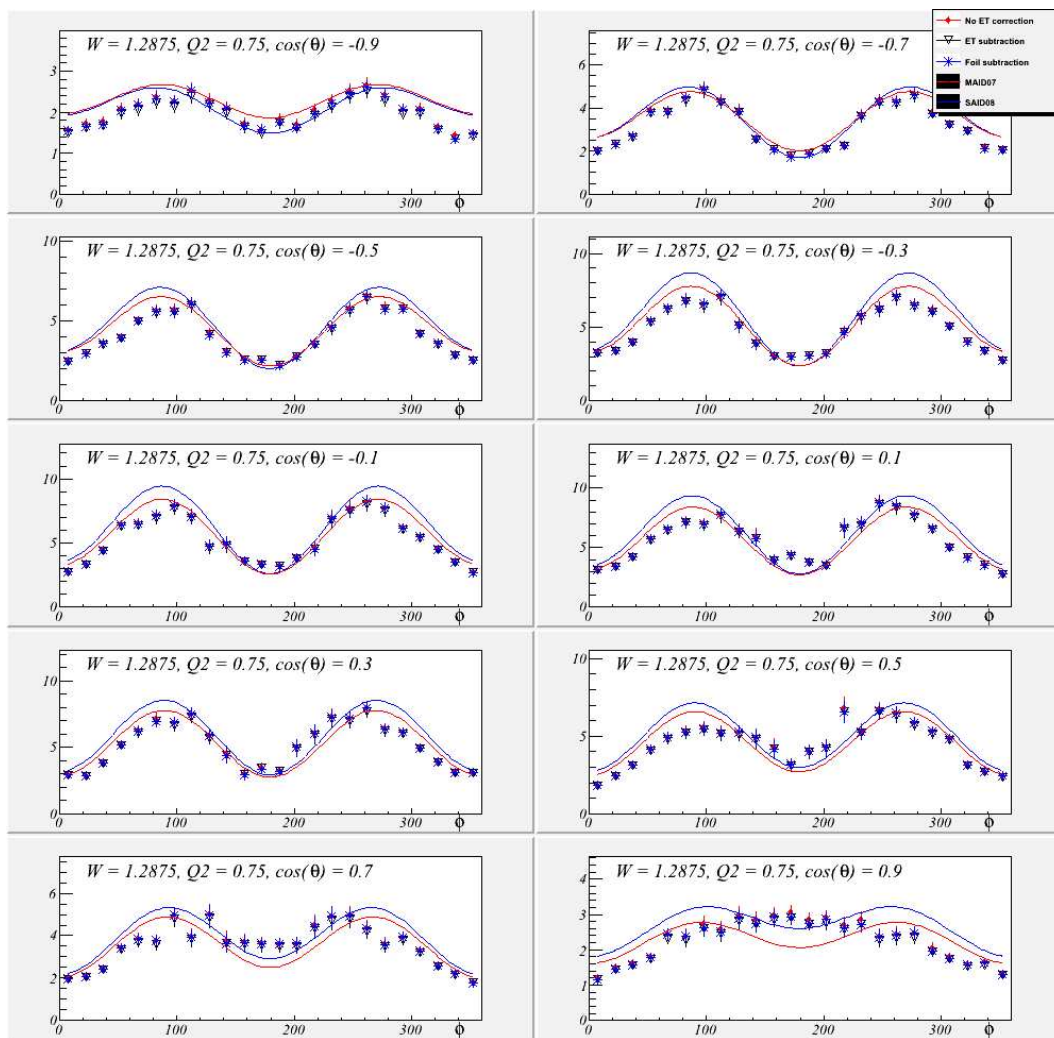


**Fig. 6.13:** Different methods of the target windows subtraction for different values of the  $\cos\theta_{\pi^0}^*$ . Red squares - data, no subtraction, black triangles - data, subtraction based on the empty target runs, blue stars - data, subtraction based on the forward foil events. Red solid line (MAID07 predictions) and blue solid line (SAID08 predictions) are shown for the reference. The correction at higher  $W$  region is negligible.

## Conclusion

The choice of the preferable correction method is a trade-off between the ability to make the bin-by-bin correction in case of the foil data, and more precise estimation of the number of the off target events in case of the empty target. Since the distribution of the foil events is virtually independent on the  $Q^2$  and  $phi_{\pi^0}^*$  we can sum over them and use the empty target method as the more precise one.

### 6.3 Cross section

General formula used to calculate the cross section given the number of the events in the specific  $W - Q^2 - cos\theta_{\pi^0}^* - \phi_{\pi^0}^*$  reads:

$$\frac{d\sigma}{d\Omega_{\pi^0}dWdQ^2} = N_{events} \frac{1}{N_e N_p} \frac{1}{R} E_{TOF} \frac{1}{A} B \frac{1}{\Delta W \Delta Q^2 \Delta cos\theta_{\pi^0} \Delta \phi_{\pi^0}} \frac{1}{\Gamma}, \quad (6.6)$$

where  $N_{events}$  is the number of events in the 4-differential bin,

$$N_e = \frac{Q_F}{e} \quad (6.7)$$

is the number of electrons delivered to the target with accumulated charge on the Faraday cup  $Q_F = 0.00549 \text{ Coulomb}$ , and  $e$  is the electron charge.

$$N_p = \frac{L_t \rho N_A}{M_h} \quad (6.8)$$

is the number of protons with  $L_t = 2 \text{ cm}$  is the target length,  $\rho = 0.0708 \text{ /cm}^3$  is the liquid hydrogen density at  $T = 20K$ ,  $N_A = 6.02 \cdot 10^{23}$  is the Avogadro number and  $M_H = 1.00794 \text{ g/mol}$  is the atomic mass unit of the natural mixture of the

hydrogen.  $A$ ,  $B$ , and  $R$  is acceptance, bin centering and radiative corrections, respectively.  $E_{TOF} = 1.05$  is the correction to account for the time of flight inefficiency.  $\Delta W$ ,  $\Delta Q^2$ ,  $\Delta \cos\theta_{\pi^0}^*$ , and  $\Delta\phi_{\pi^0}^*$  is the bin size for the corresponding variable (see Table 6.1 and Table 6.2).

$$\Gamma = \frac{\alpha}{2\pi^2} \frac{e'}{e} \frac{k_\gamma}{Q^2} \frac{1}{1 - \epsilon} \quad (6.9)$$

is the virtual photon flux with the  $\alpha$  - fine structure constant,  $e'$  - momentum of the scattered electron,  $e$  - momentum of the initial electron (beam energy),  $k_\gamma = \frac{W^2 - m_p^2}{2m_p}$  - photon equivalent energy.

Since for the acceptance we use fine  $\phi_{\pi^0}^*$  binning of the 3.75 degrees instead of 15 used for the final results, technical details of how we get to the cross section are explained below:

- We group sub bins in each bin in pairs (we have four sub bins, so we group SB1 with SB2 and SB3 with SB4);
- For each pair we calculate the cross section separately. There are four cases:

1. We have some events in both the SB1 and SB2, and acceptances for the sub bin are nonzero as well. In this case, the cross section will be:

$$CS1 = \frac{nData1}{Acc1}, \quad (6.10)$$

$$CS2 = \frac{nData2}{Acc2}, \quad (6.11)$$

$$CS = CS1 + CS2; \quad (6.12)$$

2. We have events some in both the SB1 and SB2, and one of the acceptances for the sub bin (lets say  $Acc1$ ) is zero. The cross section will be:

$$CS1 = \frac{nData1}{Acc2}, \quad (6.13)$$

$$CS2 = \frac{nData2}{Acc2}, \quad (6.14)$$

$$CS = CS1 + CS2; \quad (6.15)$$

3. We have zero events in one of the data sub bin (suppose SB1), and at least one of the acceptances is not zero:

$$CS = \frac{nData1}{\left(\frac{Acc1+Acc2}{2}\right)} \quad (6.16)$$

$$(6.17)$$

4. We have zero events in both the SB1 and SB2, or  $Acc1 = Acc2 = 0$ .

In this case section is set to be 0

- The cross section for the full bin is then calculated as the sum of the cross sections in the pairs (SB1 SB2) and (SB3 SB4).

We start to present our result by showing the  $W$  dependence of measured cross section. It is important to see overall picture and check if it agrees with model in the well established regions before going into more details. Fig. 6.14 clearly shows such an agreement at lower  $W$  along with enhancements at higher  $W$  (also predicted by models).

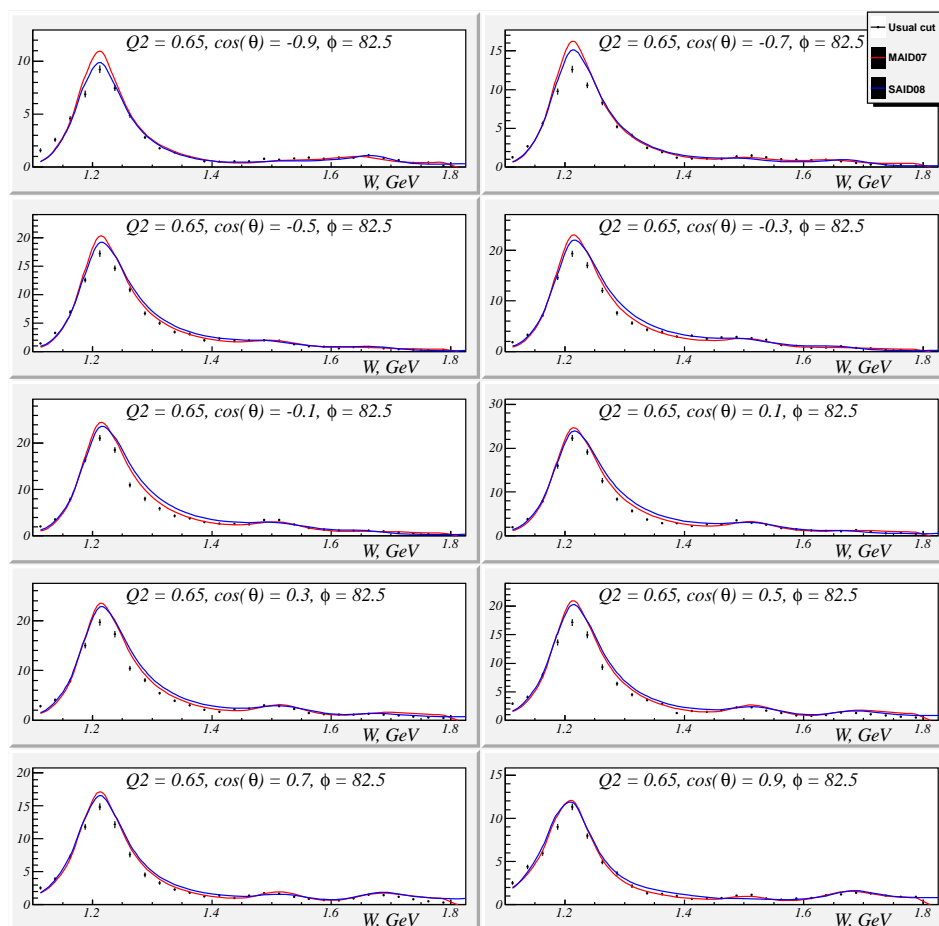


**Fig. 6.14:**  $W$  dependence of the cross section at fixed values of  $Q^2$  and  $\phi_{\pi^0}^*$ . Different panels correspond to different values of  $\cos\theta_{\pi^0}^*$ .

Angular dependencies of cross section give more details and better understanding of the quality of measured data. In Fig. 6.15 we present the value of the cross section calculated at the lower W region. This region is well established from other experiments and is accurately incorporated in the modern models, so drastic variation of reported result would indicate a systematical error. From Fig. 6.15 we see that the results are in a good agreement with the predictions of both models.

Second resonance region is as extensively covered in world data on  $\pi^0$  electroproduction, so the comparison to models might serve only as a approximate check. Important features to look at are absence of unphysical behavior of the measured cross section and symmetry over  $\phi_{\pi^0}^* = 180^0$ . In Fig. 6.16 we see that both features are presented. Note also wide coverage in  $\phi_{\pi^0}^0$ .

Even at higher W (Fig. 6.17) we have accumulated statistics large enough to study angular dependence of the cross section. Agreement with models is a bit of surprise, due to lack of the experimental data at this region.

#### 6.4 Structure functions

$\pi^0$  differential cross section in the resonance center of mass system assumes the form:

$$\frac{d\sigma}{d\Omega_{\pi^0}} = \frac{2Wp_{\pi^0}}{W^2 - m_P^2} (\sigma_T + \epsilon\sigma_L + \sigma_{TT} \sin^2\theta_{\pi^0}^* \cos 2\phi_{\pi^0}^* + \sigma_{LT} \sqrt{2\epsilon_L(\epsilon + 1)} \sin\theta_{\pi^0}^* \cos\phi_{\pi^0}^*), \quad (6.18)$$

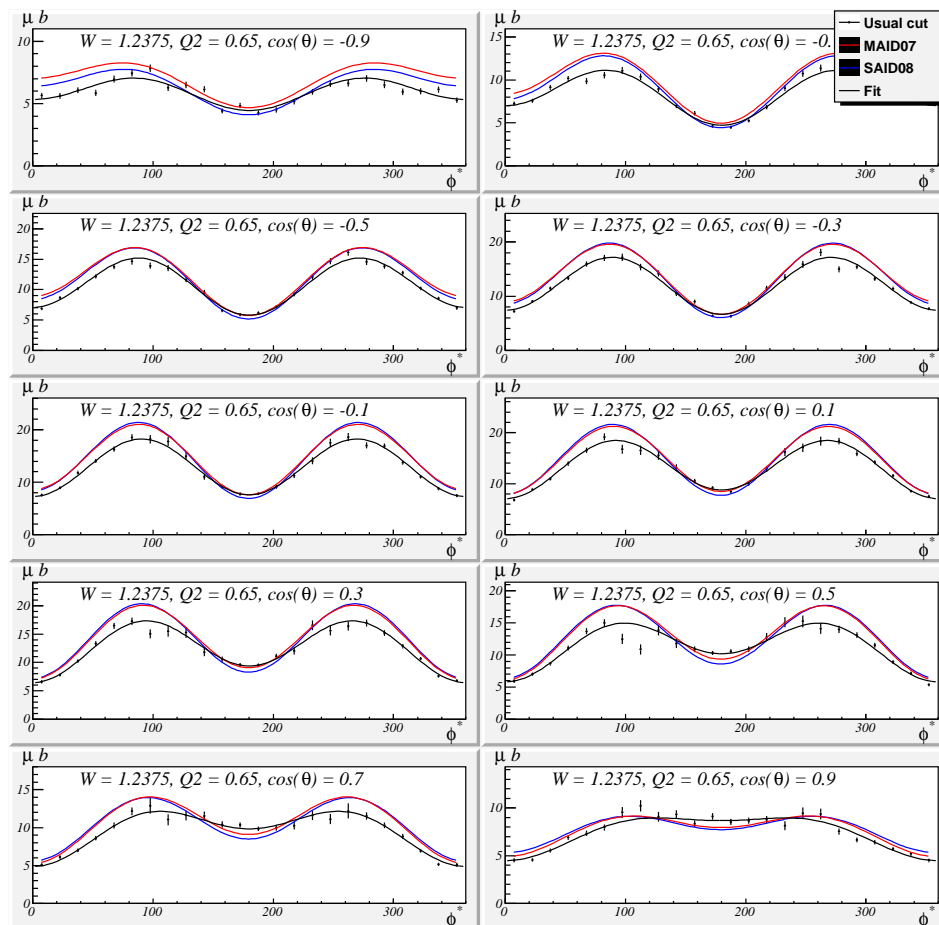


**Fig. 6.15:** Sample cross section for one  $W - Q^2 - \cos\theta_{\pi_0}^*$  bin near the  $\Delta$ , overlapped with MAID07 (red line) and SAID08 (blue line) predictions. Black solid line is the fit to extract structure functions (more details in the Section 6.4).

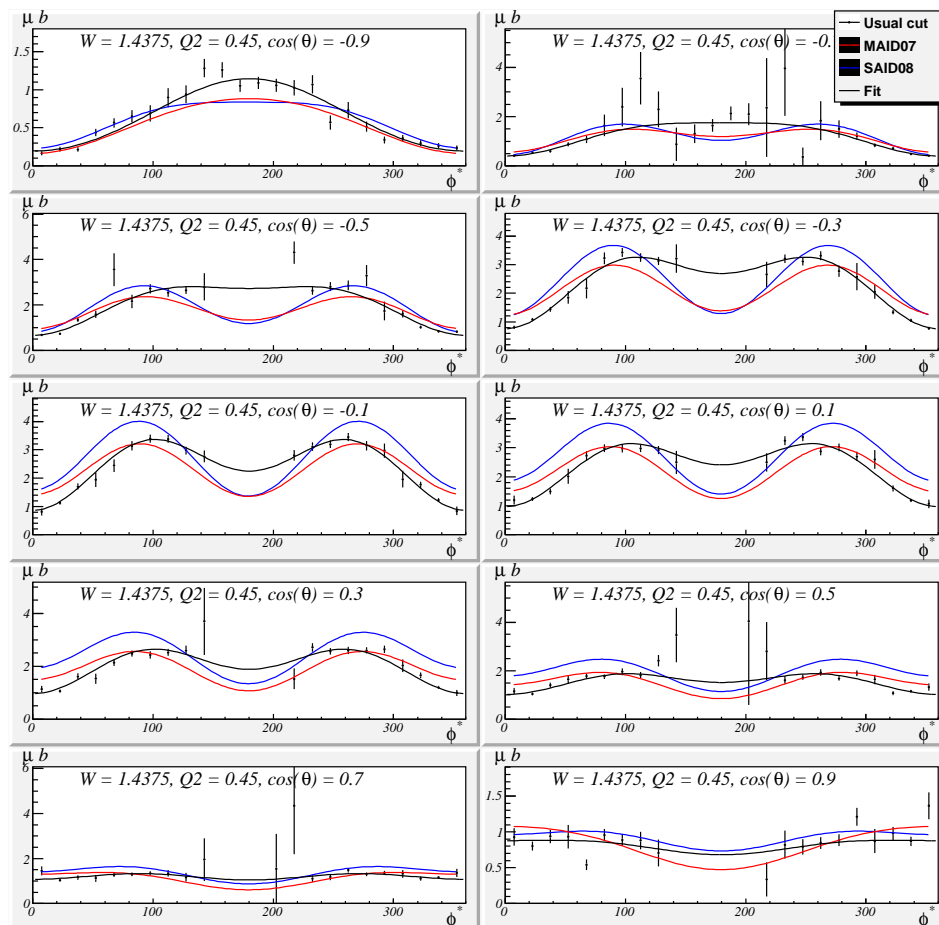


**Fig. 6.16:** Sample cross section for one  $W - Q^2 - \cos\theta_{\pi^*}^*$  bin at the  $W = 1.4375$  GeV overlapped with MAID07 (red line) and SAID08 (blue line) predictions. Black solid line is the fit to extract structure functions (more details in the Section 6.4).

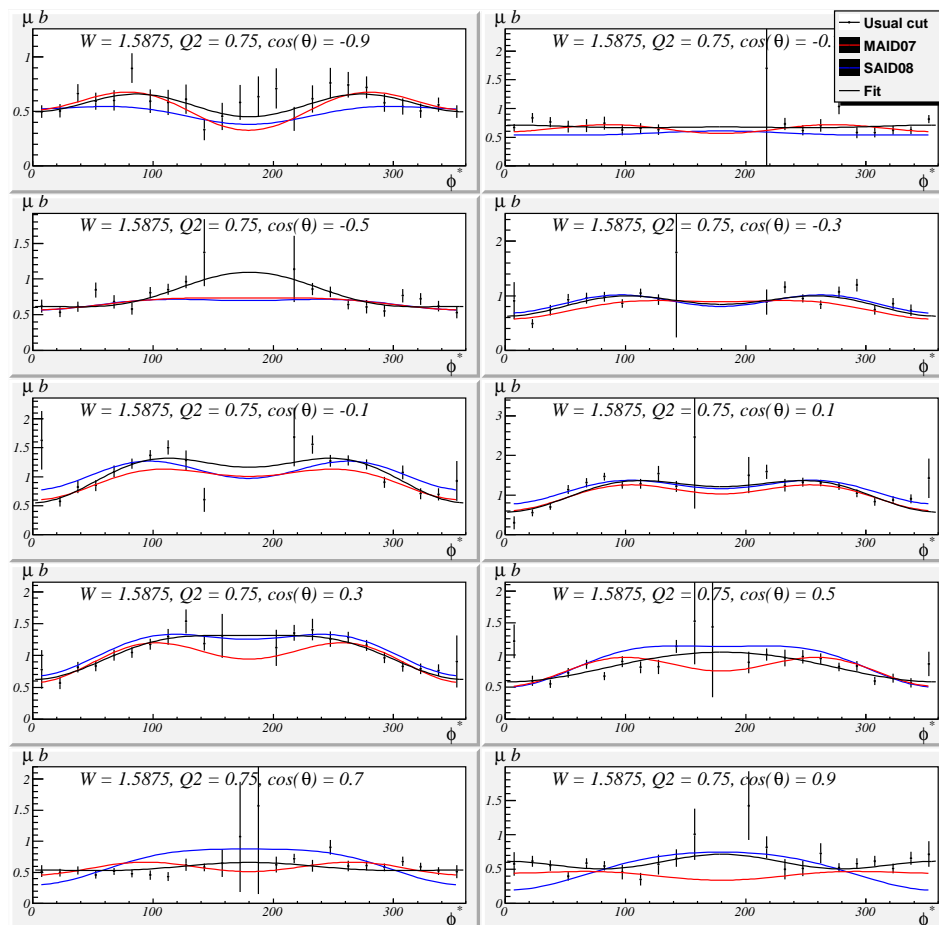


**Fig. 6.17:** Sample cross section for one  $W - Q^2 - \cos\theta_{\pi^0}^*$  bin at the  $W = 1.5875$  GeV overlapped with MAID07 (red line) and SAID08 (blue line). Note higher  $Q^2$  value. Black solid line is the fit to extract structure functions (more details in the Section 6.4).

where  $\epsilon$  is the transverse polarization of the virtual photon. The structure functions  $\sigma_T + \epsilon\sigma_L$ ,  $\sigma_{TT}$  and  $\sigma_{LT}$  depend on the  $W$ ,  $Q^2$  and  $\cos\theta_{\pi^0}^*$  but not on the  $\phi_{\pi^0}^*$ , so that the cross section is modulated by the  $\cos\phi_{\pi^0}^*$  and  $\cos 2\phi_{\pi^0}^*$  in the azimuthal angle, and the extraction of the structure functions via the  $\phi_{\pi^0}^*$ -dependent fit is possible. For that, we fit the quantity in parenthesis of Eq. 6.18 with the

$$y = a + \cos\phi + \cos 2\phi. \quad (6.19)$$

Black solid line in Figs 6.15, 6.16 and 6.17 is the fit with functions described above. Chi squared distribution  $\chi^2/\nu$ , where  $\nu$  is number of degrees of freedom of the fit (Eq. 6.20) is shown in Fig. 6.18.

$$\nu = N - \text{constraints} = 21, \quad (6.20)$$

where

$$N = 24, \text{ number of points to fit,} \quad (6.21)$$

$$\text{constraints} = 3, \text{ number of fit parameters.} \quad (6.22)$$

The structure functions are presented in Figs. 6.19- 6.27. Again, we show results for all three  $W$  regions and overlap them with the MAID07 and SAID08 model predictions. New features, additional to comparison of cross sections is the  $Q^2$  dependence of measurements. Fit, described above, smoothed out oscillations which are present in cross sections, and overall agreement between data and model

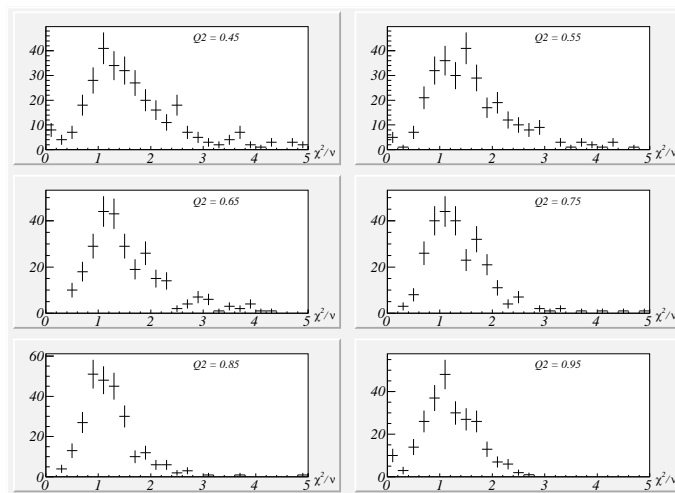


**Fig. 6.18:**  $\chi^2/\nu$  distributions for the different  $Q^2$  bins. The center of each distribution is around one, which confirms the quality of the fit.

is good at lower W. Higher W result are in agreement as well, but, more important, do not show unphysical behavior.

Comparison to available world data will be performed in the next chapter after extraction of Legendre coefficients.

## 6.5 Absolute normalization

There are number of additional steps which we will undertake to make reported results more convincing.

First, we will examine the experimental data to see if the variations of the experimental condition are too broad and we need to exclude some of the dataset from further consideration.

Second, we will put our particle identification and event selection procedures

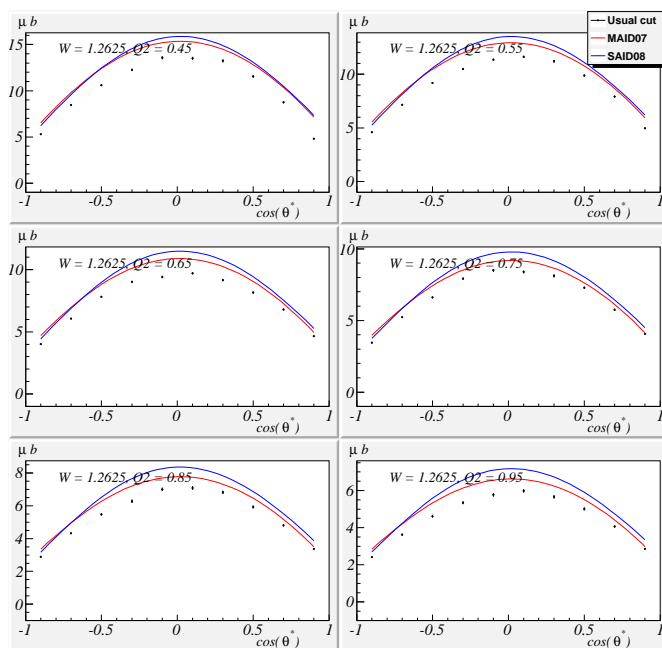


**Fig. 6.19:**  $\sigma_T + \epsilon\sigma_L$  from Eq. 6.18 in  $W$  range around  $\Delta$  in different  $Q^2$  bins overlapped with predictions of the models.

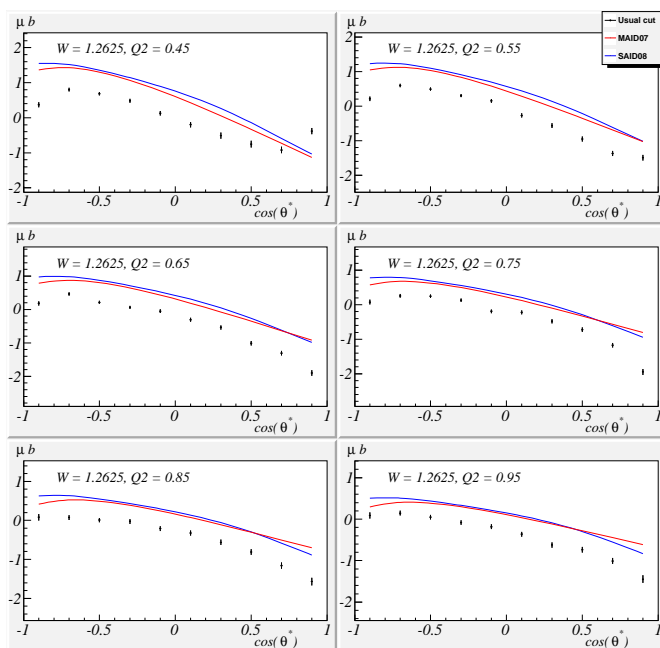


**Fig. 6.20:**  $\sigma_{LT}$  from Eq. 6.18 in  $W$  range around  $\Delta$  in different  $Q^2$  bins overlapped with predictions of the models.

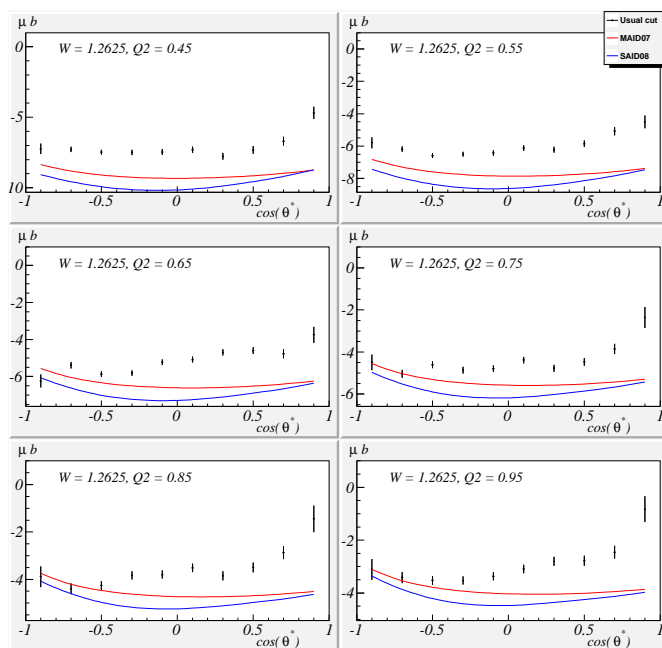


**Fig. 6.21:**  $\sigma_{TT}$  from Eq. 6.18 in  $W$  range around  $\Delta$  in different  $Q^2$  bins overlapped with predictions of the models.

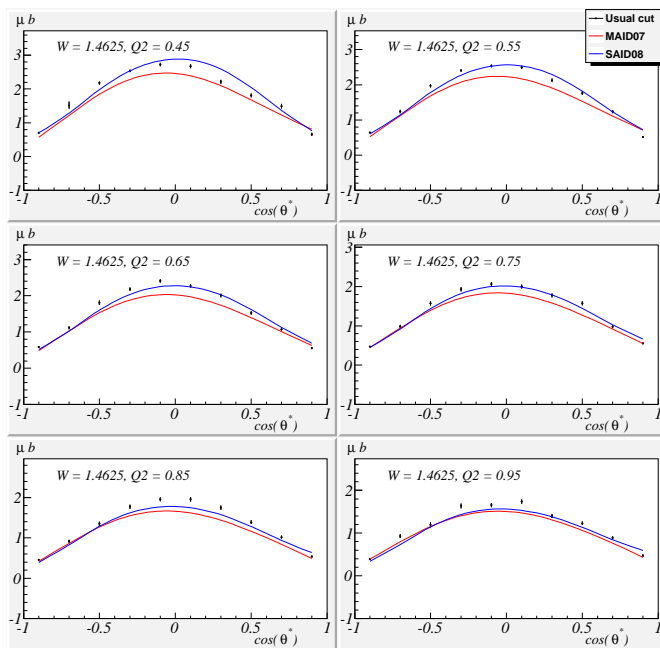


**Fig. 6.22:**  $\sigma_T + \epsilon\sigma_L$  from Eq. 6.18 at  $W = 1.4625$  GeV in different  $Q^2$  bins overlapped with predictions of the models.

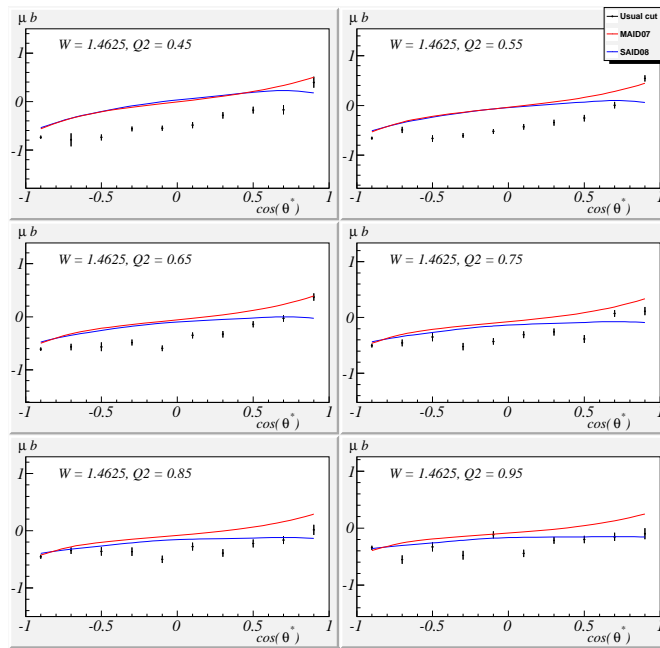


**Fig. 6.23:**  $\sigma_{LT}$  from Eq. 6.18 at  $W = 1.4625$  GeV in different  $Q^2$  bins overlapped with predictions of the models.

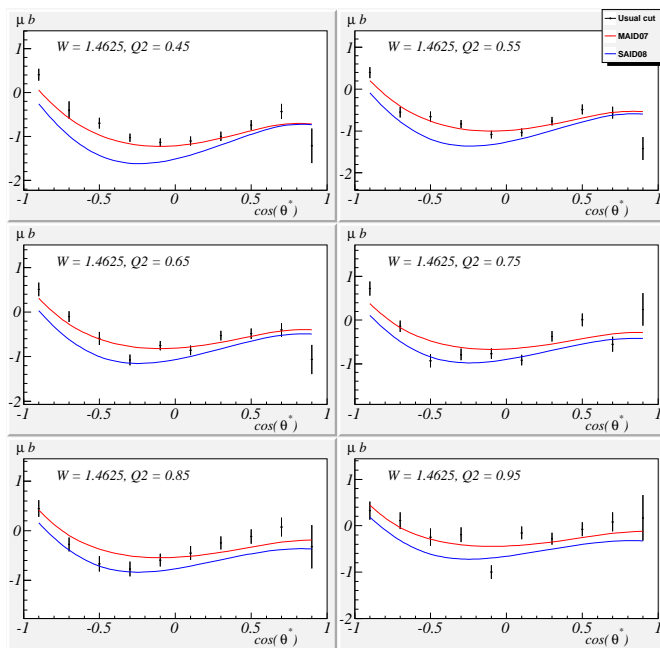


**Fig. 6.24:**  $\sigma_{TT}$  from Eq. 6.18 at  $W = 1.4625$  GeV in different  $Q^2$  bins overlapped with predictions of the models.

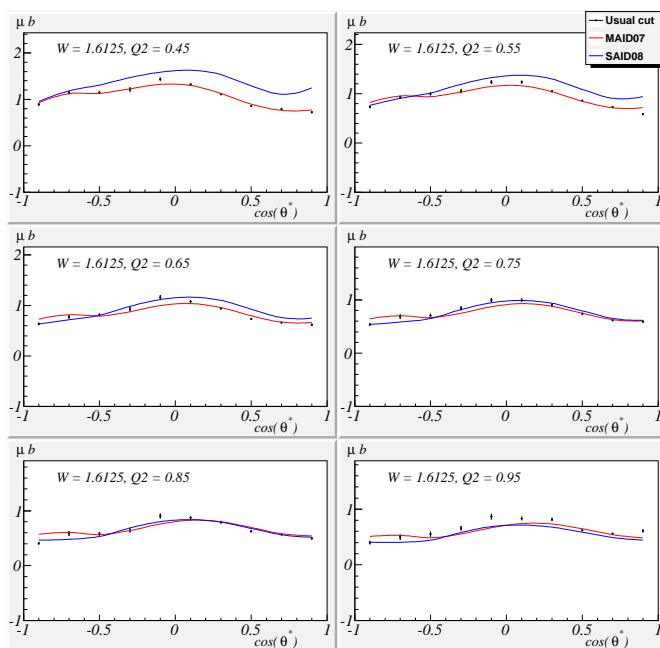


**Fig. 6.25:**  $\sigma_T + \epsilon\sigma_L$  from Eq. 6.18 at  $W = 1.6125$  GeV in different  $Q^2$  bins overlapped with predictions of the models.

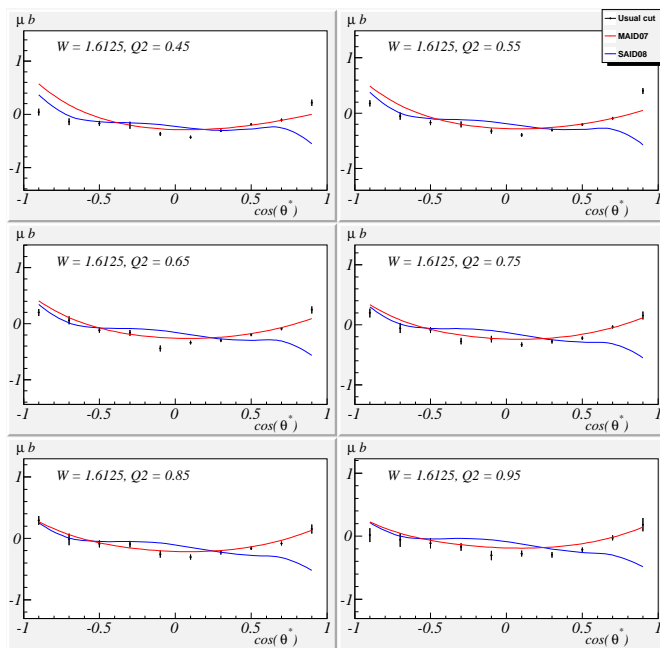


**Fig. 6.26:**  $\sigma_{LT}$  from Eq. 6.18 at  $W = 1.6125$  GeV in different  $Q^2$  bins overlapped with predictions of the models.

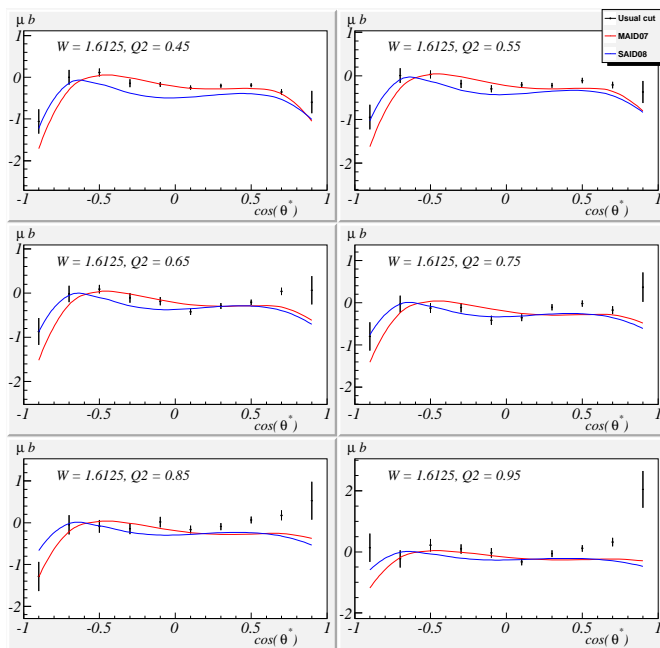


**Fig. 6.27:**  $\sigma_{TT}$  from Eq. 6.18 at  $W = 1.6125$  GeV in different  $Q^2$  bins overlapped with predictions of the models.

on the firmer ground by calculating the well-known cross sections and comparing them to the existing models. Two processes are chosen to be such benchmarks: elastic electron scattering with detection of the electron only or both electron and proton, and inclusive electron scattering. Together, they will cover full kinematical range of the experiment with very high statistical precision, and will show the quality of the event selection.

Another aspect of the calculating of such benchmark cross sections is that we take same steps on the simulation side as we do for the single pion electroproduction, except using different event generator. The good agreement will make the handling of the simulation more trustworthy.

### **6.5.1 Data set selection**

During the quite long experimental run the variations of the experimental conditions, like the target density, can lead to the different yields of events. Based on the number of the events per Faraday cup charge for different reaction and sets of cut, the decision to eliminate four runs (NN 36158, 36159, 36160, 36429) from further consideration was made (Fig. 6.28.)

### **6.5.2 Elastic cross section**

Elastic cross section is a good benchmark of the overall selection of the electron and proton since it is very well studied, and in the case of our kinematics can be

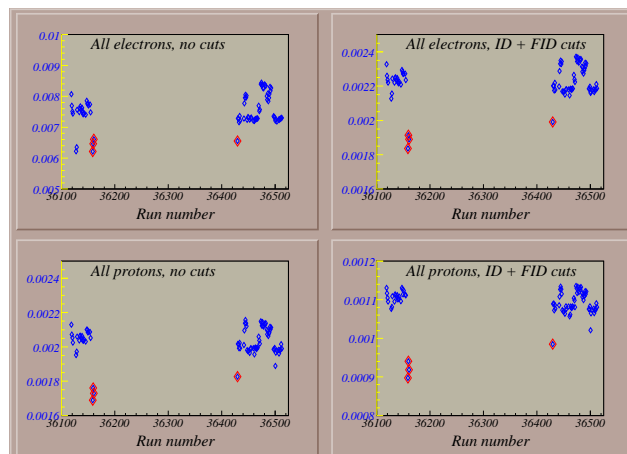


**Fig. 6.28:** Number of events per Faraday cup charge for the different reactions. Excluded runs are highlighted in red.

measured with the very high statistical accuracy. As elastic, we treated events with the  $0.9 \leq W \leq 1.05$  GeV.

To estimate the absolute cross section, we need to have a good estimation of the detector acceptance. In order to calculate it, the *elastgen* package with adjustable inelastic tail was used to generate elastic events (Fig. 6.29), and then the GSIM introduced the realistic resolution effects and inefficiencies. To improve the agreement between data and simulation, electron momentum correction on the simulation part was performed.

We show the cross section in cases when we have only electron detected and when we have both particles. For every sector all events were divided in the bins of  $1^\circ$  over electron  $\theta$ , and acceptance was calculated as a ratio of the number of reconstructed events in the given bin to the number of generated.

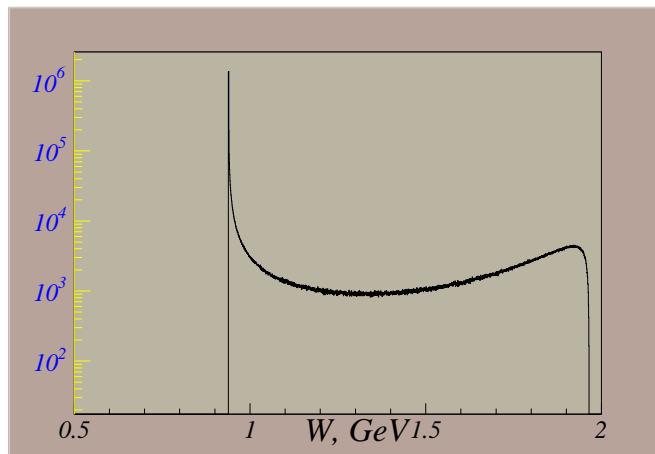


**Fig. 6.29:** Spectrum of generated events with radiative tail.

The studies ( ??) showed, that the efficiency of the TOF system is overestimated in the simulation, and the correction factor equal to 1.05 was applied to all the results which require the detection of the proton.

Resulting cross sections (with and without the detection of the proton) was then compared to the radiated Bosted parametrization [105] (Fig. 6.30, Fig. 6.31).

In case of the detections of electrons our data varies from the parametrization by not more than 5% for the most of the  $\theta$ , and even with addition of the proton arm our results are still within the 5% from the predicted values.

### 6.5.3 Inclusive cross section

The advantage of the inclusive electron scattering is that it has the same kinematical coverage as the single pion electroproduction process we study.

To calculate the acceptance, we generate events with the code based on the

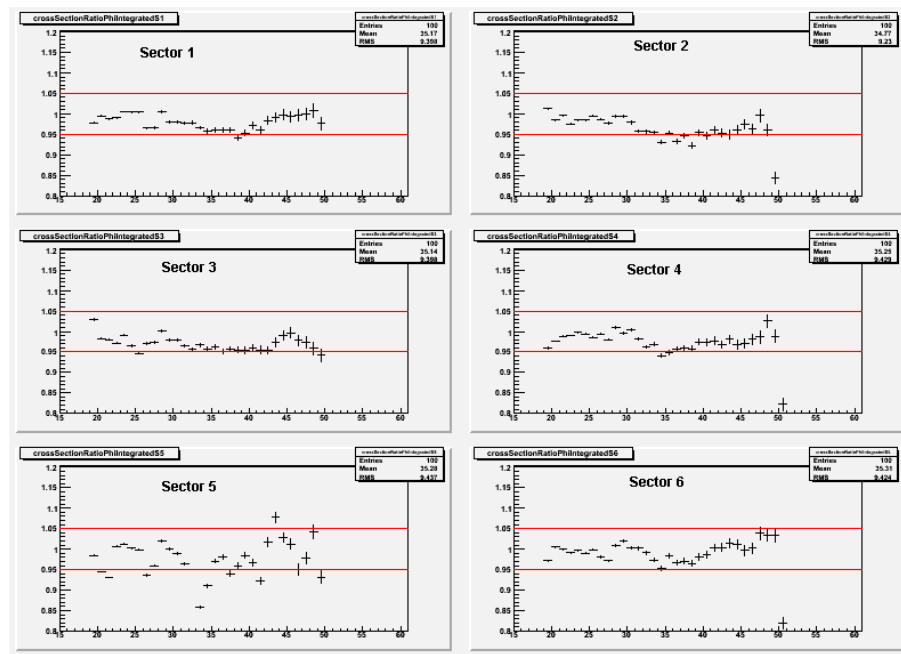


**Fig. 6.30:** Ratio of the elastic cross section in case of the electron detection to the Bosted parametrization as a function of the electron  $\theta$  in different sectors. Red line is  $1 \pm 5\%$ .

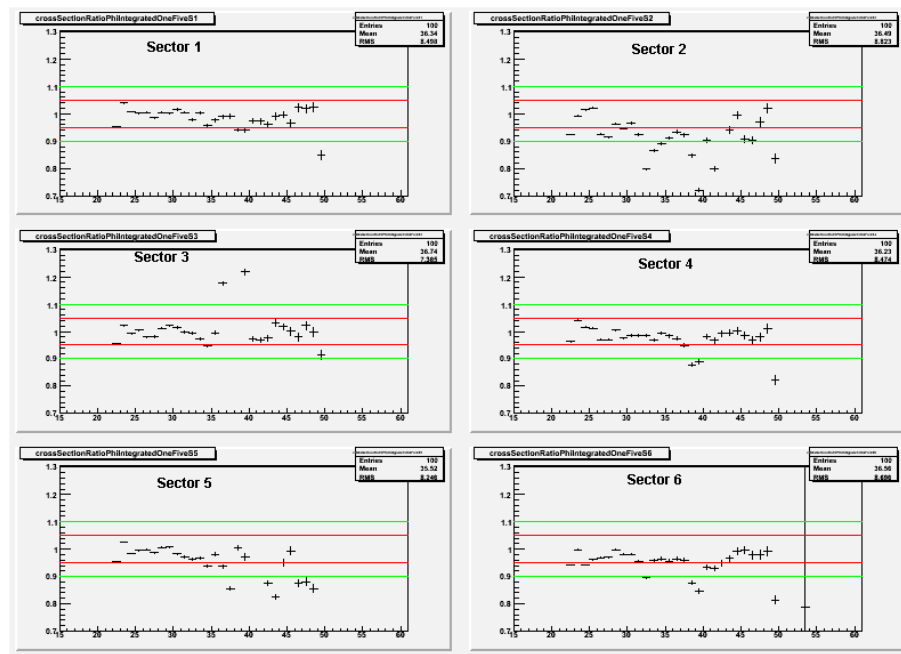


**Fig. 6.31:** Ratio of the elastic cross section in case of the simultaneous electron and proton detection to the Bosted parametrization as a function of the electron  $\theta$ . Red line is  $1 \pm 5\%$ , green line -  $1 \pm 10\%$ .

Keppel model and then project them on the GSIM simulation of the detector.

For the presentation of the result we choose the same binning in the  $W$  and  $Q^2$  as we have in the case of the  $ep \rightarrow ep\pi^0$  channel:  $0.1 \text{ GeV}^2$  wide bins in the  $Q^2$  in the region of  $0.3 - 1.0 \text{ GeV}^2$  and  $0.25 \text{ MeV}$  wide bins in the  $W$  in the region of  $1.1 - 2.0 \text{ GeV}$ .

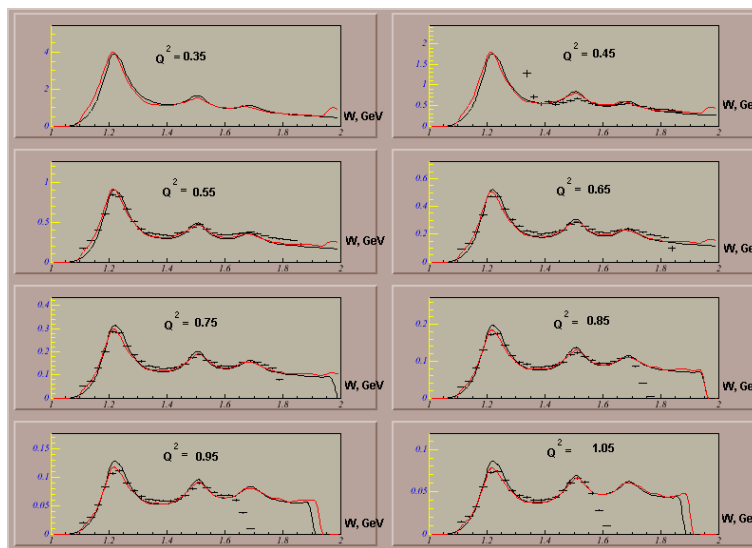


**Fig. 6.32:** Inclusive cross section compared to Brasse (red) and Keppel (black) parametrization.

The observed strong bin migration effect, especially at low  $W$ , required the momentum correction to be applied to the simulation with the generated events used as the reference. To account for the possible difference between the value of the cross section in the center point of the bin and the average value in that bin, we developed and applied the bin centering correction based on the Keppel

parametrization. For that, each  $W - Q^2$  bin was divided in ten sub bins and average value of the cross sections over them was divided by the value in the center of the bin.

The resulting cross sections with all corrections applied are compared with Keppel and Brasse parametrizations (Fig. 6.32). Except for values at the highest  $W$  points for each  $Q^2$  bin, the agreement with data is satisfactory. Actually, the disagreement between that data and different models is of the same order as between the models themselves.

## 6.6 Summary

We extract all differential cross section of  $\pi^0$  electroproduction in wide  $W$  and  $Q^2$  region with almost complete angular coverage.

Quality of procedure, including data cooking, charged particle identification, corrections and event selection, simulation and detector efficiency estimation is extensively checked against well know reaction of elastic and inclusive electron scattering, which cover full  $W$  and  $Q^2$  spectrum of our measurements.

Comparison with based on the existing data on  $\pi^0$  electroproduction models predictions also confirms high quality of presented results.

It enables us to go further and check the sensitivity of data to manifestation of difference resonances using the technique of Legendre multipole truncation.

## 6.7 Systematics studies

### 6.7.1 Overview

Since sometimes it is not possible to determine the ideal position for a specific cut, we will perform the estimation of how the final result depends on the shape and position of the given cut. To do that, we vary the cut within reasonable limits, making it more stringent or more relaxed, and then calculate the cross section with this modified cut. Four variations for each cut are performed, two of them being more relaxed, and two - more stringent, and the final result for the systematic uncertainty is determined as the RMS of the deviations of the modified cross sections from the original one bin by bin:

$$\Delta_{RMS} = \frac{\sqrt{\Delta_S^2 + \Delta_{MS}^2 + \Delta_L^2 + \Delta_{ML}^2}}{\sqrt{n}}, \quad (6.23)$$

where  $\Delta_X$  corresponds to the difference between the cross section with the nominal cut and the modified one ( $S$  - strict,  $MS$  - most strict,  $L$  - Loose,  $ML$  - most loose,  $n$  - number of variations). The following cuts are considered in this study:

1. Electron ID
  - Electron sampling fraction cut
  - Electron fiducial cut
2. Proton ID
  - Proton timing cut

- Proton fiducial cut

### 3. Pion ID

- $M_x^2(ep \rightarrow epX)$  cut
- BH subtraction,  $\Delta\phi_{\pi^0}^*$  cut
- BH subtraction,  $\Delta\theta_{1p}$  cut
- BH subtraction,  $\Delta\theta_{2p}$  cut

## 6.7.2 Electron ID

### Sampling fraction cut

We vary the sampling fraction cut in the way, presented in the Eq. 6.24. Note, that the width of the cut varied in wide range up to  $\pm 18\%$ . The same procedure is then applied to the simulation, and for each set of cuts the cross section is calculated exactly in the same way as for the result reported.

The resulting systematical error is 1.51%.

$$0.78 * cut_0 < E_{tot}/P < cut_0 * 1.18(\text{most loose}), \quad (6.24a)$$

$$0.82 * cut_0 < E_{tot}/P < cut_0 * 1.1(\text{loose}), \quad (6.24b)$$

$$1.22 * cut_0 < E_{tot}/P < cut_0 * 0.9(\text{strict}), \quad (6.24c)$$

$$1.28 * cut_0 < E_{tot}/P < cut_0 * 0.82(\text{most strict}). \quad (6.24d)$$

## Electron fiducial cut

Variations of the electron fiducial cut are described in the Eq. 6.25:

$$\theta_{cut} > \theta_{cut0} - 0.5, \phi_{cut} > \phi_{cut0} - 1 \quad (\text{most loose}), \quad (6.25a)$$

$$\theta_{cut} > \theta_{cut0} - 0.25, \phi_{cut} > \phi_{cut0} - 0.5 \quad (\text{loose}), \quad (6.25b)$$

$$\theta_{cut} > \theta_{cut0} + 0.25, \phi_{cut} > \phi_{cut0} + 0.5 \quad (\text{strict}), \quad (6.25c)$$

$$\theta_{cut} > \theta_{cut0} + 0.5, \phi_{cut} > \phi_{cut0} + 1 \quad (\text{most strict}), \quad (6.25d)$$

where  $\theta_{cut}$  is the position of the shifted cut and  $\theta_{cut0}$  is the original position of the cut. The overall systematical uncertainty from this cut is 4%.

### 6.7.3 Proton ID

#### Proton timing cut

The proton identification is based on the timing cut, described in Section 4.3.2. To determine the effect of the cut variation on the cross section, we shift the cut in the manner described in the Eq. 6.26, where  $cut_-$  and  $cut_+$  correspond to the upper and lower border of the original cut:

$$1.25 * cut_- < E_{tot}/P < cut_+ * 1.25 \quad (\text{most loose}), \quad (6.26a)$$

$$0.12 * cut_- < E_{tot}/P < cut_+ * 1.12 \quad (\text{loose}), \quad (6.26b)$$

$$0.87 * cut_- < E_{tot}/P < cut_+ * 0.87 \quad (\text{strict}), \quad (6.26c)$$

$$0.75 * cut_- < E_{tot}/P < cut_+ * 0.75 \quad (\text{most strict}). \quad (6.26d)$$

This cut is responsible for 1.2% of the final uncertainty.

### Proton fiducial cut

Too large systematical error, corresponding to the fiducial cut, is a good indication that the cut position was not chosen properly. To check that, we vary the cut in the manner, described in the Eq. 6.27:

$$\theta_{cut} > \theta_{cut0} - 0.5, \phi_{cut} > \phi_{cut0} - 1.5 \quad (\text{most loose}), \quad (6.27a)$$

$$\theta_{cut} > \theta_{cut0} - 0.25, \phi_{cut} > \phi_{cut0} - 0.75 \quad (\text{loose}), \quad (6.27b)$$

$$\theta_{cut} > \theta_{cut0} + 0.25, \phi_{cut} > \phi_{cut0} + 0.75 \quad (\text{strict}), \quad (6.27c)$$

$$\theta_{cut} > \theta_{cut0} + 0.5, \phi_{cut} > \phi_{cut0} + 1.5 \quad (\text{most strict}). \quad (6.27d)$$

The resulting systematical uncertainty is equal to 5.2%, which is not too much keeping in mind quite significant variations of the cut parameters.

### 6.7.4 Pion ID

#### $M_x^2$ cut

The first cut in the set of the BH separation cuts sets the upper and lower limit on the missing mass spectrum to eliminate pion radiative events and the rest of the BH events, survived the other cuts. It is deeply connected to the radiative corrections calculations, and to make a proper estimation for each cut modification we need to set the appropriate  $V_{cut}$  and recalculate the radiative corrections. The

Cut type	Cut value	$V_{cut}$
Most strict cut	0.044	0.0258
Strict cut	0.0549	0.0367
Regular cut	0.0657	0.0475
Loose cut	0.0766	0.058
Most loose cut	0.0874	0.0692

**Table 6.4:** Missing mass cut and  $V_{cut}$  values.

same cut we use on the reconstructed events is applied to the events we generate with the *ao\_rad*. The cut values (with the corresponding  $V_{cut}$ ) can be found in the Table 6.4.

The sample radiative correction for one bin with different cuts applied is presented in Fig 6.33. This cut is the largest source of the systematical error, responsible for the 8.4% of it.

### $\Delta\phi_{\pi^0}^*$ cut

The shape of this cut is a result of careful studies, described in Section 4.6, so there is no apparent reason to change it. What we varied is the cut position: the shift is equal to  $\pm 0.004 \text{ GeV}^2$  for the intermediate cut and  $\pm 0.008 \text{ GeV}^2$  for the extreme variations. The systematical uncertainty from this cut is about 3.6%.

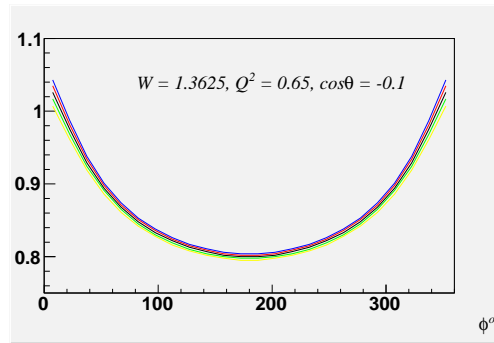


**Fig. 6.33:** The radiative corrections corresponding to the different values of the  $V_{cut}$  (black: 0.0475; green: 0.0367; yellow: 0.0258; red: 0.058; blue: 0.069)

Black line correspond to the nominal cut position.

### $\Delta\theta_1$ cut

We vary the cut as shown in Fig. 6.34 around the nominal position of  $5^\circ$  from  $3^\circ$  to  $7^\circ$  with the step of  $1^\circ$ . Contribution from this cut is equal 0.7%.

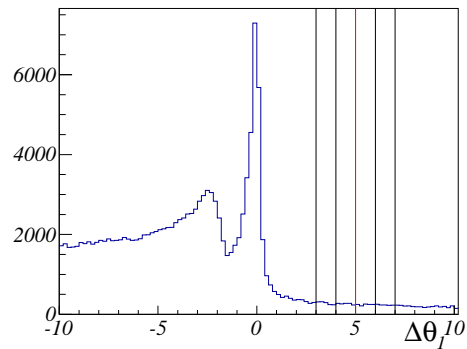


**Fig. 6.34:** Variations of the  $\Delta\theta_1$  cut. Red line is nominal cut position ( $5^\circ$ ), black lines show variations.

### $\Delta\theta_2$ cut

Studied in the manner, similar to the cut above by varying the cut position to the values of 16, 18, 22 and 24 degrees around the nominal value of 20 degrees, we find this cut to bring additional 0.5% to the systematical uncertainty.

### 6.7.5 Normalization uncertainty

The result of elastic studies shows us that the deviation of the experimentally obtained cross section with or without the proton detection is within  $\pm 5\%$  of the cross section. It is used as the value of the overall normalization error, and includes target geometry, target density fluctuation, Faraday cup uncertainty and inefficiencies of our procedures for both event selection and simulation.

### 6.7.6 Summary

Table 6.5 summarizes the different sources of uncertainties with the corresponding values and gives the overall systematical error of the experiment.

### 6.7.7 Error propagation

The errors reported here are for the cross section calculations. In order to have the systematical error estimation for the consecutive results (structure functions, Legendre moments), we apply the same procedure, used for the nominal cross section -  $a + b\cos\phi + c\cos 2\phi$  fit to all the cross section variations, corresponding to

Cut	Uncertainty, %
Sampling fraction	1.51
Electron FID	4.02
Proton ID	1.19
Proton FID	5.16
$M_x^2$ cut	8.39
$\Delta\theta_1$ cut	0.72
$\Delta\theta_2$ cut	0.47
$\Delta\phi_{CMS}$ cut	3.61
Normalization	5
Total	12.5

**Table 6.5:** Summary of sources of systematical error.

the different cuts, and then calculate the RMS for the structure functions using (Eq. 6.23). To calculate the systematic uncertainty for the Legendre polynomials coefficients, we fit all five variations of each structure functions and then calculate the RMS (Eq. 6.23) on the bin by bin basis.

## Chapter 7

### Physics analysis

#### 7.1 Legendre polynomials and fits to the structure functions

The comprehensive analysis of the data presented here will require the combined analysis of the reported  $\pi^0$  electroproduction results along with the information on other channels:  $ep \rightarrow en\pi^+$ ,  $ep \rightarrow ep\eta$  and  $ep \rightarrow ep\pi^+\pi^-$ . The ability to describe various channels within the unified framework would be a good indication of the reliability of separation between resonant and background mechanisms.

However, with the Legendre polynomial expansion of the structure functions we can get some insight on the dominant partial wave contribution at the particular resonance region and sensitivity of our data to contributions from different resonances. The Legendre polynomial expansion of the structure functions in general form can be expressed as in Eqs. 7.1 - 7.3 (for the details of the derivation

see App. A):

$$\sigma_T + \epsilon\sigma_L = \sum_{i=0}^{2l} A_i P_i(\cos\theta_\pi^*), \quad (7.1)$$

$$\sigma_{LT} = \sum_{i=0}^{2l-1} B_i P_i(\cos\theta_\pi^*), \quad (7.2)$$

$$\sigma_{TT} = \sum_{i=0}^{2l-2} C_i P_i(\cos\theta_\pi^*), \quad (7.3)$$

where  $l$  is the highest orbital momentum of the  $\pi^0$  considered (see Chapter 1).

Expression for the polynomial truncated up to  $l = 1$  ( $p$ -wave) is presented in the Eqs. 7.4-7.6:

$$\sigma_T + \epsilon\sigma_L = A_0 P_0(\cos\theta) + A_1 P_1(\cos\theta) + A_2 P_2(\cos\theta), \quad (7.4)$$

$$\sigma_{TT} = B_0 P_0(\cos\theta), \quad (7.5)$$

$$\sigma_{LT} = C_0 P_0(\cos\theta) + C_1 P_1(\cos\theta), \quad (7.6)$$

and up to  $l = 2$  ( $d$  - wave) in the Eqs. 7.7-7.9:

$$\sigma_T + \epsilon\sigma_L = A_0 P_0(\cos\theta) + A_1 P_1(\cos\theta) + A_2 P_2(\cos\theta) + A_3 P_3(\cos\theta) + A_4 P_4(\cos\theta), \quad (7.7)$$

$$\sigma_{TT} = B_0 P_0(\cos\theta) + B_1 P_1(\cos\theta) + B_2 P_2(\cos\theta), \quad (7.8)$$

$$\sigma_{LT} = C_0 P_0(\cos\theta) + C_1 P_1(\cos\theta) + C_2 P_2(\cos\theta) + C_3 P_3(\cos\theta). \quad (7.9)$$

The  $l = 3$  ( $f$ -wave) expression is written in the Eqs. 7.10-7.12:

$$\begin{aligned} \sigma_T + \epsilon\sigma_L = & A_0P_0(\cos\theta) + A_1P_1(\cos\theta) + A_2P_2(\cos\theta) + A_3P_3(\cos\theta) + A_4P_4(\cos\theta) \\ & + A_5P_5(\cos\theta) + A_6P_6(\cos\theta), \end{aligned} \quad (7.10)$$

$$\sigma_{TT} = B_0P_0(\cos\theta) + B_1P_1(\cos\theta) + B_2P_2(\cos\theta) + B_3P_3(\cos\theta) + B_4P_4(\cos\theta), \quad (7.11)$$

$$\begin{aligned} \sigma_{LT} = & C_0P_0(\cos\theta) + C_1P_1(\cos\theta) + C_2P_2(\cos\theta) + C_3P_3(\cos\theta) + C_4P_4(\cos\theta) \\ & + C_5P_5(\cos\theta), \end{aligned} \quad (7.12)$$

It follows from the fits to the structure functions, that in many cases expansion up to  $l = 1$  fails to provide adequate description of the data (Fig. 7.1). The full picture is available at the analysis web-page. The  $l = 2$  expansion leads to a better agreement, but keeping the higher order  $l = 3$  is beneficial for the two reasons:

- $l = 2$  and  $l = 3$  should provide the same results for common coefficients due to orthogonality of Legendre multipoles, and any significant deviation indicates a systematical error;
- at higher  $W$  in the region of the  $F_{15}(1680)$  resonance one should expect to see effects of higher multipoles ( $l = 3$ ) which are not necessarily manifested in the lower Legendre moments.

We compare the result of this work to world data in Figs. 7.2 and 7.3. We notice, that the  $\Delta$  region is extensively covered in the  $\pi^0$  production channel in a wide

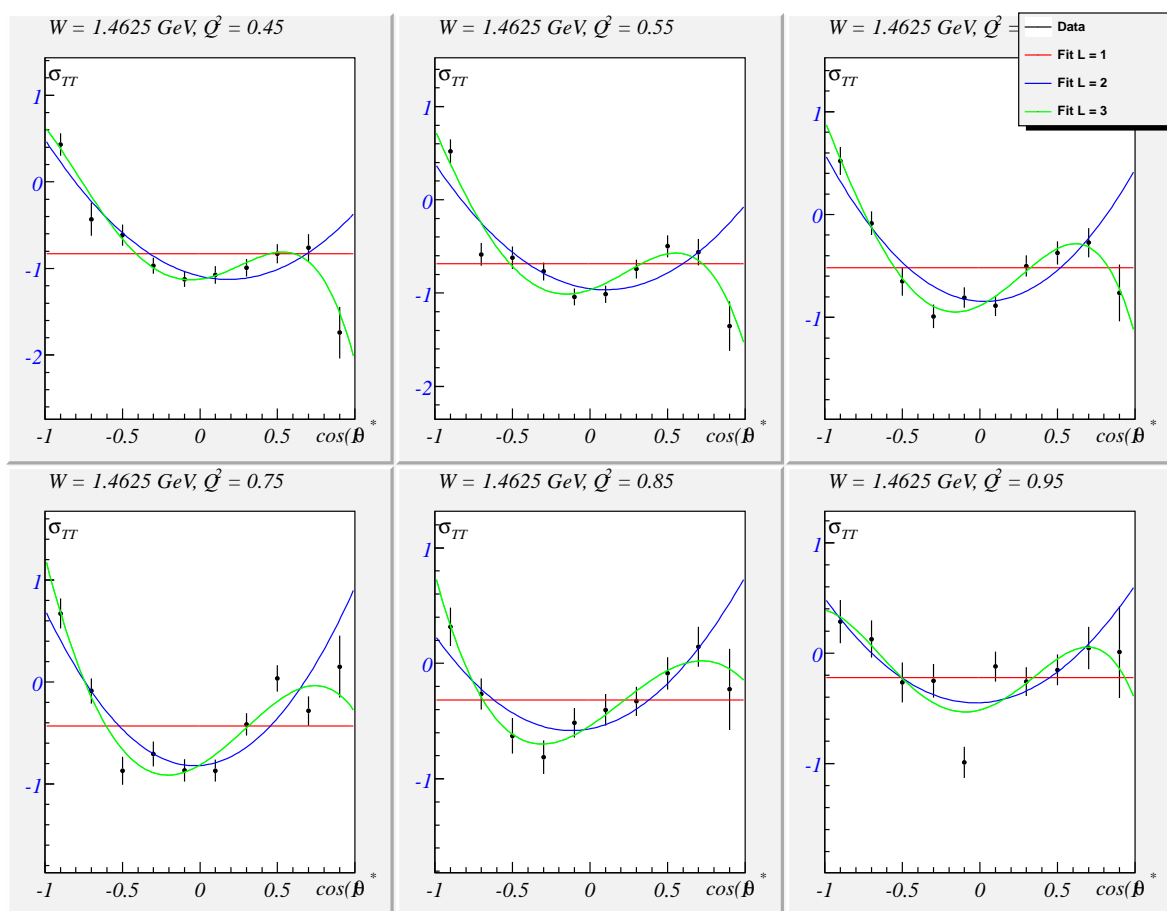


**Fig. 7.1:** Fit to the structure function  $\sigma_{TT}$  with the Legendre polynomials of the different orders. The case of  $l = 1$  ( $s$ -wave only) does not provide good enough description of the data.

$Q^2$  region. Reported results are well aligned with the available data from Hall B at the Jefferson Lab as well as with the data from Hall A, where completely different experimental setup was employed. Good agreement with other data in well-known  $\Delta$  region substantiates our claims about the reliability of the results in the full resonance region we present.

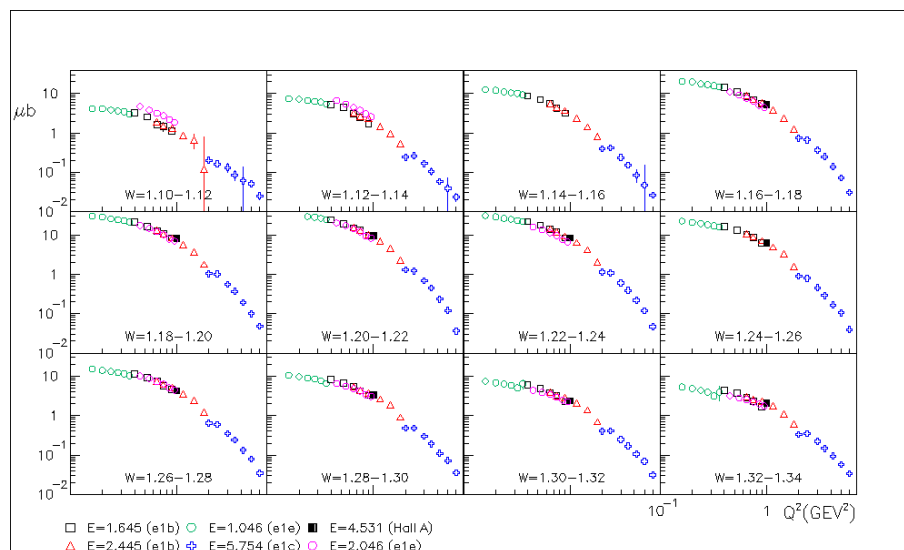


**Fig. 7.2:** The  $A_0$  coefficient (see Eq. 7.7) as a function of  $Q^2$  in the different  $W$  bins. Reported results (magenta circles) are compared to the Hall B results of [48] (red triangles and black squares, obtained with the different beam energy), [47] (green circles), [49] (blue crosses), and results of Hall A [46] (solid black square).

## 7.2 Multipole analysis

Since various resonances manifest different evolution as a function of the  $W$ , the full range of  $W = 1.1 - 1.8$  GeV was divided into three subranges: the  $\Delta$ , or the

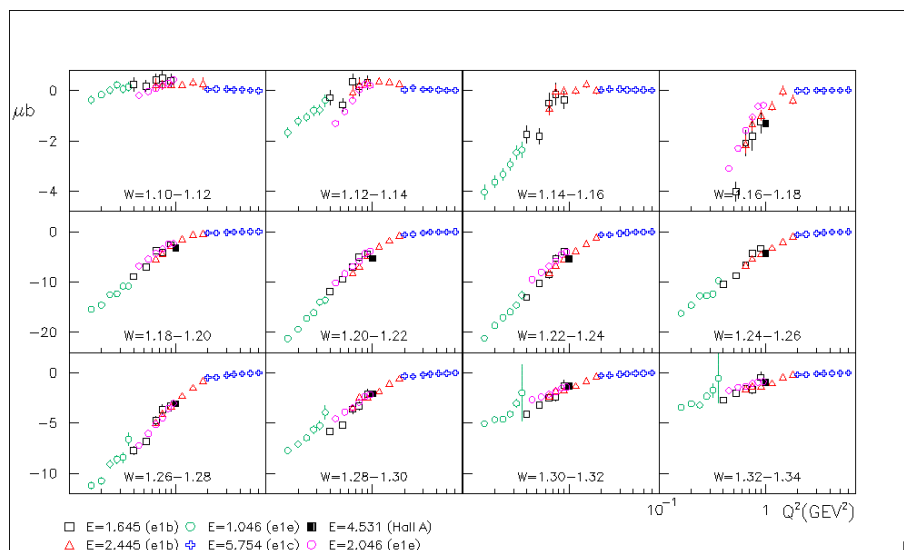


**Fig. 7.3:** The  $B_0$  coefficient (see Eq. 7.8) as a function of the  $Q^2$  in different  $W$  bins. Reported results (magenta circles) are compared to the Hall B results of [48] (red triangles and black squares, obtained with the different beam energy), [47] (green circles), [49] (blue crosses), and results of Hall A [46] (solid black square).

first resonance region of  $W = 1.1 - 1.4$  GeV, the second resonance region  $W = 1.4 - 1.6$  GeV and the third resonance region  $W = 1.6 - 1.8$  GeV.

If one assumes  $M_{1+}$  dominance and keeps only s-and p-wave terms in the  $\Delta$  re-

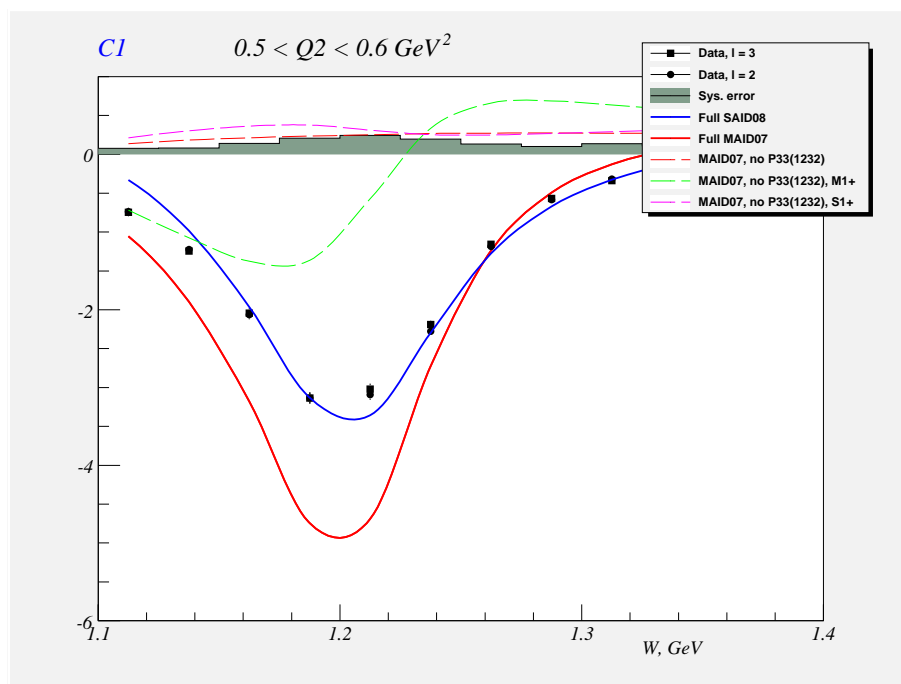


**Fig. 7.4:** The  $C_1$  (Eqs. 7.18 and 7.9) Legendre coefficient in the region of the  $\Delta$  resonance.

gion, a simple relation between Legendre multipole coefficients and EM multipoles

holds:

$$|M_{1+}|^2 = A_0/2, \quad (7.13)$$

$$\text{Re}(E_{1+}M_{1+}^*) = (A_2 - 2C_0/3)/8, \quad (7.14)$$

$$\text{Re}(M_{1-}M_{1+}^*) = -(A_2 + 2(A_0 + C_0))/8, \quad (7.15)$$

$$\text{Re}(E_{0+}M_{1+}^*) = A_1/2, \quad (7.16)$$

$$\text{Re}(S_{0+}M_{1+}^*) = C_0, \quad (7.17)$$

$$\text{Re}(S_{1+}M_{1+}^*) = C_1/6. \quad (7.18)$$

From Eq. 7.18  $C_1$  Legendre coefficient is expected to be sensitive to the  $S_{1+}$  transition amplitude through its interference with the dominant term,  $M_{1+}$ . Fig. 7.4 shows that such sensitivity is incorporated in the MAID07 model, though the absolute strength of the amplitude is overestimated. The SAID08 predictions are well aligned with the data. This behavior is consistent within all  $Q^2$  range accessible in this experiment. Right above the  $\Delta$  resonance both models are in an agreement with the data.

The same  $C_1$  coefficient at higher  $W$  shows significant sensitivity to all three amplitudes of  $D_{13}(1520)$  state,  $A_{1/2}$ ,  $A_{3/2}$  and  $S_{1/2}$ , and both  $A_{1/2}$  and  $S_{1/2}$  of  $S_{11}(1535)$ . Taking into account how many parameters along with their  $Q^2$  dependencies are to be described, a good agreement between models and data, including overall shape, peak position and zero crossing at  $W \approx 1.6\text{GeV}$  is achieved (Fig. 7.5). Additional information from the  $\eta$  electroproduction channel may be

helpful in order to fix the amplitude of the  $S_{11}(1535)$ .

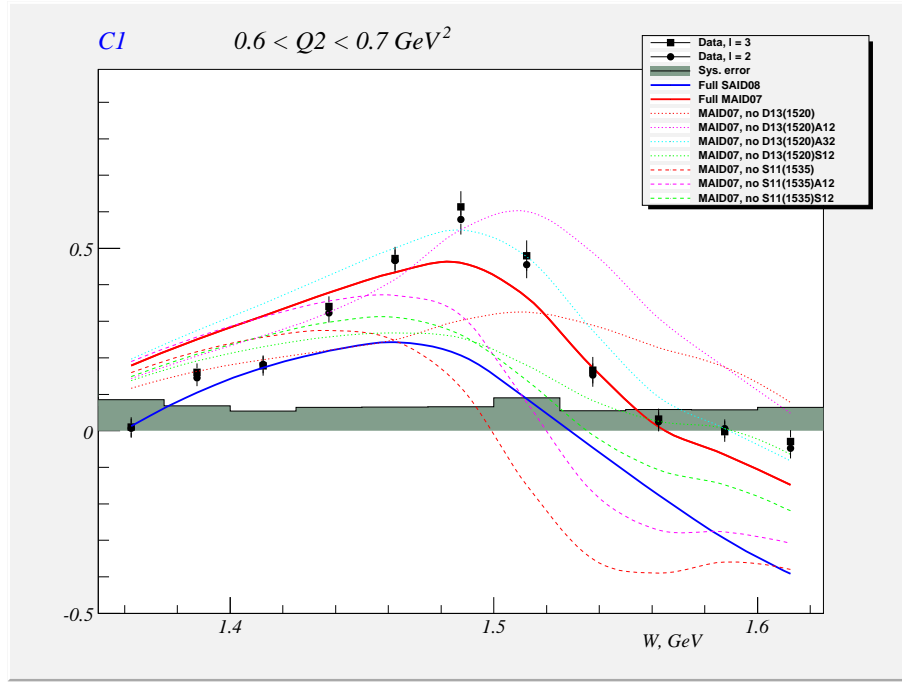


**Fig. 7.5:** The  $C_1$  (Eq. 7.12) Legendre coefficient in the second resonance region. Solid lines are the full model calculations, dashed and dotted lines correspond to particular helicity amplitudes turned off.

In the region of  $W \approx 1.55 \text{ GeV}$  there are two resonances, capable of producing structure observed in Fig. 7.6,  $D_{13}(1520)$  and  $S_{11}(1535)$ . Studies with MAID07 model (which shows a better agreement with the data) reveal sensitivity to the two amplitudes of the  $D_{13}(1520)$  resonance, transverse  $A_{1/2}$  and  $A_{3/2}$  in full  $W$  region and longitudinal  $S_{1/2}$  at higher values of invariant mass. Results of SAID08 hint at the underestimation of this amplitudes. Study of  $Q^2$  dependence of the same  $A_3$  (Fig. 7.7) shows that at higher photon virtuality contributions of

$A_{1/2}$  and  $A_{3/2}$  amplitudes notably drop, and MAID07 describes this effect very well.

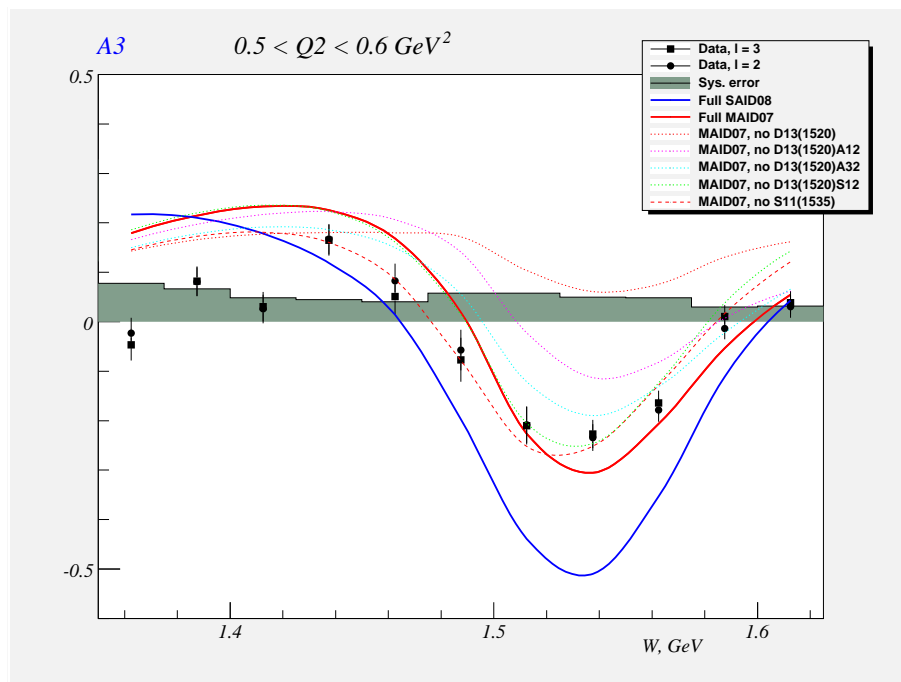


**Fig. 7.6:** The  $A_3$  (Eq. 7.10) Legendre coefficient at the  $Q^2 = 0.55 \text{ GeV}^2$  in the second resonance region as a function of  $W$ . Solid lines are the full model calculations, dashed and dotted lines correspond to particular helicity amplitudes turned off.

The prominent feature of the  $C_2$  coefficient at intermediate  $W$  is rather flat behavior as a function of  $Q^2$ , which is reproduced by both models (Fig. 7.8). The absolute value is predicted as well, though the sign in the SAID08 is opposite to the data. The MAID07 is in agreement with data within the errorbar on both the value and sign. It has almost constant input of the most important  $A_{1/2}$  and  $AS_{3/2}$  throughout the full  $Q^2$  range.

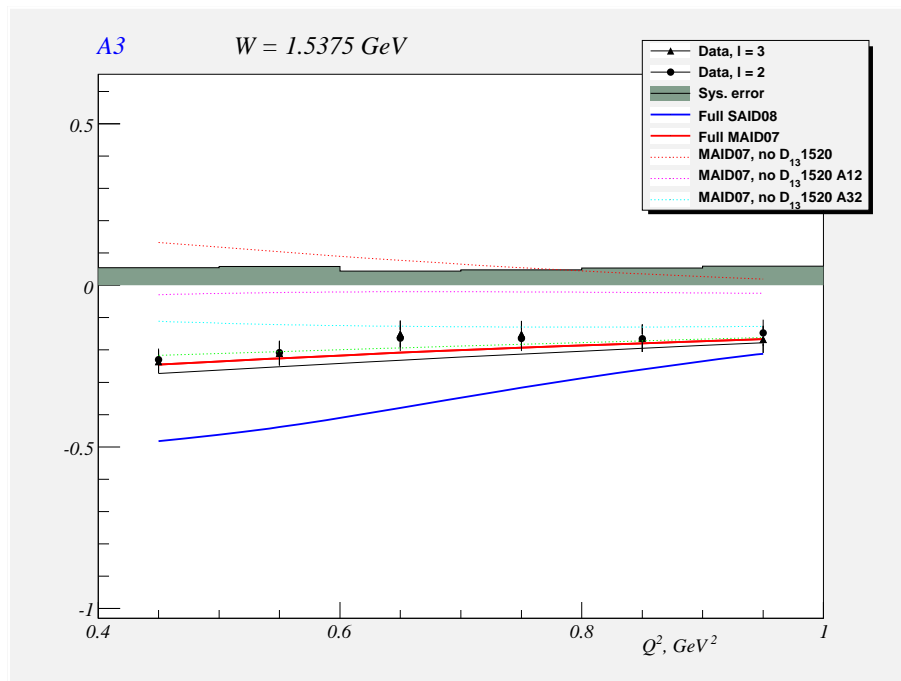


**Fig. 7.7:** The  $A_3$  (Eq. 7.10) Legendre coefficient at the  $W = 1.5375$  GeV as a function of the  $Q^2$ . Solid lines are the full model calculations, dashed and dotted lines correspond to particular helicity amplitudes turned off.

Third resonance region is dominated by the  $F_{15}(1680)$  state. The enhancement at the peak position of this resonance is clearly seen in both model predictions (Fig. 7.9), though the SAID08 underestimates the value. Another feature of SAID08 predictions is the variation of the position of the structure as a function of the  $W$  which can not be supported or rejected by the data on this stage of the analysis.

Studies with MAID07 show that the effect of the  $D_{15}(1675)$  on these multipole is negligible, while the  $S_{1/2}$  and  $A_{3/2}$  of the  $F_{15}(1680)$  play a dominant role.

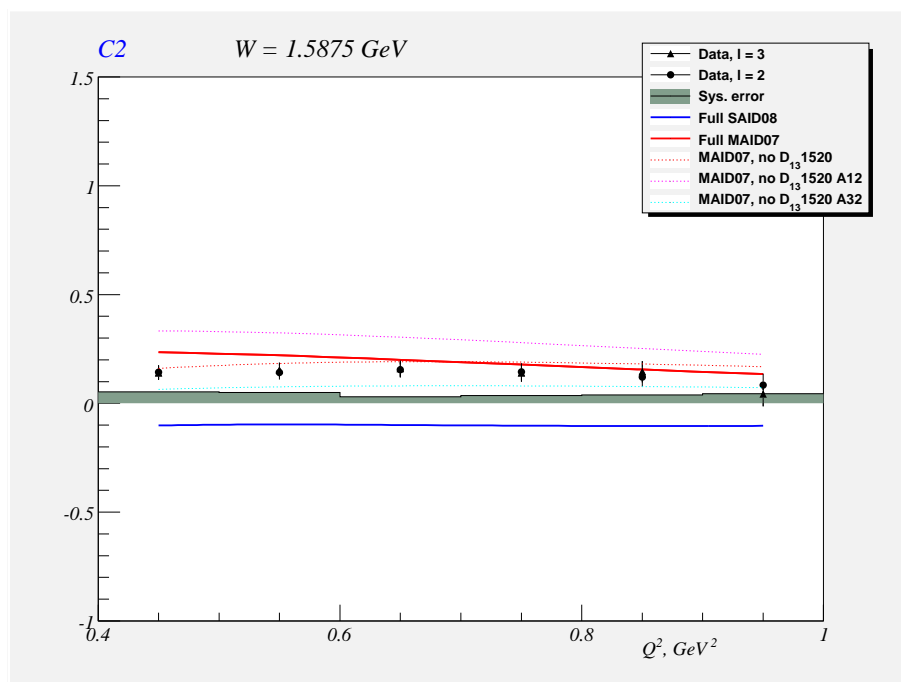


**Fig. 7.8:** The  $C_2$  (Eq. 7.12) Legendre coefficient at the  $W = 1.5875\text{GeV}$  as a function of the  $Q^2$ . Solid lines are the full model calculations, dashed and dotted lines correspond to particular helicity amplitudes turned off.

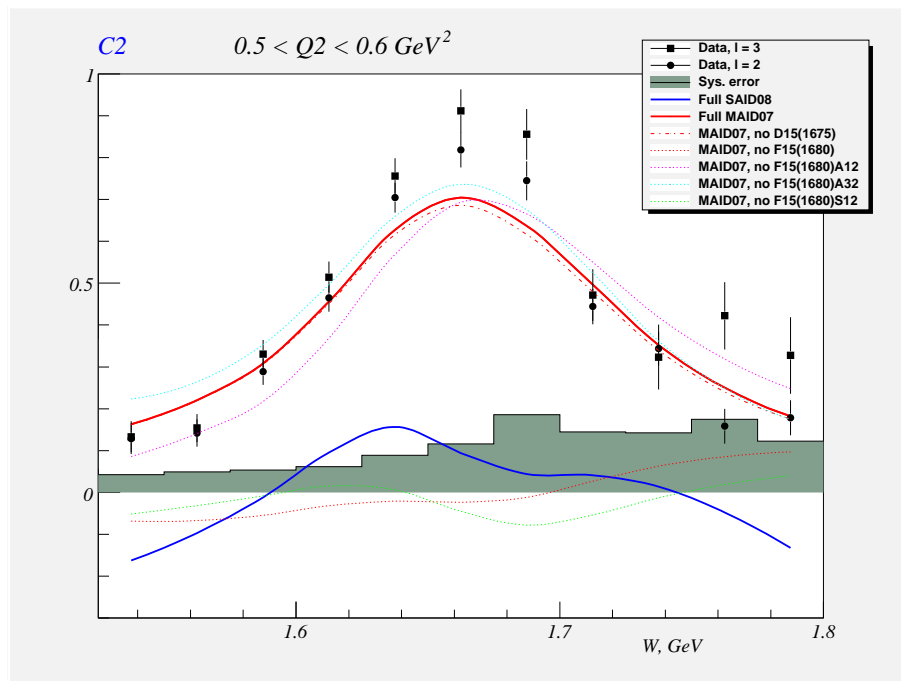


**Fig. 7.9:** The  $C_2$  (Eq. 7.12) Legendre OA coefficient at the  $Q^2 = 0.55 \text{ GeV}^2$  in the third resonance region as a function of  $W$ . Solid lines are the full model calculations, dashed and dotted lines correspond to particular helicity amplitudes turned off.

Both model calculations predict a structure at around 1.7 GeV in the  $A_2$  Legendre coefficient (Fig. 7.10). The difference between the two models should be attributed to the different amplitude strength of  $F_{15}(1680)$  resonance, in particular to the possibly different sign of  $A_{1/2}$  and  $S_{1/2}$ . Data shows zero crossing at  $W = 1.6$  GeV which seems to support the SAID08 prediction, though the systematical uncertainties and difference between fits with Legendre polynomials with  $l = 2$  and  $l = 3$  do not allow to draw a firm conclusion. This issue is to be addressed during the upcoming analysis.

The higher Legendre multipoles reveal the structure at  $W$  around 1.7 GeV (Fig. 7.11). It is easily identified with the  $F_{15}(1680)$  resonance (with most important amplitudes being the  $A_{1/2}$  and  $A_{3/2}$ ) and is described by the both models surprisingly well, including falloff up to 1.65 GeV and consecutive rise. The zero crossing is presented in MAID07 and is supported by the data, though the systematic error prevents us from making a decisive conclusion.

### 7.3 Conclusion

Using the data from the CLAS detector at the Jefferson Lab, the differential cross-section of the  $\pi^0$  electroproduction off the proton was measured for the first time in wide kinematical range  $W = 1.1 - 1.8$  GeV,  $Q^2 = 0.4 - 1.0$  GeV<sup>2</sup>.

The measured data were validated by a series of test and cross-checks performed on all stages of the data analysis. The reliability of charged particle ID,

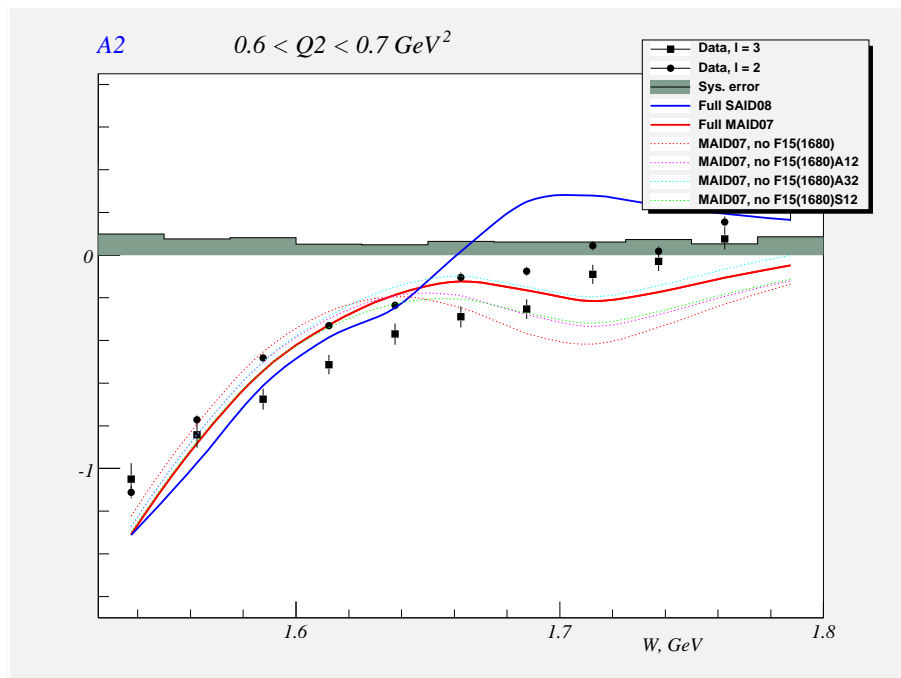


**Fig. 7.10:** The  $A_2$  (Eq. 7.10) Legendre coefficient at the  $Q^2 = 0.65 \text{ GeV}^2$  in the third resonance region as a function of  $W$ . The solid lines indicate the full model calculations, and the dashed and dotted lines correspond to model calculations with specific helicity amplitudes excluded.

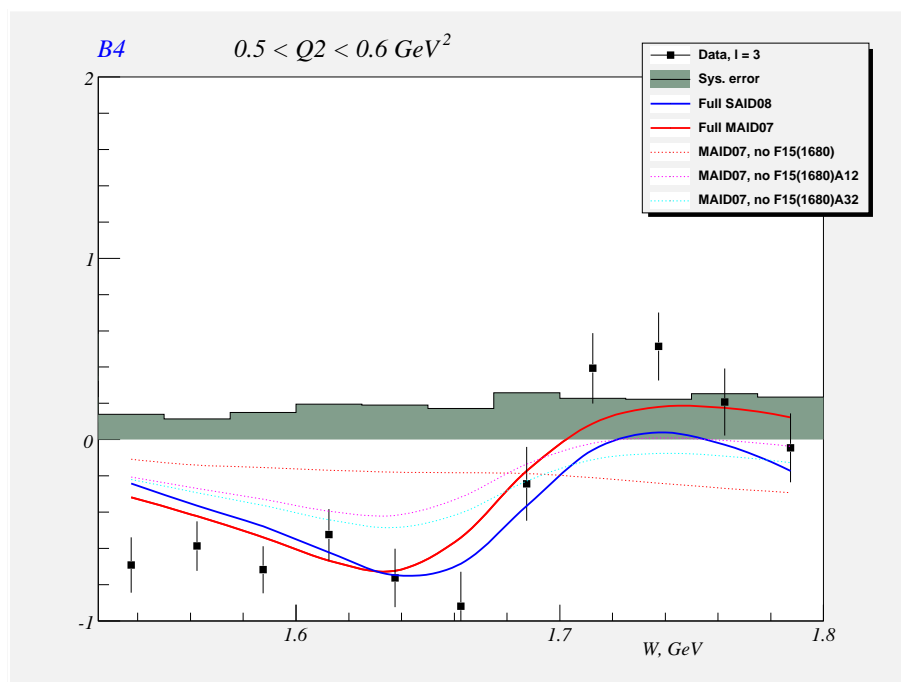


**Fig. 7.11:** The  $B_4$  (Eq. 7.11) Legendre coefficient at the  $Q^2 = 0.65 \text{ GeV}^2$  in the third resonance region as a function of  $W$ . Solid lines are the full model calculations, dashed and dotted lines correspond to particular helicity amplitudes turned off.

absolute normalization, data handling, simulation, and detector description were confirmed by calculating cross sections of elastic and inclusive electron scattering and comparing the results to different models. The obtained result were checked against available data on  $\pi^0$  electroproduction in the common regions of invariant mass and photon virtualities and were found to be in a good agreement.

The full angular coverage and high statistical accuracy of this measurement enabled us to extract the unpolarized structure functions  $\sigma_L + \epsilon\sigma_T$ ,  $\sigma_{TT}$ , and  $\sigma_{TL}$  with high precision. Legendre multipole truncation analysis, performed along with model calculation, have shown the sensitivity of reported data to major  $N^*$  resonances in the region and, more specifically, to the individual transitional amplitudes.

Best known  $\Delta(1232)$  resonance is well reproduced in reported data and is manifested in both dominant  $M_{1+}$  transition directly and through the interference of it with other multipoles. On the level of cross section both models are in a good agreement with data, though we observe significant difference in particular Legendre coefficients.

$D_{13}(1520)$  state dominates the second resonance region in the  $\pi^0$  production channel. Two major production amplitudes  $A_{1/2}$  and  $A_{3/2}$  are prominent in several Legendre coefficients and appear determined in MAID07. SAID08 results are consisten in the general shape of the curves but sometimes lack a quantitative agreement.

The data reported shows sensitivity to both  $A_{1/2}$  and  $A_{3/2}$  amplitudes of  $S_{11}(1535)$  state. Analysis of this data in the  $\pi^0$  channel along with the data on the  $\eta$  electroproduction will significantly enrich our knowledge on this  $N^*$ .

$P_{11}(1440)$ , or Roper resonance, was shown to be important in few Legendre coefficients, mostly via the  $S_{(1/2)}$  amplitude. This resonance has been studied in the  $\pi^+$  channel and the addition of this data will provide the information with different nonresonant amplitudes, thus improving the quality of separation of resonant part of the transitional amplitude.

The third resonance region in this channel is dominated by the  $F_{15}(1680)$  resonance and is sensitive to all three amplitudes of it. Currently, data available on this resonance is very limited, and this measurements will drastically improve our understanding of its structure, as well as structures of higher-lying resonances.

This result is the only source of information on  $\pi^0$  electroproduction in the region of higher  $W$  and provides additional valuable information in the lower  $W$  region.

The sensitivity of the data to different  $N^*$  throughout the covered  $W$  range is a strong indication that it can be successfully used to extract the  $Q^2$  evolution of the transitional form factors of the nucleon resonances in the resonance region, which will significantly enhance our understanding of QCD behavior in the confinement regime.

## Chapter 8

### BIBLIOGRAPHY

#### 8.1 \*

##### Bibliography

- [1] K. Nakamura et al. (Particle Data Group), *J Phys. G* **37**, 075021 (2010).
- [2] M. S. Bahgwat et al, *Phys. Rev. D* **71**, 015203 (2005).
- [3] M. S. Bahgwat et al, *Phys. Rev. C* **68**, 015203 (2003).
- [4] M. S. Bahgwat, P. C. Tandy, *AIP. Conf. Proc* **842**, 225 (2006).
- [5] H. L. L. Roberts, L. Chang, I. C. Cloet and C. D. Roberts, *Few Body Syst.* **51**, 1 (2011).
- [6] Lei Chang et al, *Chin. Phys. C* **33**, 1189 (2009).
- [7] C. Chen, L. Chang, C. D. Roberts, S. Wan and D. J. Wilson, arXiv:1204.2553 [nucl-th].

- [8] L. Chang, I. C. Cloet, C. D. Roberts and H. L. L. Roberts, AIP Conf. Proc. **1354**, 110 (2011).
- [9] C. D. Roberts, I. C. Cloet, L. Chang and H. L. L. Roberts, arXiv:1108.1327 [nucl-th].
- [10] C. Alexandrou, arXiv:1111.5960 [hep-lat].
- [11] C. Alexandrou, arXiv:0906.4137 [hep-lat].
- [12] A. J. G. Hey and R. L. Kelly, Phys. Rept. **96**, 71 (1983).
- [13] S. Capstick and N. Isgur, Phys. Rev. D **34**, 2809 (1986).
- [14] A. Chodos, R. L. Jaffe, K. Johnson and C. B. Thorn, Phys. Rev. D **10**, 2599 (1974).
- [15] A. W. Thomas, S. Theberge and G. A. Miller, Phys. Rev. D **24**, 216 (1981).
- [16] G. E. Brown and M. Rho, Phys. Lett. B **82**, 177 (1979).
- [17] G. S. Adkins, C. R. Nappi and E. Witten, Nucl. Phys. B **228**, 552 (1983).
- [18] J. K. Perring and T. H. R. Skyrme, Nucl. Phys. **31**, 550 (1962).
- [19] T. H. R. Skyrme, Nucl. Phys. **31**, 556 (1962).
- [20] R. Bijker, F. Iachello and A. Leviatan, Annals Phys. **236**, 69 (1994). [nucl-th/9402012].

- [21] G. Eckart and B. Schwesinger, Nucl. Phys. A **458**, 620 (1986).
- [22] H. B. Nielsen and A. Patkos, Nucl. Phys. B **195**, 137 (1982).
- [23] J. B. Kogut and L. Susskind, Phys. Rev. D **9**, 3501 (1974).
- [24] P. Maris and C. D. Roberts, Int. J. Mod. Phys. E **12**, 297 (2003). [arXiv:nucl-th/0301049].
- [25] C. Roberts, A. Williams Prog. in Part. and Nucl. Phys. **33**,477 (1994) .
- [26] I. G. Aznauryan, V. D. Burkert, Prog. Part. Nucl. Phys. **67**, 1 (2012). [arXiv:1109.1720 hep-ph].
- [27] G. F. Chew, M. L. Goldberger, F. E. Low and Y. Nambu, Phys. Rev. **106**, 1337 (1957).
- [28] A.A. Logunov, A.N. Takhvelidze, L.D. Soloviev Nucl. Phys. **4**, 427 (1957).
- [29] R. C. E. Devenish and D. H. Lyth, Nucl. Phys. B **43**, 228 (1972).
- [30] R. L. Walker, Phys. Rev. **182**, 1729 (1969).
- [31] R. D. Peccei, Phys. Rev. **181**, 1902 (1969).
- [32] D. Drechsel, O. Hanstein, S. S. Kamalov and L. Tiator, Nucl. Phys. A **645**, 145 (1999). [arXiv:nucl-th/9807001].
- [33] I. G. Aznauryan, Phys. Rev. C **67**, 015209 (2003). [arXiv:nucl-th/0206033].

- [34] R. A. Arndt, W. J. Briscoe, I. I. Strakovsky and R. L. Workman, Phys. Rev. C **66**, 055213 (2002). [arXiv:nucl-th/0205067].
- [35] R. A. Arndt, R. L. Workman, Z. Li and L. D. Roper, Phys. Rev. C **42**, 1864 (1990).
- [36] N. Suzuki, B. Julia-Diaz, H. Kamano, T.-S. H. Lee, A. Matsuyama, T. Sato Phys. Rev. Lett.**104**, 042302 (2010).
- [37] S. S. Kamalov and S. N. Yang, Phys. Rev. Lett. **83**, 4494 (1999). [arXiv:nucl-th/9904072].
- [38] T. Sato and T. S. H. Lee, Phys. Rev. C **54**, 2660 (1996). [arXiv:nucl-th/9606009].
- [39] I. G. Aznauryan, V. D. Burkert, Progress in Particle and Nuclear Physics, **67**, 1 (2012).
- [40] I. G. Aznauryan, V. D. Burkert, H. Egiyan, et al., Phys. Rev. C **71**, 015201 (2005).
- [41] I. G. Aznauryan, V. D. Burkert, Phys. Rev. C **72**, 045201 (2005).
- [42] J. S. Ball Phys. Rev. **124**, 2014 (1961).
- [43] R. A. Arndt et al, AIPConf. Proc. **904** 269 (2007).
- [44] G. Laveissiere, Phys. Rev. C **69**, 045203 (2004) .

- [45] J. J. Kelly, et al., Phys .Rev . C **95**, 102001 (2007).
- [46] J. J. Kelly, et al., Phys .Rev . C **75**, 025201 (2007).
- [47] L.C. Smith et al, Proceedings of the workshop “Shape of hadrons”, p.222, Athens, 2006.
- [48] K. Joo, L. C. Smith, et al., Phys. Rev. Lett. **88**, 122001 (2002).
- [49] M. Ungaro, P. Stoler, I. Aznauryan, V. D. Burkert, K. Joo, L.C. Smith, Phys.Rev.Lett. **97**, 112003 (2006).
- [50] V. V. Frolov et al, Phys. Rev. Lett. **82**, 45-48 (1999).
- [51] A. N. Villano, Phys. Rev. C **80**, 035203 (2009).
- [52] S. Stave Eur. Phys. J. A **30**, 471 (2006).
- [53] S. Stave, et al Phys. Rev. C **78**, 025209 (2008).
- [54] C. Mertz, et al, Phys. Rev. Lett. **86**, 2963 (2001).
- [55] C. Kunz, et al, Phys.Lett. B5 **64**, 21 (2003).
- [56] N.F. Sparveris, et al, Phys. Rev. Lett. **94**, 022003 (2005). Eur.Phys.J.A34:69-97,2007
- [57] D. Drechsel, S.S. Kamalov, L. Tiator, Eur.Phys.J. A **34**, 69-97 (2007) .

- [58] R.A. Arndt, W.J. Briscoe, I.I. Strakovsky, R.L. Workman,  
<http://gwdac.phys.gwu.edu>
- [59] K. Bermuth, D. Drechsel, L. Thiator, J.B. Seaborn, Phys.Rev.D **37**, 89(1988).
- [60] D.H. Lu, A.W. Thomas, A.G. Williams Phys.Rev. C **55**, 3108 (1997).
- [61] A. Faessler, G. Koutsou, B.R. Holsten et al, Phys.Rev.D **74**, 074010 (2006).
- [62] I. G. Aznauryan et al., Phys. Rev. C **78**, 045209 (2008).
- [63] I. G. Aznauryan et al, Phys. Rev. C **80**, 055203 (2009).
- [64] V. I. Mokeev et al., Phys. Rev. C **80**, 045212 (2009).
- [65] V. I. Mokeev et al., Chinese Physics, C **33**, 1210 (2009).
- [66] Z. .P. Li, Phys. Rev. D **44**, 2841 (1991).
- [67] Z. .P. Li, V. D. Burkert, Zh. Li Phys. Rev. D **46**, 70 (1992).
- [68] I. G. Aznauryan, A. S. Bagdasaryan, Sov. J. Nucl. Phys.**41**, 158 (1985).
- [69] R. Siddle et al, Nucl. Phys. B **35**, 93 (1971).
- [70] J. .C Adler et al., Nucl. Phys. B **46**, 573 (1972).
- [71] R. Haidan et al, DESY re. F21-79/03 (1979).
- [72] T. Sato, T.-S. .H. Lee, Phys. Rev. C **63**, 055201 (2001).

- [73] V. Pascalutsa, M. Vanderhaeghen, S. N. Yang, Phys. Rep. **437**, 125 (2007).
- [74] V. Pascalutsa, M. Vanderhaeghen, Phys. Rev.D **80**, 055006 (2009).
- [75] H. R. Grigoryan, T.-S. Lee, Ho-Ung Yee, Phys. Rev.D **76**, 111501 (2007).
- [76] M. J. Dugger, et al., CLAS Collaboration, Phys. Rev. C **79**, 065206 (2009).
- [77] K. Nakamura et al. [Particle Data Group], Journal of Physics G **37**, 1 (2010).
- [78] I. G. Aznauryan, Phys. Rev. C **79**, 025212 (2007).
- [79] G. Ramalho, K. Tsushima, Phys. Rev. D **81**, 077420 (2010).
- [80] R. Thompson, et al., CLAS Collaboration, Phys. Rev. Lett. **86**, 1702 (2001).
- [81] H. Denizli, et al., Phys. Rev. C **76**, 015204 (2007).
- [82] C. S. Armstrong et al., Phys. Rev. D **60**, 052004 (2009).
- [83] M. M. Dalton et al., Phys. Rev. C **80**, 015205 (2009).
- [84] I. G. Aznauryan, Phys. Rev. C **68**, 065204 (2003).
- [85] S. Capstick, B. D. Keister, Phys. Rev. D **51**, 3598 (1995).
- [86] E. Pace, G. Salme, S. Simula, Few Body Syst. Suppl. **10**, 407 (1999).
- [87] V. M. Braun, M. Gockeler, R. Horsley, Phys. Rev. Lett. **103**, 072001 (2009).
- [88] M. Warns, H. Scroder, W. Pfeil, H. Rollnik, Z. Phys. C **46**, 627 (1990).

- [89] M. Aiello, M. M. Giannini, E. Santopinto, J. Phys. G **24**, 753, (1998).
- [90] D. Merten, U. Loring, K. Kretzschmar, B. Metsch, H.-R. Petry, Eur. Phys. J. A **14**, 477 (2002).
- [91] L. Tiator, D. Drechsel, S. Kamalov, M.M. Giannini, E. Santopinto, A. Vassallo, Eur. Phys. J. A **19** (Suppl.1), 55 (2004).
- [92] M. Ferraris, M.M. Giannini, M. Pizzo, E. Santopinto, L. Tiator, Phys. Lett. **B364**, 231 (1995).
- [93] S. Kamalov, S.N. Yang, D. Drechsel, O. Hanstein, L. Tiator, Phys. Rev. **C 64**, 032201 (2001).
- [94] N. Isgur, G. Karl, Phys. Rev. **D18**, 4187 1978; **D18**, 2653 1979, **D20**, 1191 1979.
- [95] M. Mestayer, D. Carman et al., NIM **A449** 81 (2000).
- [96] G. Adams, V. Burkert et al., NIM **A465** 414 (2001).
- [97] E. S. Smith, T. Carstens et al., NIM **A432** 265 (1999).
- [98] M. Amarian, G. Asryan et al., NIM **A465** 460 (2001).
- [99] A. Afanasev, I. Akushevich, V. Burkert, K. Joo, Phys. Rev. D, **66** 0.74004 (2002).
- [100] E. Smith et al, NIM A **432** 625(1999)

- [101] K. S. Egiyan, CLAS NOTE 99-007.
- [102] K. Park, personal communications.
- [103] M. Ungaro, personal communications.
- [104] V. Kubarovsky, personal communications.
- [105] P. E. Bosted, Phys. Rev. C **51**, 409 1995.
- [106] M. Osipenko, CLAS NOTE 2004-20
- [107] M. Ungaro, K. Joo, CLAS NOTE 2010-006

## Appendix A

### Legendre multipoles and structure functions

The multipole decomposition of the CGLN amplitude in terms of the electric ( $E_{l\pm}$ ), magnetic ( $M_{l\pm}$ ) and longitudinal ( $S_{l\pm}$ ), with pion angular momentum  $l$  and total angular momentum  $j = l \pm 1/2$

$$F_1 = \sum_{l \geq 0} (lM_{l+} + E_{l+})P'_{l+1} + [(l+1)M_{l-} + E_{l-}]P'_{l-1}, \quad (\text{A.1})$$

$$F_2 = \sum_{l \geq 1} [(l+1)M_{l+} + lM_{l-}]P'_l, \quad (\text{A.2})$$

$$F_3 = \sum_{l \geq 1} (E_{l+} - M_{l+})P''_{l+1} + (E_{l-} + M_{l-})P''_{l-1}, \quad (\text{A.3})$$

$$F_4 = \sum_{l \geq 2} [M_{l+} - E_{l+} - M_{l-} - E_{l-}]P''_l, \quad (\text{A.4})$$

$$F_5 = \sum_{l \geq 0} [(l+1)L_{l+}P'_{l+1} - lL_{l-}P'_{l-1}], \quad (\text{A.5})$$

$$F_6 = \sum_{l \geq 1} [lL_{l-} - (l+1)L_{l+}]P'_l \quad (\text{A.6})$$

The response functions (we are interested in the unpolarized,  $\sigma_T$ ,  $\sigma_L$ ,  $\sigma_{TL}$ ,  $\sigma_{TT}$ ), are described in terms of the CGLN amplitudes as follows:

$$\begin{aligned} \sigma_T = & |F_1|^2 + |F_2|^2 + \frac{\sin^2\theta}{2}(|F_3|^2 + |F_4|^2) + \text{Re}(\sin^2\theta[F_2^*F_3 + F_1^*F_4 + \cos\theta F_3^*F_4] \\ & - 2\cos\theta F_1^*F_2) \end{aligned} \quad (\text{A.7})$$

$$\sigma_L = \text{Re}(|F_5|^2 + |F_6|^2 + 2\cos\theta F_5^*F_6) \quad (\text{A.8})$$

$$\sigma_{TL} = \sin\theta \text{Re}(-F_2^*F_5 - F_3^*F_5 - F_1^*F_6 - F_4^*F_6 - \cos\theta(F_4^*F_5 + F_3^*F_6)) \quad (\text{A.9})$$

$$\sigma_{TT} = \frac{1}{2}\sin^2\theta[|F_3|^2 + |F_4|^2] + \sin^2\theta \text{Re}(F_2^*F_3 + F_1^*F_4 + \cos\theta F_3^*F_4) \quad (\text{A.10})$$

Leaving only highest order term in each of the CGLN amplitudes:

$$F_1 \approx P_l \quad (\text{A.11})$$

$$F_2 \approx P_{l-1} \quad (\text{A.12})$$

$$F_3 \approx P_{l-1} \quad (\text{A.13})$$

$$F_4 \approx P_{l-2} \quad (\text{A.14})$$

$$F_5 \approx P_l \quad (\text{A.15})$$

$$F_6 \approx P_{l-1} \quad (\text{A.16})$$

Now retaining the highest order term in the SF:

$$\sigma_T \approx |F_1|^2 \approx P_l P_l \approx 2l \quad (\text{A.17})$$

$$\sigma_L \approx |F_5|^2 \approx P_l P_l \approx 2l \quad (\text{A.18})$$

$$\sigma_T + \sigma_L \approx 2l \quad (\text{A.19})$$

$$\sigma_{TL} \approx |F_2 F_5| + |F_1 F_6| \approx P_{l-1} P_l \approx 2l - 1 \quad (\text{A.20})$$

$$\sigma_{TT} \approx F_3^2 + F_2 F_3 + F_1 F_4 \approx P_{l-1} P_{l-1} + P_{l-1} P_{l-1} + P_l P_{l-2} \approx 2l - 2 \quad (\text{A.21})$$

So if we fix the **small**  $l$ , the order of the multipole, in the structure function we will have partial waves up to  $L_{T+L} = 2l$  for  $\sigma_T + \sigma_L$ ,  $L_{TL} = 2l - 1$  for the  $\sigma_{TL}$  and  $L_{TT} = 2l - 2$  for the  $\sigma_{TT}$ .

The equation for the structure functions decomposition into the Legendre polynomials then reads:

$$\sigma_T + \epsilon\sigma_L = \sum_{i=0}^{2l} A_i P_i(\cos\theta_\pi^*) \quad (\text{A.22})$$

$$\sigma_{LT} = \sum_{i=0}^{2l-1} B_i P_i(\cos\theta_\pi^*) \quad (\text{A.23})$$

$$\sigma_{TT} = \sum_{i=0}^{2l-2} C_i P_i(\cos\theta_\pi^*) \quad (\text{A.24})$$

where the  $l$  is the highest order electromagnetic multipole considered in our analysis.

The expression for the polynomial truncated up to  $l = 1$  (p-wave) is presented:

$$\sigma_T + \epsilon\sigma_L = A_0P_0(\cos\theta) + A_1P_1(\cos\theta) + A_2P_2(\cos\theta) \quad (\text{A.25})$$

$$\sigma_{TT} = B_0P_0(\cos\theta) \quad (\text{A.26})$$

$$\sigma_{LT} = C_0P_0(\cos\theta) + C_1P_1(\cos\theta) \quad (\text{A.27})$$

and up to  $l = 2$  (d - wave) reads:

$$\begin{aligned} \sigma_T + \epsilon\sigma_L = & A_0P_0(\cos\theta) + A_1P_1(\cos\theta) + A_2P_2(\cos\theta) + A_3P_3(\cos\theta) \\ & + A_4P_4(\cos\theta) \end{aligned} \quad (\text{A.28})$$

$$\sigma_{TT} = B_0P_0(\cos\theta) + B_1P_1(\cos\theta) + B_2P_2(\cos\theta) \quad (\text{A.29})$$

$$\sigma_{LT} = C_0P_0(\cos\theta) + C_1P_1(\cos\theta) + C_2P_2(\cos\theta) + C_3P_3(\cos\theta) \quad (\text{A.30})$$

The  $l = 3$  (f - wave) expression is written below:

$$\begin{aligned} \sigma_T + \epsilon\sigma_L = & A_0P_0(\cos\theta) + A_1P_1(\cos\theta) + A_2P_2(\cos\theta) + A_3P_3(\cos\theta) + A_4P_4(\cos\theta) \\ & + A_5P_5(\cos\theta) + A_6P_6(\cos\theta) \end{aligned} \quad (\text{A.31})$$

$$\begin{aligned} \sigma_{TT} = & B_0P_0(\cos\theta) + B_1P_1(\cos\theta) + B_2P_2(\cos\theta) + B_3P_3(\cos\theta) \\ & + B_4P_4(\cos\theta) \end{aligned} \quad (\text{A.32})$$

$$\begin{aligned} \sigma_{LT} = & C_0P_0(\cos\theta) + C_1P_1(\cos\theta) + C_2P_2(\cos\theta) + C_3P_3(\cos\theta) + \\ & C_4P_4(\cos\theta) + C_5P_5(\cos\theta) \end{aligned} \quad (\text{A.33})$$